

Quantum Well Infrared Photodetector (QWIP) Focal Plane Arrays

S. D. Gunapala and S. V. Bandara

Center for Space Microelectronics Technology, Jet Propulsion Laboratory, California
Institute of Technology, Pasadena, CA 91109

CONTENT

1. INTRODUCTION

2. COMPARISON OF VARIOUS TYPES OF QWIPs

- 2.1 n-Doped Bound-to-Bound QWIPs
- 2.2 n-Doped Bound-to-Continuum QWIPs
- 2.3 n-Doped Bound-to-Quasibound QWIPs
- 2.4 n-Doped Broad-band QWIPs
- 2.5 n-Doped Bound-to-Bound Miniband QWIPs
- 2.6 n-Doped Bound-to-Continuum Miniband QWIPs
- 2.7 n-Doped Bound-to-Miniband QWIPs
- 2.8 n-Doped Asymmetrical GaAs/Al_xGa_{1-x}As QWIPs
- 2.9 p-Doped QWIPs
- 2.10 Single Quantum Well Infrared Photodetectors
- 2.11 Indirect Band-gap QWIPs
- 2.12 n-doped In_{0.53}Ga_{0.47}As/In_{0.52}Al_{0.48}As QWIPs
- 2.13 n-doped In_{0.53}Ga_{0.47}As/InP QWIPs
- 2.14 InGaAsP - quaternary QWIPs
- 2.15 n-doped GaAs/Ga_{0.5}In_{0.5}P QWIPs
- 2.16 n-doped GaAs/Al_{0.5}In_{0.5}P QWIPs
- 2.17 n-doped In_{0.15}Ga_{0.85}As/GaAs QWIPs
- 2.18 p-doped In_{0.53}Ga_{0.47}As/InP QWIPs

3. FIGURES OF MERIT

- 3.1 Absorption spectra
- 3.2 Dark current
- 3.3 Responsivity
- 3.4 Dark current noise
- 3.5 Noise gain and Photoconductive gain
- 3.6 Quantum efficiency
- 3.7 Detectivity

4. *LIGHT COUPLING*

- 4.1 Random Reflectors
- 4.2 Two-Dimensional Periodic Gratings
- 4.3 Corrugated Structure
- 4.4 Microlenses

5. *IMAGING FOCAL PLANE ARRAYS*

- 5.1 Effect of nonuniformity
- 5.2 128x128 VLWIR Imaging Camera
- 5.3 256x256 LWIR Imaging Camera
- 5.4 640X486 LWIR Imaging Camera
- 5.5 Dualband (MWIR & LWIR) Detectors
- 5.6 Dualband (LWIR & VLWIR) Detectors
- 5.7 High Performance QWIPs for Low Background Applications
- 5.8 Broad-band QWIPs for Thermal Infrared Imaging Spectrometers

6. *APPLICATIONS*

- 6.1 Fire Fighting
- 6.2 Volcanology
- 6.3 Medicine
- 6.4 Defense
- 6.5 Astronomy

7. *SUMMARY*

ACKNOWLEDGMENTS

REFERENCES

Quantum Well Infrared Photodetector (QWIP) Focal Plane Arrays

S. D. Gunapala and S. V. Bandara

Center for Space Microelectronics Technology, Jet Propulsion Laboratory, California Institute of Technology, Pasadena, CA 91109

1. INTRODUCTION

Intrinsic infrared detectors in the long-wavelength range (6 - 20 μm) are based on interband transition which promotes an electron across the band gap (E_g) from the valence band to the conduction band as shown in Fig. 1. These photoexcited-electrons can be collected efficiently, thereby producing a photocurrent in the external circuit. Since the incoming photon has to excite an electron from the valence band to the conduction band, the energy of the photon ($h\nu$) must be higher than the E_g of the photosensitive material. Therefore, the spectral response of the detectors can be tuned by controlling the E_g of the photosensitive material. Examples for such materials are $\text{Hg}_{1-x}\text{Cd}_x\text{Te}$ and $\text{Pb}_{1-x}\text{Sn}_x\text{Te}$ in which the energy gap can be controlled by varying x . This means detection of very long-wavelength infrared (VLWIR; $>12 \mu\text{m}$) radiation up to 20 μm requires small band gaps down to 62 meV. It is well known that these low band gap materials are more difficult to grow and process than large band gap semiconductors such as GaAs. These difficulties motivate the exploration of utilizing the intersubband transitions in multi-quantum-well (MQW) structures made of large band gap semiconductors (Fig. 2).

The idea of using MQW structures to detect infrared radiation can be explained by using the basic principles of quantum mechanics. The quantum well is equivalent to the well known particle in a box problem in quantum mechanics, which can be solved by the time independent Schrodinger equation. The solutions to this problem are the Eigen values that describe energy levels inside the quantum well in which the particle is allowed to exist.

The position of the energy levels are primarily determined by the quantum well dimensions (height and width). For infinitely high barriers and parabolic bands, the energy levels in the quantum well are given by (Weisbuch, 1987)

$$E_j = \left(\frac{\eta^2 \pi^2}{2m^* L_w^2} \right) j^2, \quad (1)$$

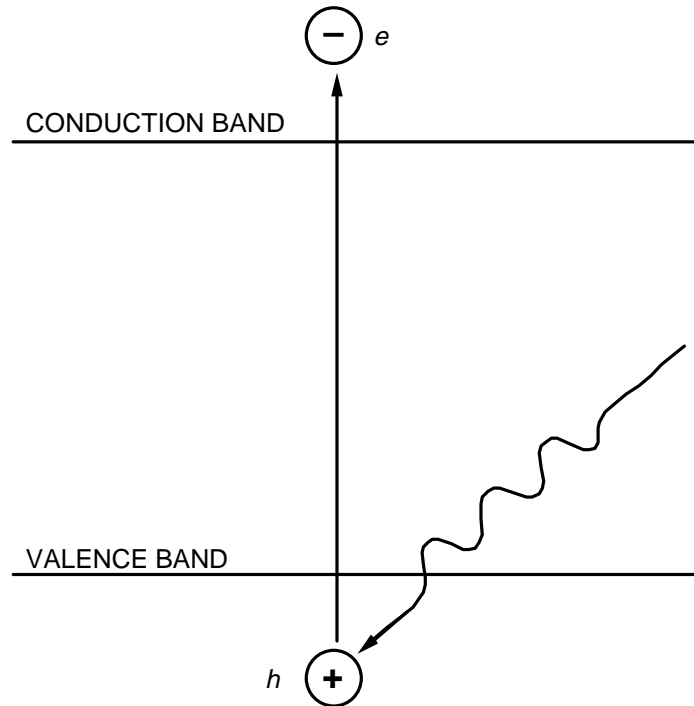


Fig. 1. Band diagram of conventional intrinsic infrared photodetector. (Gunapala and Bandara, 1995)

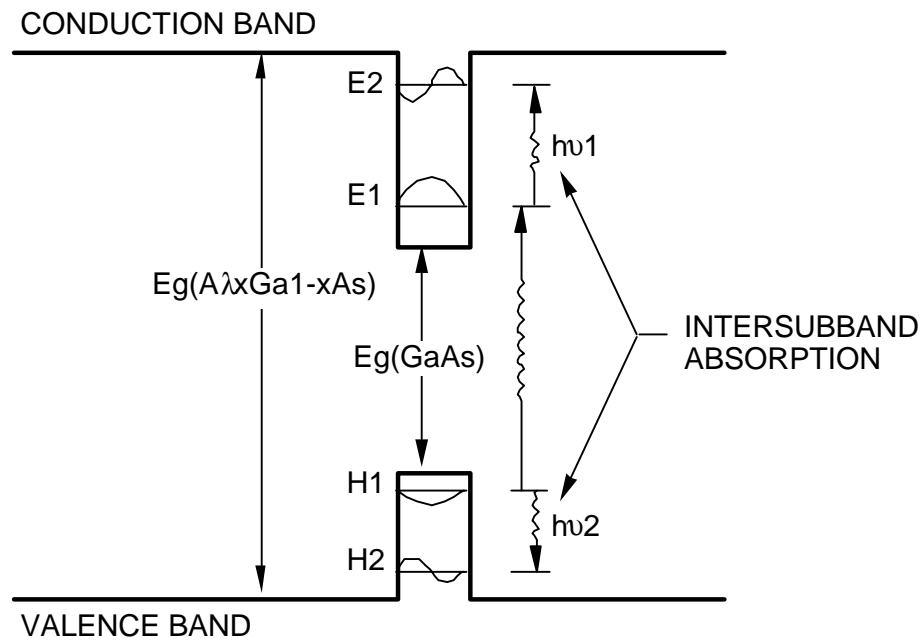


Fig. 2. Schematic band diagram of a quantum well. Intersubband absorption can take place between the energy levels of a quantum well associated with the conduction band (n-doped) or the valence band (p-doped). (Levine, 1993)

where L_w is the width of the quantum well, m^* is the effective mass of the carrier in the quantum well, and j is an integer. Thus the intersubband energy between the ground and the first excited state is

$$(E_2 - E_1) = (3\eta^2 \pi^2 / 2m^* L_w^2). \quad (2)$$

The quantum well infrared photodetectors (QWIPs) discussed in this article utilize the photoexcitation of electron (hole) between the ground state and the first excited state in the conduction (valance) band quantum well (See Fig. 2). The quantum well structure is designed so that these photoexcited carriers can escape from the quantum well and be collected as photocurrent. In addition to larger intersubband oscillator strength, these detectors afford greater flexibility than extrinsically doped semiconductor infrared detectors because the wavelength of the peak response and cutoff can be continuously tailored by varying layer thickness (quantum well width) and barrier composition (barrier height).

The lattice matched GaAs/ $\text{Al}_x\text{Ga}_{1-x}\text{As}$ material system is a very good candidate to create such a quantum well structure, because the band gap of $\text{Al}_x\text{Ga}_{1-x}\text{As}$ can be changed continuously by varying x (and hence the height of the quantum well). Thus, by changing the quantum well width L_w and the barrier height (Al molar ratio of $\text{Al}_x\text{Ga}_{1-x}\text{As}$ alloy), this intersubband transition energy can be varied over a wide range, from short-wavelength infrared (SWIR; 1-3 μm), the mid-infrared (MWIR; 3-5 μm), through long-wavelength (LWIR; 8-12 μm) and into the VLWIR (>12 μm). It is important to note that unlike intrinsic detectors which utilize interband transition, quantum wells of these detectors must be doped since the photon energy is not sufficient to create photocarriers ($h\nu < E_g$).

The possibility of using GaAs/ $\text{Al}_x\text{Ga}_{1-x}\text{As}$ MQW structures to detect infrared radiation was first suggested by Esaki *et al.* (1977), experimentally investigated by Smith *et al.* (1983), and theoretically analyzed by Coon *et al.* (1984). The first experimental observation of the strong intersubband absorption was performed by West *et al.* (1985), and the first QWIP was demonstrated by Levine *et al.* (1987b) at Bell Laboratories. Levine *et al.* (1988c) also introduced QWIP involving bound-to-continuum intersubband transitions with wider $\text{Al}_x\text{Ga}_{1-x}\text{As}$ barriers and demonstrated dramatically improved detectivity. Recent developments in these detectors have already led to the demonstration of large (up to 640x486) high-sensitivity staring arrays by several groups (Bethea *et al.*, 1991, 1992, 1993; Kozłowski *et al.*, 1991; Beck *et al.*, 1994; Gunapala *et al.*, 1997a, 1997b, 1998a; Andersson *et al.*, 1997; Choi *et al.*, 1998b; Breiter *et al.*, 1998).

2. COMPARISON OF VARIOUS TYPES OF QWIPs

2.1 n-Doped Bound-to-Bound QWIPs

As mentioned previously, the first *bound-to-bound* state QWIP was demonstrated by Levine *et al.* (1987b), which consisted of 50 periods of $L_w = 65 \text{ \AA}$ GaAs and $L_b = 95 \text{ \AA}$ $\text{Al}_{0.25}\text{Ga}_{0.75}\text{As}$ barriers sandwiched between top (0.5 \mu m thick) and bottom (1 \mu m thick) GaAs contact layers. The center 50 \AA of the GaAs wells were doped to $N_D = 1.4 \times 10^{18} \text{ cm}^{-3}$ and the contact layers were doped to $N_D = 4 \times 10^{18} \text{ cm}^{-3}$. This structure was grown by molecular beam epitaxy (MBE). These thicknesses and compositions were chosen to produce only two states in the quantum well with energy spacing give rise to a peak wavelength of 10 \mu m . The measured (Levine *et al.*, 1987b) absorption spectra peaked at $\lambda_p = 10.9 \text{ \mu m}$ with a full-width at half-maximum of $\Delta \nu = 97 \text{ cm}^{-1}$. The peak absorbance $a = -\log(\text{transmission}) = 2.2 \times 10^{-2}$ corresponds to a net absorption of 5% (i.e., $a = 600 \text{ cm}^{-1}$).

After the absorption of infrared photons, the photoexcited carriers can be transported either along the plane of quantum wells (with an electric field along the quantum wells) or perpendicular to the wells (with an electric field perpendicular to the epitaxial layers). As far as the infrared detection is concerned, perpendicular transport is superior to parallel transport (Wheeler and Goldberg, 1975) since the difference between the excited state and ground state mobilities is much larger in the latter case, and consequently, transport perpendicular to the quantum wells (i.e., growth direction) gives a substantially high photocurrent. In addition, the heterobarriers block the transport of ground state carriers in the quantum wells, and thus lower dark current. For these reasons, QWIPs are based on escape and perpendicular transport of photoexcited carriers as shown in Fig. 3.

In the latter versions of the bound-to-bound state QWIPs, Choi *et al.* (1987c) has used slightly thicker and higher barriers to reduce tunneling induced dark current. When they increased the barrier thickness from $L_b = 95 \text{ \AA}$ to 140 \AA and $\text{Al}_x\text{Ga}_{1-x}\text{As}$ barrier height from $x = 0.25$ to 0.36 , the dark current (also the photocurrent) was significantly reduced. The nonlinear behavior of the responsivity and the dark current versus bias voltage observed in the bound-to-bound QWIPs is due to the complex tunneling process associated with the high-field domain formation (Choi *et al.*, 1987c).

2.2 n-Doped Bound-to-Continuum QWIPs

In the previous section, we mentioned the QWIP containing two bound states. By reducing the quantum well width, it is possible to push the strong bound-to-bound intersubband absorption into the continuum, resulting in a strong bound-to-continuum intersubband absorption. The major advantage of the bound-to-continuum QWIP is that the photoexcited electron can escape from the quantum well to the continuum transport

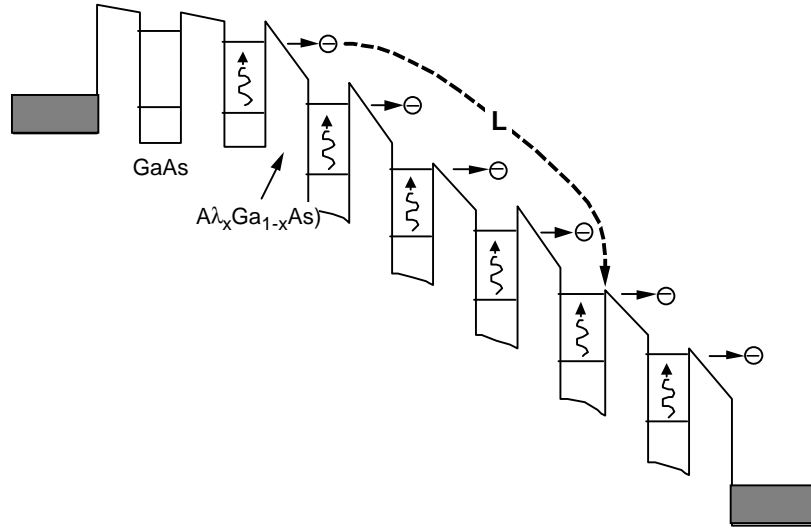


Fig. 3. Conduction-band diagram for a bound-to-bound QWIP, showing the photoexcitation (intersubband transition) and tunneling out of well. (Levine, 1993)

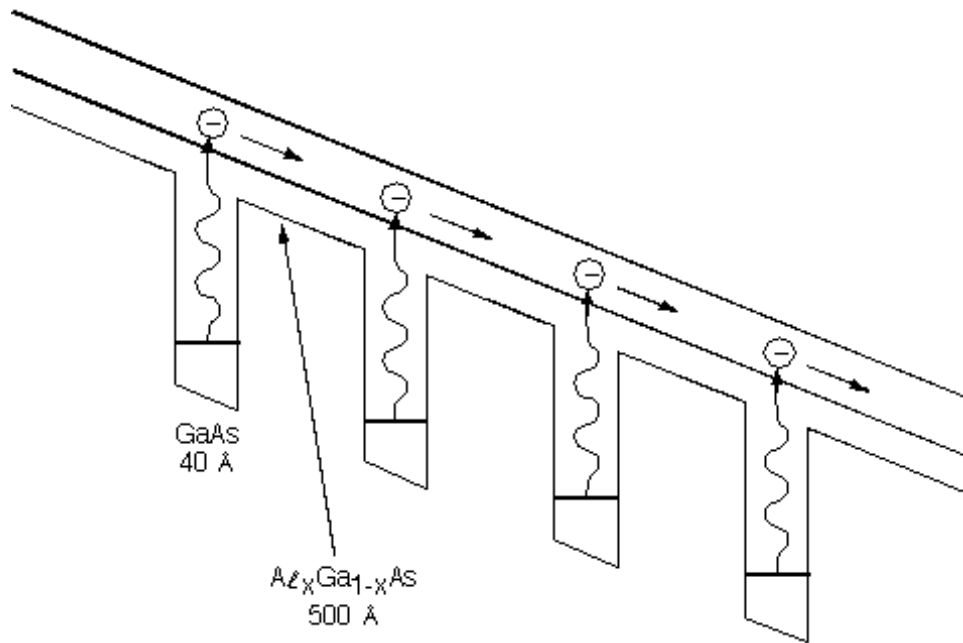


Fig. 4. Conduction-band diagram for a bound-to-continuum QWIP, showing the photoexcitation and hot-electron transport process. (Levine, 1993)

states without tunneling through the barrier as shown in Fig. 4. As a result, the bias required to efficiently collect the photoelectrons can be reduced dramatically, and hence lower the dark current. Due to the fact that the photoelectrons do not have to tunnel through the barriers, the $\text{Al}_x\text{Ga}_{1-x}\text{As}$ barrier thickness of bound-to-continuum QWIP can be increased without reducing the photoelectron collection efficiency. Increasing the barrier width from a few hundred Å to 500 Å can reduce the ground state sequential tunneling by an order of magnitude. By making use of these improvements, Levine *et al.*

(1990a) has successfully demonstrated the first bound-to-continuum QWIP with a dramatic improvement in the performance (i.e., detectivity $3 \times 10^{10} \text{ cm} \cdot \text{Hz/W}$ at 68 K for a QWIP which had cutoff wavelength at 10 μm).

2.3 n-Doped Bound-to-Quasibound QWIPs

Improving QWIP performance depends largely on minimizing the parasitic current (i.e., dark current) that plagues all light detectors. The dark current is the current that flows through a biased detector in the dark (i.e., with no photons impinging on it). As Gunapala and Bandara (1995) have discussed elsewhere, at temperatures above 45 K (typical for $\lambda < 14 \mu\text{m}$), the dark current of the QWIP is entirely dominated by classical thermionic emission of ground state electrons directly out of the well into the energy continuum. Minimizing the dark current is critical to the commercial success of the QWIP as it allows the highly-desirable high-temperature detector operation.

Therefore, Gunapala and Bandara (1995) have designed the *bound-to-quasibound* quantum well by placing the first excited state exactly at the well top as shown in Fig. 5. The best previous QWIPs pioneered by Levine *et al.* (1988c) at AT&T Bell Laboratories were of the bound-to-continuum variety, so-called because the first excited state was a continuum energy band above the quantum well top (typically 10 meV). Dropping the first excited state to the quantum well top causes the barrier to thermionic emission (roughly the energy height from the ground state to the well top) to be $\sim 10 \text{ meV}$ more in bound-to-quasibound QWIP than in the bound-to-continuum one, causing the dark current to drop significantly at elevated operating temperatures. The advantage of the bound-to-quasibound QWIP over the bound-to-continuum QWIP is that in the case of bound-to-quasibound QWIP the energy barrier for the thermionic emission is the same as it is for the photoionization as shown in Fig. 5 (Gunapala and Bandara, 1995). In the case of a bound-to-continuum QWIP the energy barrier for the thermionic emission is 10 - 15 meV less than the photoionization energy. Thus, the dark current of bound-to-quasibound QWIPs is reduced by an order of magnitude (i.e., $I_d \propto e^{-\frac{\Delta E}{kT}} \approx e^{-2}$ for $T = 55 \text{ K}$) as shown in Fig. 5.

2.4 n-Doped Broad-band QWIPs

A broad-band MQW structure can be designed by repeating a unit of several quantum wells with slightly different parameters such as quantum well width and barrier height. The first device structure (shown in Fig. 6) demonstrated by Bandara *et al.* (1998a) has 33 repeated layers of GaAs three-quantum-well units separated by $L_B \sim 575 \text{ \AA}$ thick $\text{Al}_x\text{Ga}_{1-x}\text{As}$ barriers (Bandara *et al.*, 1998b). The well thickness of the quantum wells of three-quantum-well units are designed to respond at peak wavelengths around 13, 14, and 15 μm respectively. These quantum wells are separated by 75 \AA thick $\text{Al}_x\text{Ga}_{1-x}\text{As}$

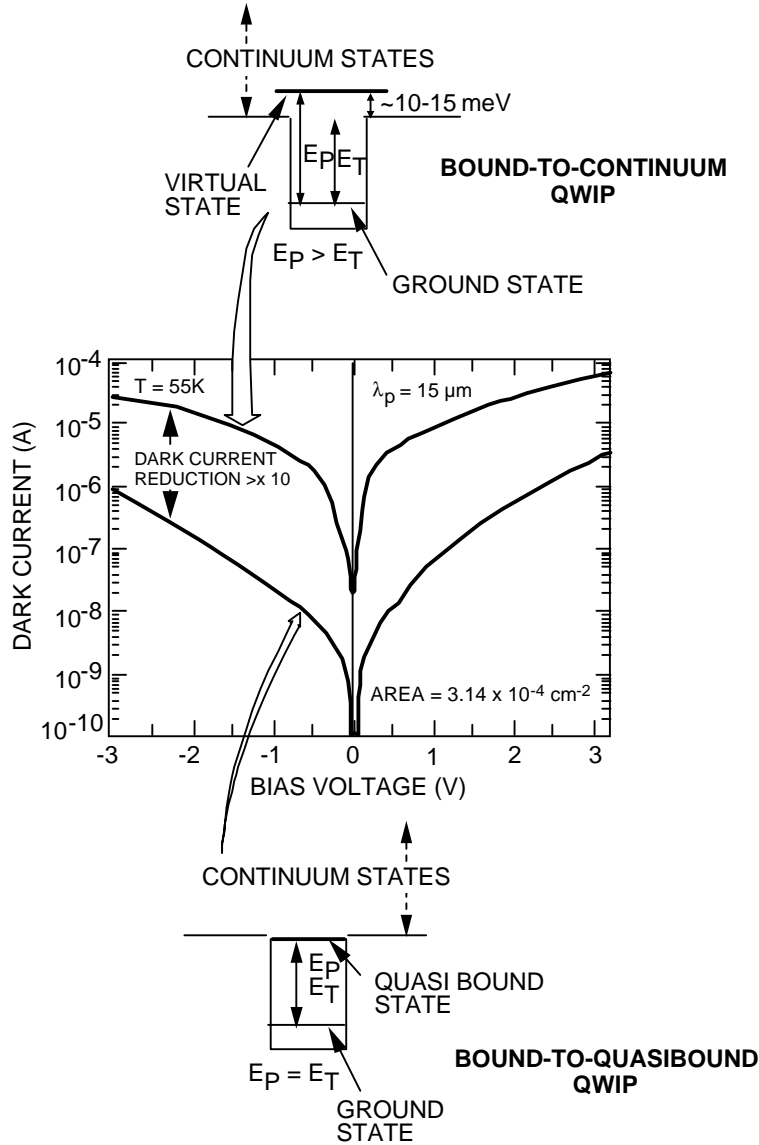


Fig. 5. Comparison of dark currents of bound-to-continuum and bound-to-quasibound VLWIR QWIPs as a function of bias voltage at temperature $T = 55$ K. (Gunapala *et al.*, 1997a)

barriers. The Al mole fraction (x) of barriers throughout the structure was chosen such that the $\lambda_p = 13 \mu\text{m}$ quantum well operates under bound-to-quasibound conditions. The excited state energy level broadening has further enhanced due to overlap of the wave functions associated with excited states of quantum wells separated by thin barriers. Energy band calculations based on a two band model shows excited state energy levels spreading about 28 meV. An experimentally measured responsivity curve at $V_B = -3$ V bias voltage has shown broadening of the spectral response up to $\lambda \sim 5.5 \mu\text{m}$, i.e. the full width at half maximum from 10.5-16 μm . This broadening $\lambda/\lambda_p \sim 42\%$ is about a 400 % increase compared to a typical bound-to-quasibound QWIP.

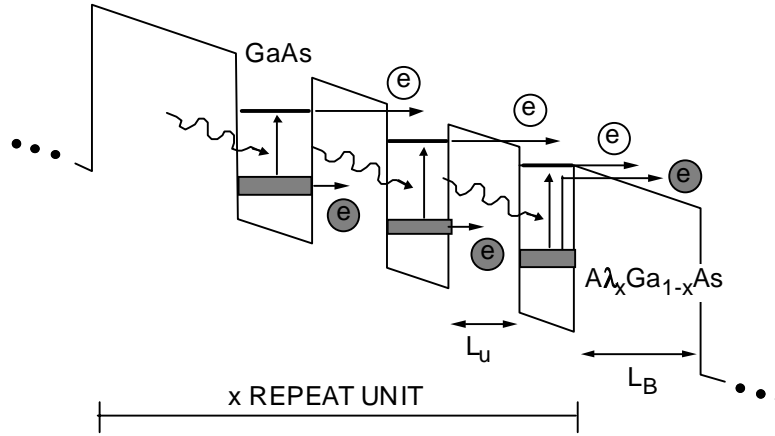


Fig. 6. Schematic diagram of the conduction band in broadband QWIP in an externally applied electric field. The device structure consists of 33 repeated layers of three-quantum-well units separated by thick $\text{Al}_x\text{Ga}_{1-x}\text{As}$ barriers. Also shown are the possible paths of dark current electrons and photocurrent electrons of the device under a bias (Bandara *et al.*, 1998b)

2.5 n-Doped Bound-to-Bound Miniband QWIPs

The superlattice miniband detector uses the concept of infrared photoexcitation between minibands (ground state and first excited state) and transport of these photoexcited electrons along the excited state miniband. When the carrier de Broglie wavelength becomes comparable to the barrier thickness of the superlattice, the wave functions of the individual wells tend to overlap due to tunneling, and energy minibands are formed. The miniband occurs when the bias voltage across one period of the superlattice becomes smaller than the miniband width (Capasso *et al.*, 1986).

Experimental work on infrared detectors involving the miniband concept was initially carried out by Kastalsky *et al.* (1988). The spectral response of this GaAs/AlGaAs detector was in the range 3.6-6.3 μm and indicated that low-noise infrared detection was feasible without the use of external bias. O *et al.* (1990) reported experimental observations and related theoretical analysis for this type of detectors with absorption peak in the LWIR spectral range (8-12 μm). Both these detectors consist of a bound-to-bound miniband transition (i.e., two minibands below the top of the barrier) and a graded barrier between the superlattice and the collector layer as a blocking barrier for ground-state miniband tunneling dark current.

In order to further reduce ground-state miniband tunneling dark current, Bandara *et al.* (1992) used a square step barrier at the end of the superlattice. This structure, illustrated in Fig. 7(a), was grown by MBE and consists of 50 periods of 90 \AA GaAs quantum wells and 45 \AA $\text{Al}_{0.21}\text{Ga}_{0.79}\text{As}$ barriers. A 600 \AA $\text{Al}_{0.15}\text{Ga}_{0.85}\text{As}$ blocking layer was designed so that it has two minibands below the top of the barrier with the top of the step blocking barrier being lower than the bottom of the first excited state miniband, but higher than the top of the ground state miniband. The spectral photoresponse was measured at 20 K with a 240 mV bias voltage across the detector and at 60 K with a 200 mV bias voltage. The experimental response band of this detector was in the VLWIR range with peak response

at 14.5 μm . The rapid fall-off in the photocurrent at higher bias voltage values was observed and attributed to the progressive decoupling of the miniband as well as the rapid decrease in the impedance of the detector.

The peak responsivity of this detector at 20 K and 60 K are 97 and 86 mA/W for unpolarized light. Based on these values and noise measurements, the estimated detectivity at 20 K and 60 K are 1.5×10^9 and 9×10^8 $\text{cm} \cdot \text{Hz/W}$, respectively. Although this detector operates under a modest bias and power conditions, the demonstrated detectivity is relatively lower than the responsivity of usual QWIPs. This is mainly due to lower collection efficiency. Although there is enough absorption between minibands, only photoexcited electrons in few quantum wells near the collector contact contribute to the photocurrent.

2.6 n-Doped Bound-to-Continuum Miniband QWIPs

It is anticipated that placing the excited state miniband in the continuum levels would improve the transportation of the photoexcited electrons, i.e., responsivity of the detector. This is same as in the case of the wide barrier bound-to-continuum detectors discussed previously. A detector based on photoexcitation from a single miniband below the top of the barriers to one above the top of the barriers is expected to show a higher performance. Gunapala *et al.* (1991b) proposed and demonstrated this type of bound-to-continuum miniband photoconductor based on $\text{GaAs}/\text{Al}_x\text{Ga}_{1-x}\text{As}$ superlattice operating in the 5-9 μm spectral range. Their structure shows more than an order of magnitude improvement in electron transport and detector performance, compared with previous bound-to-bound state miniband detectors.

Device structures [as shown in Fig. 7(b)] studied by Gunapala *et al.* (1991b) consisted of 100 periods of GaAs quantum wells of either $L_b = 30 \text{ \AA}$ or $L_b = 45 \text{ \AA}$ barriers of $\text{Al}_{0.28}\text{Ga}_{0.72}\text{As}$, and $L_w = 40 \text{ \AA}$ GaAs wells (doped $N_D = 1 \times 10^{18} \text{ cm}^{-3}$) sandwiched between doped GaAs contact layers. The absolute values for the peak absorption coefficients are $\alpha = 3100 \text{ cm}^{-1}$ and $\alpha = 1800 \text{ cm}^{-1}$ for the $L_b = 30$ and 45 \AA structures, respectively. The structure with narrower barrier ($L_b = 30 \text{ \AA}$) has a higher peak absorption coefficient as well as a broader spectrum, resulting in significantly larger integrated absorption strength. Also, the dark current of this structure ($L_b = 30 \text{ \AA}$) is much larger than that of the other ($L_b = 45 \text{ \AA}$) structure.

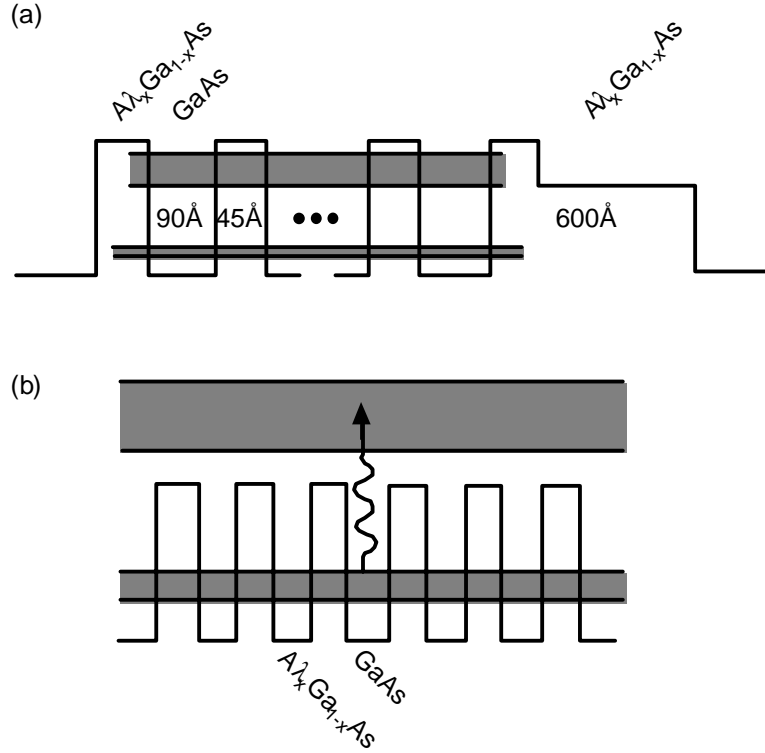


Fig. 7(a). Parameters and band diagram for LWIR GaAs/A λ_x Ga $_{1-x}$ As superlattice miniband detector with $\lambda_c \sim 15 \mu\text{m}$. (Bandara *et al.*, 1988); (b) device structure of bound-to-continuum miniband (Gunapala *et al.*, 1991b)

Detectivities at peak wavelength for the above miniband detectors were calculated using measured responsivities and dark currents. For the $L_b = 30 \text{ \AA}$ structure the result was $D^* = 2.5 \times 10^9$ and $5.4 \times 10^{11} \text{ cm} \cdot \text{Hz/W}$ for $T = 77$ and 4 K at -80 mV bias. For $L_b = 45 \text{ \AA}$ structure, they obtained $D^* = 2.0 \times 10^9$ and $2.0 \times 10^{10} \text{ cm} \cdot \text{Hz/W}$ for $T = 77$ and 4 K at -300 mV bias. These values are significantly larger than the previous bound-to-bound miniband results. Although the responsivity is improved by placing the excited state in the continuum, it also increases the thermionic dark current because of the lower barrier height. This fact is more critical for LWIR detectors because the photoexcitation energy becomes even smaller, i. e., the detector operating temperature will be lowered.

2.7 n-Doped Bound-to-Miniband QWIPs

Yu *et al.* (1991a, 1991b) proposed and demonstrated a miniband transport QWIP which contained two bound states with higher energy level being resonance with the ground state miniband in the superlattice barrier. [see Fig. 8(a)]. In this approach, infrared radiation is absorbed in the doped quantum wells, exciting an electron into the miniband and transporting it in the miniband until it is collected or recaptured into another quantum well. Thus, the operation of this miniband QWIP is analogous to that of a weakly coupled MQW bound-to-continuum QWIP. In this device structure, the continuum states above the barriers are replaced by the miniband of the superlattice barriers. These miniband QWIPs show lower photoconductive gain than bound-to-continuum QWIPs because the

photoexcited electron transport occurs in the miniband where electrons have to transport through many thin heterobarriers resulting in lower mobility. The band width of the absorption spectrum is controlled by the position of the miniband, relative to the barrier threshold, as well as the width of the miniband which is exponentially dependent on the thickness of the superlattice barriers. Faska *et al.* (1992) adopted this bound-to-miniband approach and demonstrated excellent LWIR images from a 256x256 focal plane array (FPA) camera. These bound-to-miniband QWIPs have been demonstrated using a GaAs/Al_xGa_{1-x}As material system. In order to further improve performance (by decreasing dark current) of these miniband QWIPs, Yu *et al.* (1992) proposed a step bound-to-miniband QWIP which is shown in Fig. 8(b). This structure consists of GaAs/Al_xGa_{1-x}As superlattice barriers and In_{0.07}Ga_{0.93}As strained quantum wells which are deeper than superlattice barrier wells, as shown in Fig. 8(b) (Li *et al.*, 1993).

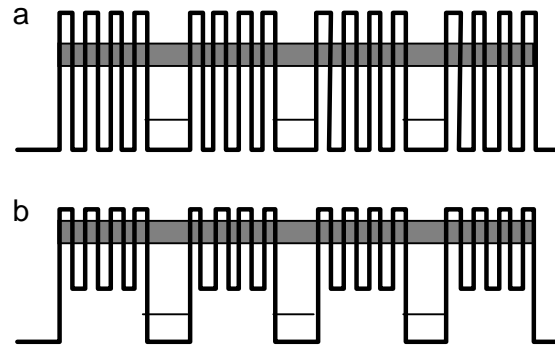


Fig. 8. Band diagrams for (a) bound-to-miniband; (b) step bound-to-miniband QWIP structures. (Levine, 1993)

2.8. n-Doped Asymmetrical GaAs/Al_xGa_{1-x}As QWIPs

For typical QWIP structures with symmetrical rectangular wells, the electric field shift of intersubband absorption is relatively small, since the linear shift term is forbidden by symmetry. This was demonstrated by Harwit *et al.* (1987) who obtained a shift of less than 2 meV for a field of 36 kV/cm across a symmetrical QWIP structure. Large stark shifts can be obtained by designing QWIP structures with asymmetrical quantum wells such as stepped well. Martinet *et al.* (1992) have demonstrated a linear stark shift of ~10 meV for an electric field shift of ~15 kV/cm, while Mii *et al.* (1989) measure a shift of 8 meV at 18 kV/cm. These shifts are an order of magnitude larger than that for the symmetrical rectangular well in the same electrical field. In addition to absorption spectral changes due to asymmetrical wells or barriers in the structure, there will be much stronger bias-dependent behavior in escape probability, photoconductive gain and, in the responsivity spectrum.

By introducing a QWIP structure with asymmetrical barriers, Levine *et al.* (1990c) demonstrated an electrically tunable photodetector without sacrificing the responsivity. Laco *et al.* (1992) demonstrated a large difference in spectral width and cutoff wavelength by using graded barrier QWIP with much stronger (81 meV) grading in the

barrier. They also find that the responsivity spectral line width is much narrower ($\Delta\lambda < 1 \mu\text{m}$) and the cutoff wavelength much shorter ($\lambda_c = 7.6 \mu\text{m}$) in the negative bias direction where the QWIP operates on a bound-to-bound transition, compared to the broad ($\Delta\lambda = 6 \mu\text{m}$) longer-wavelength cutoff ($\lambda_c = 11.4 \mu\text{m}$) positive bias bound-to-continuum transition. Levine *et al.* (1991c) have also discussed LWIR photoinduced charge polarization and storage in graded asymmetrical quantum wells. They have studied the long-wavelength photoinduced charge polarization and electron storage produced by infrared induced intersubband absorption in highly asymmetrical graded quantum wells. At zero bias a large photovoltage is observed, while at high bias the charge transfer probability approached unity.

2.9 p-Doped QWIPs

Levine *et al.* (1991b) experimentally demonstrated the first QWIP that used hole intersubband absorption in the GaAs valence band. The strong mixing (Chang *et al.*, 1989; Chiu *et al.*, 1983; Karunasiri *et al.*, 1990; Pinczuk *et al.*, 1986; Wieck *et al.*, 1984) between the light and heavy holes (at $k \neq 0$) allows the desired normal incidence illumination geometry to be used. The samples were grown on a (100) semi-insulating GaAs substrate, using gas source MBE, and consisted of 50 periods of $L_w=30 \text{ \AA}$ (or $L_w=40 \text{ \AA}$) quantum wells (doped $N_D = 4 \times 10^{18} \text{ cm}^{-3}$ with Be) separated by $L_b=300 \text{ \AA}$ barriers of $\text{Al}_{0.3}\text{Ga}_{0.7}\text{As}$, and capped by $N_D = 4 \times 10^{18} \text{ cm}^{-3}$ contact layers.

The unpolarized responsivity spectra of the $L_w=40 \text{ \AA}$ QWIP are compared for the two geometries (i.e., 45° and normal incidence as discussed in Section 4). The two spectra are essentially identical (peak wavelength $\lambda_p = 7.2 \mu\text{m}$ and long wavelength cutoff $\lambda_c = 7.9 \mu\text{m}$) and the normal incidence responsivity is larger than that of 45° illumination which is consistent with both polarizations contributing to the photoresponse. The peak unpolarized responsivities (for the $L_w=40 \text{ \AA}$ sample at $\lambda_p=7.2 \mu\text{m}$ and $V_b=+4 \text{ V}$) are $R_p = 39 \text{ mA/W}$ and 35 mA/W for normal and 45° incidence, respectively, which are approximately an order of magnitude smaller than the responsivities for n-QWIPs. As a further test of polarization behavior, Levine *et al.* (1991b) found that by using the 45° geometry, s-polarized light had twice the photoresponse of p-polarization. This is again in strong contrast with n-QWIPs for which the s-polarized photoresponse is forbidden by symmetry. A comparison between the $L_w = 30$ and 40 \AA detectors shows that, as expected, the narrower well QWIP has a broader spectral response ($\lambda_c=8.6 \mu\text{m}$) due to the excited state being pushed further up into the continuum and thereby broadening the absorption (Levin *et al.*, 1989). The 30 \AA well detector also has a slightly longer peak wavelength ($\lambda_p=7.4 \mu\text{m}$), consistent with the ground state being pushed up even further than the excited state. Similar lineshape effects (Levine *et al.*, 1989) have been seen in n-QWIPs. Peak detectivity $D_\lambda^*=1.7 \times 10^{10} \text{ cm} \cdot \text{Hz/W}$ and $D_\lambda^*=3.5 \times 10^9 \text{ cm} \cdot \text{Hz/W}$ were measured at $T=77 \text{ K}$ for $L_w=30 \text{ \AA}$ and 40 \AA detectors respectively.

The experimentally measured photoconductive gains are $g = 3.4 \times 10^{-2}$ and $g = 2.4 \times 10^{-2}$ for

$L_w = 30$ and 40 \AA , respectively. This yields hot hole mean free path $L = 510$ and 360 \AA for the two samples (i.e., photoexcited carrier travels only one or two periods before being recaptured). It should be noted that both g and L are over an order of magnitude smaller than the corresponding values for n-QWIPs [where photoconductive gains of $g \approx 1$ have been obtained (Levine *et al.*, 1990a)]. Since $L = v_s \tau_r$ [where τ_r is the well recapture time (Levine *et al.*, 1992b)], we can see that the lower g is due to a lower velocity associated with the higher hole effective mass, and a shorter lifetime due to increased scattering between the light and heavy hole bands. Having now obtained g , we can relate it to the peak responsivity, and thus using the measured values for R_p and g directly determine the low temperature quantum efficiency. This yields double pass values of $\eta = 17\%$ and 28% for the $L_w = 30$ and 40 \AA QWIPs, respectively. Thus, in spite of the larger effective mass of the holes compared to that of electrons, the different symmetry (normal incidence) of the intersubband absorption, and the much smaller photoconductive gain and mean free path, the quantum efficiency (and hence escape probability) for bound-to-continuum n- and p-QWIPs are similar.

2.10 Single Quantum Well Infrared Photodetectors

Although there has been extensive research on MQW infrared photodetectors which typically contain many (~ 50) periods, there has been relatively limited experimental work (Liu *et al.*, 1991a, 1991b; Rosencher *et al.*, 1992) done on QWIPs containing only a single quantum well. Bandara *et al.* (1993a, 1993b, 1993c) have performed a complete series of experiments on single quantum well structures with n-type doped well, un-doped well, and p-type doped well. These doped-single well detectors are, in fact, particularly interesting since they have exceptionally high photoconductive gain compared to MQW detectors. In addition, their simple band structures allow accurate calculations of the bias voltage dependence of the potential profiles for each of the two barriers, band bending effects in the contacts, as well as charge accumulation (or depletion) in the quantum well.

2.11 Indirect Band-gap QWIPs

Infrared detectors operating in the MWIR spectral range ($\lambda \sim 3\text{-}5 \text{ \mu m}$) are also of interest due to the atmospheric window in this wavelength range. However, the short wavelength limit in the GaAs/ $\text{Al}_x\text{Ga}_{1-x}\text{As}$ materials system imposed by keeping the $\text{Al}_x\text{Ga}_{1-x}\text{As}$ barriers direct is $\lambda = 5.6 \text{ \mu m}$. That is, if the Al concentration x is increased beyond $x = 0.4$ the indirect X valley becomes the lowest band gap. This has been thought to be highly undesirable since Γ -X scattering together with GaAs X-barrier trapping can result in inefficient carrier collection and, thus, poor responsivity. However, in view of technology advantages in the more mature GaAs/ $\text{Al}_x\text{Ga}_{1-x}\text{As}$ material system, it would be highly desirable to design detectors using indirect $\text{Al}_x\text{Ga}_{1-x}\text{As}$. Levine *et al.* (1991a) successfully demonstrated the first bound-to-continuum GaAs/ $\text{Al}_x\text{Ga}_{1-x}\text{As}$ indirect band-gap QWIP operating at $\lambda_p = 4.2 \text{ \mu m}$.

A single period of the structure (Levine *et al.*, 1991a) consists of $L_w = 30 \text{ \AA}$ of GaAs

(doped $n = 1 \times 10^{18} \text{ cm}^{-3}$) and 500 Å of undoped $\text{Al}_{0.55}\text{Ga}_{0.45}\text{As}$. This is repeated 50 times and is sandwiched between a 0.5 μm top and 1 μm bottom contact layer (also doped $n = 1 \times 10^{18} \text{ cm}^{-3}$). The conduction band diagram under bias for the structure is shown in Fig. 9. The solid line in Fig. 9 is the Γ -valley band edge and the dotted line is that of the X valley. The Γ -barrier height of $E_b^\Gamma = 452 \text{ meV}$ results in a calculated single bound Γ state at an energy $E_0^\Gamma = 165 \text{ meV}$, and an optical absorption peak (from E_0^Γ to the excited continuum state E_1^Γ) at an energy of $\Delta E_{01}^\Gamma = 289 \text{ meV}$ (i.e., 2 meV above E_b^Γ) corresponding to a calculated absorption peak at $\lambda_p = 4.3 \text{ μm}$.

• •

Fig. 9. Schematic conduction band diagram of indirect $\text{Al}_{0.55}\text{Ga}_{0.45}\text{As}$ barrier QWIP. The solid lines are the direct Γ -valley band edge while the dashed lines are the indirect X-band edge. (Levine *et al.*, 1991a)

The bias dependence of R at $\lambda_p = 4.2 \text{ μm}$ has also been measured (Levine *et al.*, 1991a) and found to have significant zero bias photovoltaic effect with $R_p = 0.05 \text{ A/W}$ at $V_b = 0$. This yields the photoconductive gain of $g = 3.0$ and 1.0 for $V_b = 4$ and -4V , respectively, and (using the superlattice length $l = 2.65 \text{ μm}$) the corresponding values of the hot electron mean free path $L = 8.0$ and 2.65 μm . These large values for g and L are comparable to (or even larger than) the best results in the usual Γ direct gap devices (Hasnain *et al.*, 1990b; Levine *et al.*, 1990a) and thus confirm excellent transport and efficient carrier collection expected in this indirect barrier QWIP. That is, this large mean free path is due to the difficulty of an X electron being captured by a Γ well. The peak detectivity D_λ^* at $V_b = -1 \text{ V}$ and $T = 77 \text{ K}$ is $D_\lambda^* = 4 \times 10^{10} \text{ cm} \cdot \text{Hz/W}$. However, an even larger value $D_\lambda^* = 1.1 \times 10^{12} \text{ cm} \cdot \text{Hz/W}$ is obtained at zero bias [determined by the Johnson noise generated by QWIP differential resistance (Levine *et al.*, 1991a)]. This large D^* is comparable to that obtained using the direct-gap material $\text{In}_{0.53}\text{Ga}_{0.47}\text{As}/\text{In}_{0.52}\text{Al}_{0.48}\text{As}$ which is discussed in the next subsection.

2.12 n-doped $\text{In}_{0.53}\text{Ga}_{0.47}\text{As}/\text{In}_{0.52}\text{Al}_{0.48}\text{As}$ QWIPs

In order to shift the intersubband absorption resonance into the higher energy spectral region ($\lambda = 3\text{--}5\ \mu\text{m}$), Levine *et al.* (1988a) have investigated lattice matched quantum well superlattices of $\text{In}_{0.53}\text{Ga}_{0.47}\text{As}/\text{In}_{0.52}\text{Al}_{0.48}\text{As}$ grown using MBE on an InP substrate and reported intersubband absorption in this heterosystem. This direct gap heterostructure has conduction band discontinuity of 550 meV, which is significantly higher than that of the direct gap $\text{GaAs}/\text{Al}_x\text{Ga}_{1-x}\text{As}$ system, therefore allowing for shorter wavelength operation.

A 50-period MQW superlattice consisting of $\text{In}_{0.53}\text{Ga}_{0.47}\text{As}$ wells (doped $N_D = 1 \times 10^{18}\ \text{cm}^{-3}$) having a width $L_w = 50\ \text{\AA}$, and $150\ \text{\AA}$ barriers of $\text{In}_{0.52}\text{Al}_{0.48}\text{As}$, was grown on an InP substrate. The experimental absorption peak is at $\lambda = 4.4\ \mu\text{m}$, in good agreement with the theoretical estimation of the energy separation of bound states [see reference (Levine *et al.*, 1988a) for details]. In order to achieve higher performances in the MWIR range, Hasnain *et al.* (1990a) designed a MQW structure of the same materials system involving bound-to-continuum intersubband absorption. This structure consisting of 50 periods of $30\ \text{\AA}$ $\text{In}_{0.53}\text{Ga}_{0.47}\text{As}$ wells (doped $N_D = 2 \times 10^{18}\ \text{cm}^{-3}$) and $300\ \text{\AA}$ $\text{In}_{0.52}\text{Al}_{0.48}\text{As}$ barriers, was grown by MBE on an InP substrate. The absorption spectrum is peaked at 279 meV ($\lambda = 4.4\ \mu\text{m}$) with a full width at half maximum of 93 meV. Although the peak absorption of this bound-to-continuum detector is 4.2 times lower than that of a bound-to-bound detector (Levine *et al.*, 1988a) the line width is five times greater. Thus, it has comparable (20% higher) absorption strength covering the full 3-5 μm MWIR band. The noise measured in these MQW detectors at 500 Hz corresponds to the shot noise of the dark current resulting peak detectivity at 77 K of $D^* = 1.5 \times 10^{12}\ \text{cm}^2\ \text{Hz/W}$ with a background limited (for a 180° field of view) $D_{BL}^* = 2.3 \times 10^{10}\ \text{cm}^2\ \text{Hz/W}$ at 120 K and lower temperatures. These values are comparable to those demonstrated with the Pt-Si devices (Sheperd *et al.*, 1988) presently used in MWIR band.

2.13 n-doped $\text{In}_{0.53}\text{Ga}_{0.47}\text{As}/\text{InP}$ QWIPs

An InGaAs/InP materials system has been used extensively for optical communication devices and therefore has a highly developed growth and processing technology. Since the quality of barriers is extremely important for optimum QWIP performance, and InP is binary, whereas $\text{Al}_x\text{Ga}_{1-x}\text{As}$ is a ternary alloy, Gunapala *et al.* (1991a) investigated the hot electron transport and performance of detectors fabricated from these two materials. Two structures were grown by metal organic molecular beam epitaxy (MOMBE) with arsine and phosphine as group V sources, trimethylindium and trimethylgallium as group III sources, and elemental Sn as n-type dopant sources (Gunapala *et al.*, 1991a; Ritter *et al.*, 1991). The first structure consisted of 20 periods of $L_w = 60\ \text{\AA}$ $\text{In}_{0.53}\text{Ga}_{0.47}\text{As}$ quantum wells lattice matched to $500\ \text{\AA}$ InP barriers. A second sample contained 50 periods of $L_w = 50\ \text{\AA}$ $\text{In}_{0.53}\text{Ga}_{0.47}\text{As}$ wells separated by $500\ \text{\AA}$ InP barriers. These MQWs were doped $N_D = 5 \times 10^{17}\ \text{cm}^{-3}$, and had top and bottom $0.4\ \mu\text{m}$ contact layers of $N_D = 1 \times 10^{18}\ \text{cm}^{-3}$ doped $\text{In}_{0.53}\text{Ga}_{0.47}\text{As}$. The intersubband absorption was measured on a 45° multipass

waveguide. The peak ($\lambda_p = 8.1 \mu\text{m}$) room temperature absorption coefficient $\alpha = 950 \text{ cm}^{-1}$ is expected to increase by a factor of 1.3 at $T=77 \text{ K}$ resulting in a low temperature quantum efficiency of $\eta = 12\%$ (Gunapala *et al.*, 1991a). For the 50 \AA well QWIP, the corresponding value is $\eta = 11\%$. These values are quite comparable to those of GaAs samples, when the lower doping level of $N_D = 5 \times 10^{17} \text{ cm}^{-3}$ in the wells is taken into account.

The bias dependence of the responsivities (which was essentially independent of temperature $T = 10\text{-}80 \text{ K}$) was measured. Extremely large values of the responsivity, reaching $R = 6.5 \text{ A/W}$ at $V_b = +3.5 \text{ V}$ and $R = 3.5 \text{ A/W}$ at $V_b = -3.5 \text{ V}$ has been observed. This responsivity is five times larger than that of similar GaAs/ $\text{Al}_x\text{Ga}_{1-x}\text{As}$ QWIPs which demonstrates the excellent transport in this materials system. These large responsivity values yield very large values of photoconductive gain of $g = 9.0$ for $V_b = +3.5 \text{ V}$ and $g = 4.8$ for $V_b = -3.5 \text{ V}$ (Gunapala *et al.*, 1991a). The corresponding value of the hot electron mean free path is $L = 10 \mu\text{m}$ at $V_b = +3.5 \text{ V}$, which is five times larger than that for similar GaAs/ $\text{Al}_x\text{Ga}_{1-x}\text{As}$ QWIPs. This excellent transport may be associated with the high quality binary InP barriers, and higher mobility of InP compared with $\text{Al}_x\text{Ga}_{1-x}\text{As}$. The calculated peak detectivity $D_\lambda^* = 9 \times 10^{10} \text{ cm} \cdot \text{Hz/W}$ based on noise current and measured responsivity at $V_b = +1.2 \text{ V}$ and $T = 77 \text{ K}$ of 60 \AA QWIP compares favorably with GaAs/ $\text{Al}_x\text{Ga}_{1-x}\text{As}$ QWIPs operating at this wavelength. Jelen *et al.*, (1998a, 1998b) also investigated lattice matched InGaAs/InP QWIPs and observed large photoconductive gain indicating improved transport properties in the binary InP barrier. (Jelen *et al.*, 1998a, 1998b)

2.14 InGaAsP - quaternary QWIPs

In the GaAs/ $\text{Al}_x\text{Ga}_{1-x}\text{As}$ system, transport properties of $\text{Al}_x\text{Ga}_{1-x}\text{As}$ can be affected by oxygen related defects, and sometimes preferred elevated growth temperatures could result in undesirable dopant diffusion. Also, aluminum oxidation restricts fabrication methods such as epitaxial regrowth. Gunapala *et al.* (1991c, 1992a) investigated QWIP structures based on quaternary, $\text{Ga}_{1-x}\text{In}_x\text{As}_y\text{P}_{1-y}$ materials grown in a VG-V80H system modified for metal organic molecular beam epitaxy on semi-insulating (100) InP wafers. These structures consisted of InGaAsP quantum wells, lattice matched to 500 \AA InP barriers. The quantum wells were n-type doped with $N_D = 5 \times 10^{17} \text{ cm}^{-3}$ and sandwiched between $0.4 \mu\text{m}$ $\text{In}_{0.53}\text{Ga}_{0.47}\text{As}$ contact layers of $N_D = 1 \times 10^{18} \text{ cm}^{-3}$. The responsivity spectra peaked at wavelengths of $\lambda_p = 8.6$, $\lambda_p = 11.0 \mu\text{m}$ ($L_w = 54 \text{ \AA}$) and $\lambda_p = 12.1 \mu\text{m}$ ($L_w = 63 \text{ \AA}$) with $\lambda_c = 9.4 \mu\text{m}$, $\lambda_c = 12.5$ and $13.2 \mu\text{m}$ respectively have been observed. The responsivities were measured and results are approximately twice as large as the responsivity of similar GaAs/ $\text{Al}_x\text{Ga}_{1-x}\text{As}$ QWIPs. These results clearly demonstrate the excellent hot electron transport in this materials system. It should also be noted, that this large maximum responsivity is still two times smaller than that of InGaAs/InP QWIPs previously discussed. This reduction of responsivity can be attributed to an increase in scattering and hence reduction in photoconductive gain of the quaternary GaInAsP

material. The peak detectivities are comparable to GaAs/Al_xGa_{1-x}As detectors operating at similar wavelengths. Hoff *et al.* (1995a, 1995b) also, investigated p-doped QWIP based on quaternary, Ga_{1-x}In_xAs_yP_{1-y} materials. Extensive theoretical modeling and experimental measurements have been carried out on QWIPs with different combinations of the above materials system. Both p-doped binary-quaternary QWIP (GaAs/Ga_{0.71}In_{0.29}As_{0.39}P_{0.61}) and p-doped quaternary-ternary QWIP (Ga_{0.87}In_{0.13}As_{0.74}P_{0.26}/Ga_{0.51}In_{0.49}P) shows spectral coverage from 4 - 6 μm and background limited performances at T = 100 K (Hoff *et al.*, 1995a, 1995b).

2.15 n-doped GaAs/Ga_{0.5}In_{0.5}P QWIPs

In a GaAs/Ga_{0.5}In_{0.5}P materials system, Ga_{0.5}In_{0.5}P acts as the barrier material for the transport of electrons with an effective mass similar to that of Al_{0.3}Ga_{0.7}As. Therefore, Gunapala *et al.* (1990a) investigated this lattice-matched GaAs/Ga_{0.5}In_{0.5}P MQW structure grown on a GaAs substrate as an alternative system to GaAs/Al_xGa_{1-x}As for LWIR detection. In addition, these infrared photoconductive measurements have allowed us to accurately determine the GaAs/Ga_{0.5}In_{0.5}P band offset.

The QWIP structure consisting of ten periods of 40Å GaAs quantum wells (doped $N_D = 2 \times 10^{18} \text{ cm}^{-3}$) and 300Å of undoped Ga_{0.5}In_{0.5}P barriers grown by atmospheric pressure metal organic vapor phase epitaxy (MOVPE) at a substrate temperature of 675° C on a semi-insulating undoped GaAs substrate. The absorption spectrum is peaked at 8 μm (155 meV) with a full-width at half-maximum of 82 meV, i.e., $\Delta\lambda/\lambda = 53\%$. The measured responsivity spectrum is also peaked at 8 μm , where the room temperature absorption peaked, but the width decreases from $\Delta\lambda/\lambda = 53\%$ to 21%. The measured peak responsivity is 0.34 A/W corresponding to a photoconductive gain of $g = 0.86$.

In order to determine the lattice-matched GaAs/Ga_{0.5}In_{0.5}P conduction band offset ΔE_c , we calculated the position and bandwidth of the low temperature absorption spectrum and adjusted the quantum well depth (i.e., ΔE_c) to fit the experiment. The theory includes both non-parabolicity as well as the exchange interaction. The exchange effect is significant and lowers the bound-state energy level (Bandara *et al.*, 1988; Choe *et al.*, 1990) by 19 meV for a doping density of $N_D = 2 \times 10^{18} \text{ cm}^{-3}$. From these results the conduction band offset ΔE_c was determined to be $221 \pm 15 \text{ meV}$. From the known band gaps of GaAs and Ga_{0.5}In_{0.5}P, the band gap difference $\Delta E_g = 483 \text{ meV}$ was obtained, and thus from $\Delta E_c + \Delta E_v = \Delta E_g = 483 \text{ meV}$, we determine that $\Delta E_v = 262 \pm 15 \text{ meV}$. Also, Jelen *et al.* (1997) have demonstrated a 15 μm cutoff wavelength (13 μm detection peak) QWIP fabricated using n-type GaAs/Ga_{0.5}In_{0.5}P materials and fabrication of a preliminary FPA camera has been carried out.

2.16 n-doped GaAs/Al_{0.5}In_{0.5}P QWIPs

The GaAs/(Al_xGa_{1-x})_{0.5}In_{0.5}P quaternary has a direct Γ - valley band gap from $x=0$ to

$x=0.7$ which then becomes an indirect X-valley conduction band from $x=0.7$ to $x=1$ (Watanabe *et al.*, 1987). The limiting composition GaAs/Al_{0.5}In_{0.5}P heterobarrier (although having an indirect gap) has a very large Γ -valley conduction band discontinuity of $\Delta E_c \sim 0.5$ eV (Watanabe *et al.*, 1987). Thus makes this an interesting system for short wavelength QWIPs. A MQW structure was grown on a GaAs substrate via gas-source MBE. It consisted of 20 periods of 30 Å doped ($N_D = 1 \times 10^{18} \text{ cm}^{-3}$) quantum wells of GaAs and 500 Å barriers of undoped Al_{0.5}In_{0.5}P, surrounded by GaAs contact layers (doped $N_D = 2 \times 10^{18} \text{ cm}^{-3}$). The responsivity measured on a 45° polished QWIP had a narrow spectral shape ($\Delta\lambda/\lambda = 12\%$ indicating a nearly resonant bound-to-bound transition) and peaked at $\lambda_p = 3.25 \text{ }\mu\text{m}$. The fact that this $\lambda \approx 3 \text{ }\mu\text{m}$ QWIP is grown lattice matched to a GaAs substrate means that it can be integrated with a long-wavelength GaAs/Al_xGa_{1-x}As QWIP ($\lambda = 6\text{--}20 \text{ }\mu\text{m}$), grown on the same wafer, allowing for the fabrication of monolithic multi-color infrared detectors.

2.17 n-doped In_{0.15}Ga_{0.85}As/GaAs QWIPs

For all of the GaAs based QWIPs which have been demonstrated thus far, GaAs is the low bandgap well material and the barriers are lattice matched Al_xGa_{1-x}As, Ga_{0.5}In_{0.5}P or Al_{0.5}In_{0.5}P. However, it is interesting to consider GaAs as the barrier material since the transport in binary GaAs is expected to be superior to that of a ternary alloy, as was previously found to be the case in the In_{0.53}Ga_{0.47}As/InP binary barrier structures (Gunapala *et al.*, 1991a, 1992a). To achieve this, Gunapala *et al.* (1994a) have used the lower bandgap non-lattice matched alloy In_xGa_{1-x}As as well material, together with GaAs barriers. Band edge discontinuities and critical thicknesses of quantum well structures of this materials system have been studied earlier (Andersson *et al.*, 1988; Yao *et al.*, 1991). It has been demonstrated (Elman *et al.*, 1989; Zhou *et al.*, 1989) that strain layer heterostructures can be grown for lower In concentrations ($x < 0.2$) which results in lower barrier heights. Therefore, this heterobarrier system is very suitable for very long-wavelength ($\lambda > 14 \text{ }\mu\text{m}$) QWIPs.

In order to further investigate this materials system, Gunapala *et al.* (1994b) have used three samples which have been designed to give a very wide variation in QWIP absorption and transport properties. Detector A was designed to have an intersubband infrared absorption transition occurring between a single localized bound state in the quantum well and a delocalized state in the continuum (Levine *et al.*, 1990a; Steele *et al.*, 1991). Detector C was designed with a wider well width $L_w = 70 \text{ }\text{\AA}$, yielding two bound states in the well. Therefore, the intersubband transition is from the bound ground state to the bound excited state and requires electric field assisted tunneling for the photoexcited carrier to escape into the continuum (Choi *et al.*, 1987b; Levine *et al.*, 1987a). Due to the low effective mass of the electrons in the GaAs barriers, the electric field required for the field assisted tunneling is expected to be smaller in these structures in comparison with the usual GaAs/Al_xGa_{1-x}As QWIP structures. Detector B was designed such that the second bound level is resonant with the conduction band of the GaAs barrier. Thus, the intersubband transition is from the bound ground state to the quasibound excited state

which is intermediate between a strongly bound excited state and a weakly bound continuum state.

The responsivities of samples A, B and C peak at 12.3, 16.0 and 16.7 μm respectively. The absolute peaked responsivities (R_p) of the detectors were A, B and C are 293, 510 and 790 mA/W respectively at bias $V_b = 300$ mV. As expected, the responsivity spectra of the bound-to-continuum QWIP (detector A) is much broader than the bound-to-bound (detector C) or bound-to-quasibound (detector B) QWIPs. Correspondingly, the magnitude of the peak absolute responsivity (R_p) is significantly lower than that of the bound-to-bound or bound-to-quasibound QWIPs, due to reduction of the absorption coefficient α . This reduction in the absorption coefficient is a result of the conservation of oscillator strength. These peak wavelengths and spectral widths are in good agreement with theoretical estimates of bound-to-continuum and bound-to-bound intersubband transition based on the 55% conduction band offset ($\Delta E_c / E_g$) of the GaAs/In_{0.2}Ga_{0.8}As materials system (i.e. $\Delta E_v / E_g = 45\%$). The large responsivity and detectivity D_λ^* values are comparable to those achieved with the usual lattice matched GaAs/Al_xGa_{1-x}As materials system (Levine *et al.*, 1992a). The high photoconductive gains and the small carrier capture probabilities demonstrate the excellent carrier transport of the GaAs barriers and the potential of this heterobarrier system for VLWIR ($\lambda > 14$ μm) QWIPs.

2.18 p-doped In_{0.53}Ga_{0.47}As/InP QWIPs

In Section 2.9, we discussed the GaAs/Al_xGa_{1-x}As QWIPs which are based on hole intersubband absorption in p-doped GaAs quantum wells. Due to the complex GaAs valence band interactions at the non-zero wave vector, the infrared absorption at normal incidence is allowed. Also, in Sections 2.13 and 2.14 we have indicated that due to the high quality InP barriers, n-doped lattice matched In_{0.53}Ga_{0.47}As/InP and InGaAsP/InP QWIPs have even larger responsivities than GaAs/Al_xGa_{1-x}As n-QWIPs. Therefore, Gunapala *et al.* (1992b) have investigated the p-QWIPs in a lattice matched In_{0.53}Ga_{0.47}As/InP materials system.

Since most of the GaAs/Al_xGa_{1-x}As band gap discontinuity is in the conduction band (i.e., $\Delta E_c / E_g = 65\%$), whereas in In_{0.53}Ga_{0.47}As/InP most of the band gap difference is in the valence band (i.e., $\Delta E_v / E_g = 60\%$), the In_{0.53}Ga_{0.47}As/InP p-QWIP intersubband absorption occurs at a much shorter wavelength. The GaAs p-QWIPs discussed previously (Section 2.9), operated with a peak wavelength of $\lambda_p = 7.2\text{--}7.4$ μm and a cutoff wavelength of $\lambda_c = 7.9\text{--}8.6$ μm . In strong contrast, the In_{0.53}Ga_{0.47}As/InP p-QWIPs discussed here have a responsivity peaked at $\lambda_p = 2.7$ μm . This is, in fact, the shortest wavelength QWIP ever reported.

The devices discussed below were grown using MOMBE and consisted of 20 periods of 25 Å quantum wells of In_{0.53}Ga_{0.47}As (doped $N_D = 2 \times 10^{18}$ cm⁻³ with Be) and 500 Å

slightly p-doped barriers of InP. This slight p-doping is necessary to compensate for the n-background ($N_D \approx 4 \times 10^{16}$) of the InP barriers. Otherwise, n-InP and p-InGaAs result in a series of p-n junctions which would significantly reduce the available carriers in the quantum well, and thus lower the infrared absorption. In addition, the p-n junctions would increase the series resistance and thus impede the transport. These MQWs were sandwiched between $\text{In}_{0.53}\text{Ga}_{0.47}\text{As}$ contact layers (0.4 μm top and bottom) having the same doping as the wells.

The responsivity spectrum demonstrates the shortest wavelength QWIP ever reported with a responsivity peak at $\lambda_p = 2.7 \mu\text{m}$ and a cutoff wavelength of $\lambda_c = 3.0 \mu\text{m}$ (the long-wavelength side where the responsivity drops to half of its peak value). The peak unpolarized responsivity, at normal incidence, is $R_p = 29 \text{ mA/W}$ at $V_b = +3 \text{ V}$ (corresponding to a double optical pass through the QWIP). This value is essentially unchanged from $T = 20$ to 80 K . The unpolarized responsivity measured using the 45° polished substrate control detector was nearly identical, with $R_p = 31 \text{ mA/W}$, for the same conditions. This is in good agreement with the $\text{GaAs}/\text{Al}_x\text{Ga}_{1-x}\text{As}$ p-QWIPs discussed in the Section 2.9, where both the magnitude and spectral shape of the normal incidence and 45° responses were also very similar. It is worth noting that there is a zero bias responsivity of $R_p = 6 \text{ mA/W}$, which also peaked at $\lambda_p = 2.7 \mu\text{m}$. The peak detectivity for this unoptimized device was $D_\lambda^* = 3 \times 10^{10} \text{ cm}^2 \text{ Hz/W}$ at $T = 77 \text{ K}$. Later, Sengupta *et al.* (1996) has shown similar device performance of QWIPs based on the same material system.

3. FIGURES OF MERIT

Now we will discuss and compare the optical and transport properties of bound-to-continuum QWIPs, bound-to-bound QWIPs, and bound-to-quasibound QWIPs with each other. The structures of the six samples to be discussed are listed in Table I. These n-doped QWIPs were grown using MBE and the wells and contact layers were doped with Si. The quantum well widths L_w range from 40 \AA to 70 \AA , while the barrier widths are approximately constant at $L_b = 500 \text{ \AA}$. The Al molar fraction, in the $\text{Al}_x\text{Ga}_{1-x}\text{As}$ barriers, varies from $x = 0.10$ to 0.31 (corresponding to cutoff wavelengths of $\lambda_c = 7.9 - 19 \mu\text{m}$). The photosensitive doped MQW region containing 25 to 50 periods is sandwiched between similarly doped top (0.5 μm) and bottom (1 μm) ohmic contact layers. These structural parameters have been chosen to give a very wide variation in QWIP absorption and transport properties (Levine *et al.*, 1992b). In particular, samples A through D are n-doped with intersubband infrared transition occurring between a single localized bound state in the well and a delocalized state in the continuum (denoted B-C in Table I) (Levine *et al.*, 1987d, 1990a, 1991e; Andersson *et al.*, 1991b; Andrews and

Table I. Structure parameters for samples A-F, including quantum well width L_w , barrier width L_b , $\text{Al}_x\text{Ga}_{1-x}\text{As}$ composition x , doping density N_D , doping type, number of MQW periods, and type of intersubband transition *bound-to-continuum* (B-C), *bound-to-bound* (B-B), and *bound-to-quasibound* (B-QB). (Levine *et al.*, 1992a)

Sample	L_w (Å)	L_b (Å)	x	N_D (Å) (10^{18}cm^{-3})	Doping Type	Periods	Intersubband Transition
A	40	500	0.26	1.0	n	50	B-C
B	40	500	0.25	1.6	n	50	B-C
C	60	500	0.15	0.5	n	50	B-C
D	70	500	0.10	0.3	n	50	B-C
E	50	500	0.26	1.4	n	25	B-B
F	45	500	0.30	0.5	n	50	B-QB

Miller, 1991; Janousek *et al.*, 1990; Kane *et al.*, 1989; Steele *et al.*, 1991; Wu *et al.*, 1992). Sample E has a high Al concentration $x = 0.26$ coupled with a wide well $L_w = 50$ Å, yielding two bound states in the well. Thus, the intersubband transition from the bound ground state to the bound first excited state, (denoted B-B in Table I), and therefore requires electric field assisted tunneling for the photoexcited carrier to escape into the continuum as discussed in the previous section (Levine *et al.*, 1987b, 1989; Choi *et al.*, 1987b). Sample F was designed to have a quasibound excited state [denoted B-QB in Table I (Kiledjian *et al.*, 1991; Gunapala and Bandara, 1995)], which is intermediate between a strongly bound excited state and weakly bound continuum state. It consists of a $L_w = 45$ Å doped quantum well and 500 Å of a $\text{Al}_x\text{Ga}_{1-x}\text{As}$ barrier with $x = 0.3$. These quantum well parameters result in a first excited state in resonance with the barriers, and is thus expected to have an intermediate behavior.

3.1 Absorption spectra

The infrared absorption spectra for samples A-F were measured at room temperature, using a 45• multipass waveguide geometry (except for sample D which was at such a long-wavelength, that the substrate multiphonon absorption obscured the intersubband transition). As can be readily seen in Fig. 10 , the spectra of the bound-to-continuum QWIPs (samples A, B, and C) are much broader than the bound-to-bound or bound-to-quasibound QWIPs (samples E and F or the QWIPs discussed in the previous section). Correspondingly, the magnitude of the absorption coefficient α for the continuum

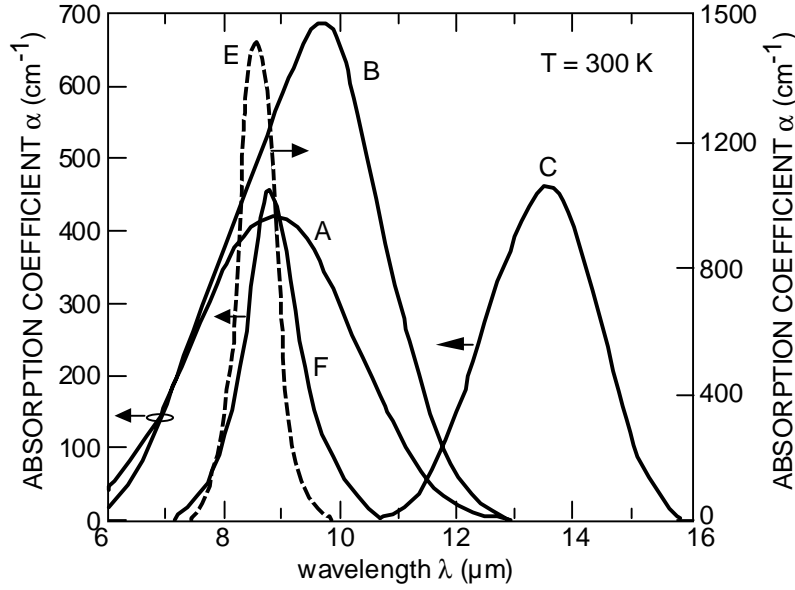


Fig. 10. Absorption coefficient spectra Vs wavelength measured at $T=300$ K for samples A, B, C, E, and F. (Levine *et al.*, 1992a)

QWIPs (left-hand scale) is significantly lower than that of the bound-to-bound QWIPs (right-hand scale), due to the conservation of oscillator strength. That is, $\alpha_p (\Delta\lambda/\lambda)/N_D$ is a constant, as was previously found (Gunapala *et al.*, 1990b). The values of the peak room temperature absorption α_p , peak wavelength λ_p , cutoff wavelength λ_c (long wavelength λ for which α drops to half- α_p) and spectral width $\Delta\lambda$ (full width at half α_p) are given in Table II. The room temperature absorption quantum efficiency η_a (300 K) evaluated from α_p (300 K) using

$$\eta_a = \frac{1}{2}(1 - e^{-2\alpha_p l}) \quad (3)$$

Table II. Optical absorption parameters for samples A, B, C, E, and F, including peak absorption wavelength λ_p , long wavelength cutoff λ_c , spectral width $\bullet \lambda$, fractional spectral width $\bullet \lambda/\lambda$, peak room temperature absorption coefficient α_p (300 K), peak room temperature absorption quantum efficiency η_a (300 K), T = 77 K absorption quantum efficiency η_a (77 K), and maximum high bias net quantum efficiency η_{\max} . (Levine *et al.*, 1992a)

Sample	λ_p (μm)	λ_c (μm)	$\bullet \lambda$ (μm)	$\bullet \lambda/\lambda$ (%)	α_p (300 K) (cm^{-1})	η_a (300 K) (%)	η_a (77 K) (%)	η_{\max} (%)
A	9.0	10.3	3.0	33	410	10	13	16
B	9.7	10.9	2.9	30	670	15	19	25
C	13.5	14.5	2.1	16	450	11	14	18
E	8.6	9.0	0.75	9	1490	17	20	23
F	8.9	9.4	1.0	11	451	11	14	20

where η_a is the unpolarized double-pass absorption quantum efficiency, where l is the length of the photosensitive region, and the factor of two in the denominator is a result of the quantum mechanical selection rules, which only allows the absorption of radiation polarized in the growth direction. The low temperature quantum efficiency $\eta_a(77)$ was obtained by using $\alpha_p(77 \text{ K}) \bullet 1.3 \alpha_p(300 \text{ K})$ as previously discussed. The last column containing η_{\max} will be discussed later.

In order to clearly compare the line shapes of the bound, quasibound, and continuum QWIPs, the absorption coefficients for samples A, E, and F have been normalized to unity and plotted as $\tilde{\alpha}$ in Fig. 11, and the wavelength scale has been normalized by plotting the spectra against $\bullet \lambda \equiv (\lambda - \lambda_p)$, where λ_p is the wavelength at the absorption peak. The very large difference in spectral width is apparent with the bound and continuum excited state transitions ($\bullet \lambda/\lambda = 9\%-11\%$) being 3-4 times narrower than for the continuum excited state QWIPs ($\bullet \lambda/\lambda = 33\%$).

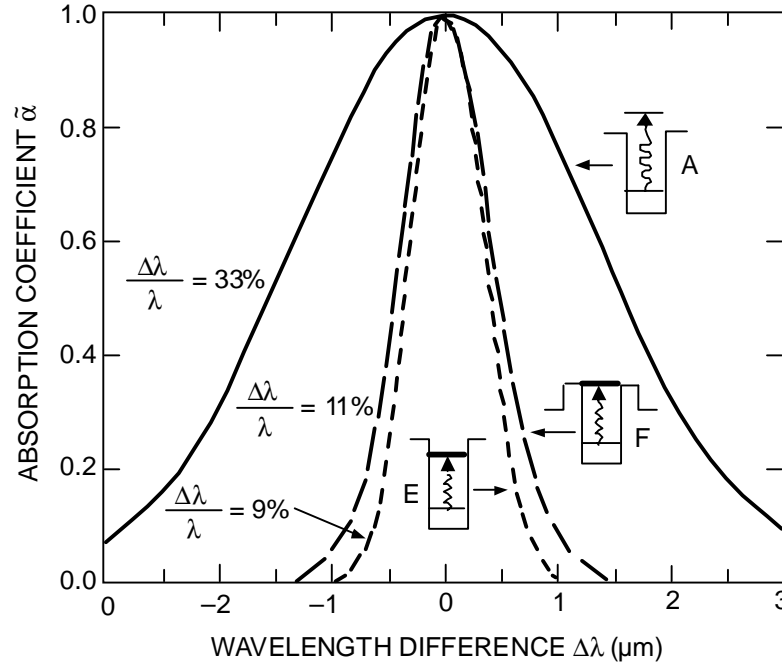


Fig. 11. Normalized absorption spectra Vs wavelength difference $\Delta\lambda = (\lambda - \lambda_p)$. The spectral width $\Delta\lambda/\lambda$ are also given. The insert show the schematic conduction band diagram for sample A (bound-to-continuum), sample E (bound-to-bound), and sample F (bound-to-quasibound). (Levine *et al.*, 1992a)

3.2 Dark current

In order to measure the dark current-voltage curves, 200 μm diam mesas were fabricated as described elsewhere (Gunapala and Bandara, 1995) and the results are shown in Fig. 12 for $T = 77\text{ K}$. Note that the asymmetry in the dark current (Zussman *et al.*, 1991) with I_d being larger for positive bias (i.e., mesa top positive) than for negative bias. This can be attributed to the dopant migration in the growth direction (Liu *et al.*, 1993), which lowers the barrier height of the quantum wells in the growth direction compared to the quantum well barriers in the other direction (which are unaffected). Note that, as expected, the dark current I_d increases as the cutoff wavelength λ_c increases. At bias $V_b = -1\text{ V}$ and 1 V , the curves for samples E and F cross. This is due to the fact that even though sample E has a shorter cutoff wavelength than sample F, it is easy for the excited electrons to tunnel out at sufficiently high bias. In contrast, sample F has a quasibound excited state, which is in resonance with the $L_b = 500\text{ \AA}$ thick barrier top.

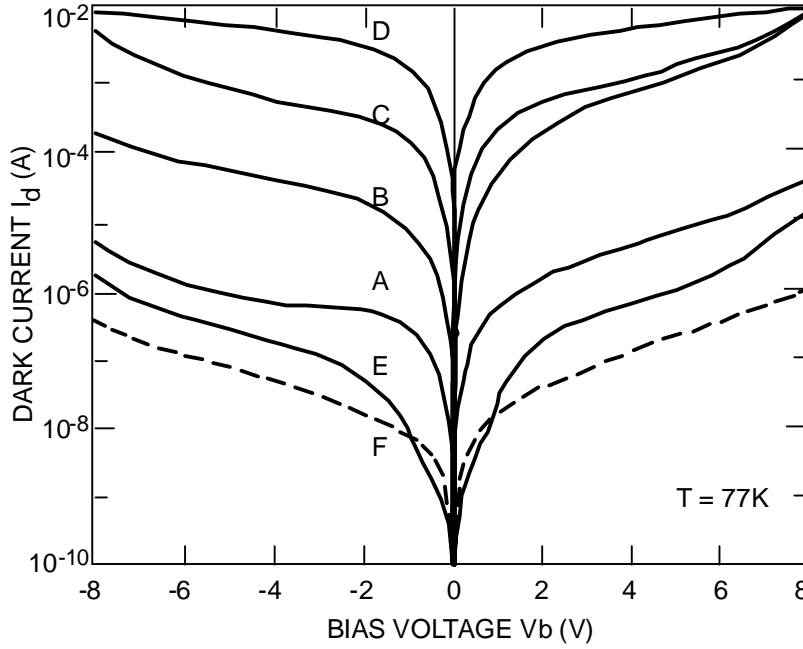


Fig. 12. Dark current I_d as a function of bias voltage V_b at $T=77$ K for samples A-F. (Levine *et al.*, 1992a)

Levine *et al.* (1990a) has analyzed the origin of the dark current in detail and shown that thermionic-assisted tunneling is a major source of dark current (Gunapala *et al.*, 1990b; Kinch and Yariv, 1989; Pelve *et al.*, 1989; Zussman *et al.*, 1991; Andrews and Miller, 1991). In that analysis, they first determine the effective number of electrons $n(V)$, which are thermally excited out of the well into the continuum transport states, as a function of bias voltage V ;

$$n(V) = \left(\frac{m^*}{\pi \eta^2 L_p} \right) \int_{E_0}^{\infty} f(E) T(E, V) dE \quad (4)$$

where the first factor containing the effective mass m^* is obtained by dividing the two-dimensional density of states by the superlattice period L_p (to convert it into an average three-dimensional density), and where $f(E)$ is the Fermi factor $f(E) = [1 + \exp((E - E_0 - E_F)/kT)]^{-1}$, E_0 is the ground state energy, E_F is the two-dimensional Fermi level, and $T(E, V)$ is the bias-dependent tunneling current transmission factor for a single barrier which can be calculated using Wentzel-Kramers-Brillouin (WKB) approximation to a biased quantum well. Equation (4) accounts for both thermionic emission above the energy barrier E_b (for $E > E_b$) and thermionically assisted tunneling (for $E < E_b$). Then they calculated the bias dependent dark current $I_d(V)$ using $I_d(V) = n(V)ev(V)A$, where e is the electronic charge, A is the area of the detector, and v is the average transport velocity given by

$$v(V) = \mu F [1 + (\mu F / v_s)^2]^{-\frac{1}{2}} \quad (5)$$

where μ is the mobility, F is the average electric field, and v_s is the saturated drift velocity. The good agreement is achieved as a function of both bias voltage and temperature over a range of eight orders of magnitude in dark current (Levine *et al.*, 1990a).

3.3 Responsivity

The responsivity spectra $R(\lambda)$ were measured (Zussman *et al.*, 1991) on 200 μm diam. mesa detectors using a polished 45° incident facet on the detector, together with a global source and a monochromator. A dual lock-in ratio system with a spectrally flat pyroelectric detector was used to normalize the system spectral response due to wavelength dependence of the blackbody, spectrometer, filters, etc. The absolute magnitude of the responsivity was accurately determined by measuring the photocurrent I_p with a calibrated blackbody source. This photocurrent is given by

$$I_p = \int_{\lambda_1}^{\lambda_2} R(\lambda) P(\lambda) d\lambda \quad (6)$$

where λ_1 and λ_2 are the integration limits that extend over the responsivity spectrum, and $P(\lambda)$ is the blackbody power per unit wavelength incident on the detector, which is given by

$$P(\lambda) = W(\lambda) \sin^2(\theta/2) A F \cos \phi \quad (7)$$

where A is the detector area, ϕ is the angle of incidence, θ is the optical field of view angle (i.e., $\sin^2(\theta/2) = (4f^2 + 1)^{-1}$ where f is the f number of the optical system; in this case θ is defined by the radius ρ of the blackbody opening at a distance D from the detector, so that $\tan(\theta/2) = \rho/D$), F represents all coupling factors and $F = T_f(1-r)C$ where T_f is the transmission of filters and windows, $r = 28\%$ is the reflectivity of the GaAs detector surface, C is the optical beam chopper factor ($C = 0.5$ in an ideal optical beam chopper), and $W(\lambda)$ is the blackbody spectral density given by the following equation (i.e., the power radiated per unit wavelength interval at wavelength λ by a unit area of a blackbody at temperature T_B).

$$W(\lambda) = (2\pi c^2 h / \lambda^5) (e^{hc/\lambda k T_B} - 1)^{-1} \quad (8)$$

By combining equations (6) and (7), and using $R(\lambda) = R_p \tilde{R}(\lambda)$, where R_p is the peak responsivity and $\tilde{R}(\lambda)$ is normalized (at peak wavelength λ_p) experimental spectral responsivity, we can rewrite the photocurrent I_p as

$$I_p = R_p G \int_{\lambda_1}^{\lambda_2} \tilde{R}(\lambda) W(\lambda) d\lambda \quad (9)$$

where G represents all the coupling factors and is given by $G = \sin^2(\theta/2) A F \cos \phi$. Thus, by measuring the $T_B = 1000$ K blackbody photocurrent, R_p can be accurately determined.

The normalized responsivity spectra $\tilde{R}(\lambda)$ are given in Fig. 13 for samples A-F, where we again see that the bound and quasibound excited state QWIPs (samples E and F) are much narrower • $\lambda/\lambda = 10\%-12\%$ than the continuum QWIPs • $\lambda/\lambda = 19\%-28\%$ (samples A-D). Table III gives the responsivity peak λ_p and cutoff wavelengths λ_c as well as the responsivity spectral width • λ . These responsivity spectral parameters are given in Table III and are similar to the corresponding absorption values listed in Table II.

The absolute peak responsivity R_p can be written in terms of quantum efficiency η and photoconductive gain g as

$$R_p = (e/h\nu) \eta g. \quad (10)$$

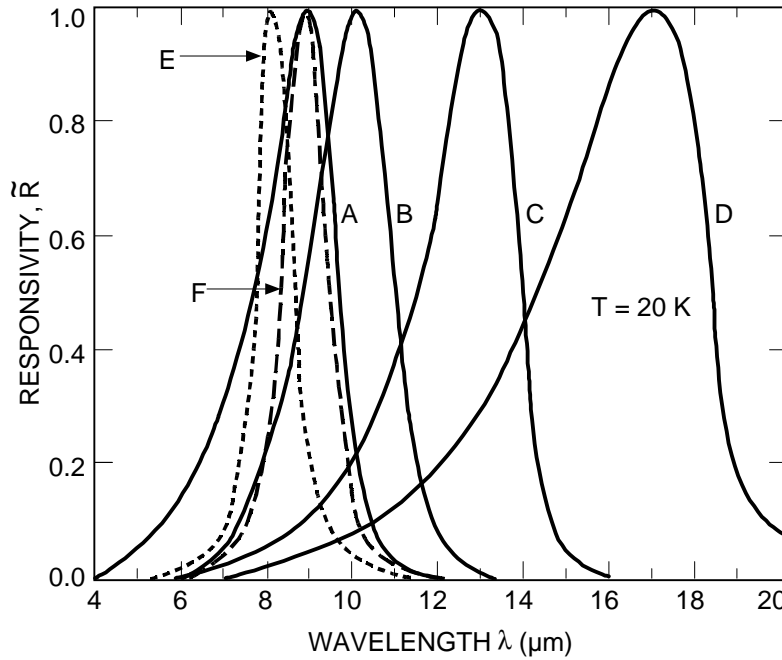


Fig. 13. Normalized responsivity spectra Vs wavelength measured at $T=20$ K for samples A-F. (Levine *et al.*, 1992a)

Table III. Responsivity spectral parameter for samples A-F, including peak responsivity wavelength λ_p , long wavelength cutoff λ_c , spectral width • λ , and fractional spectral width • λ/λ . (Levine *et al.*, 1992a)

Sample	λ_p (μm)	λ_c (μm)	$\bullet \lambda$ (μm)	$\bullet \lambda / \lambda$ (%)
A	8.95	9.8	2.25	25
B	9.8	10.7	2.0	20
C	13.2	14.0	2.5	19
D	16.6	19.0	4.6	28
E	8.1	8.5	0.8	10
F	8.4	8.8	1.0	12

Responsivity versus bias voltage curves for the bound, quasibound, and continuum, samples are shown in Fig. 14. Note that, at low bias, the responsivity is nearly linearly dependent on bias and it saturates at high bias. This saturation occurs due to the saturation of drift velocity. For the longest wavelength sample D, where $\lambda_c = 19 \mu\text{m}$, the dark current becomes too large at high bias to observe the saturation in R_p . The quasibound QWIP (sample F) behaves quite similarly to the bound QWIPs. The fully bound sample E has a significantly lower responsivity. The responsivity does not start out linearly with bias but is in fact zero for finite bias. That is, there is a zero bias offset, due to the necessity of field assisted tunneling for the photoexcited carrier to escape from the well (Levine *et al.*, 1987b, 1988b; Choi *et al.*, 1987b; Vodjdani *et al.*, 1991).

3.4 Dark current noise

The dark current noise i_n was measured on a spectrum analyzer for all of the samples at $T = 77 \text{ K}$ as a function of bias voltage (Zussman, *et al.*, 1991). The result for sample B is shown in Fig. 15. The solid circles were measured for negative bias (mesa top negative) while the open circles are for positive bias. The smooth curves are drawn through the experimental data. Note that the current shot noise for positive bias is much larger than that for negative bias (e.g., at $V_b = 3.5 \text{ V}$, it is 4 times larger). Also that near $V_b = 4 \text{ V}$ there is a sudden increase in the noise due to a different mechanism (possibly due to the avalanche gain (Levine *et al.*, 1987c) process). This asymmetry in the dark current noise is due to the previously mentioned asymmetry in I_d . The photoconductive gain g can now be obtained using the current shot noise expression (Levine *et al.*, 1990a; Liu, 1992a, 1992b; Beck, 1993; Hasnain *et al.*, 1990b)

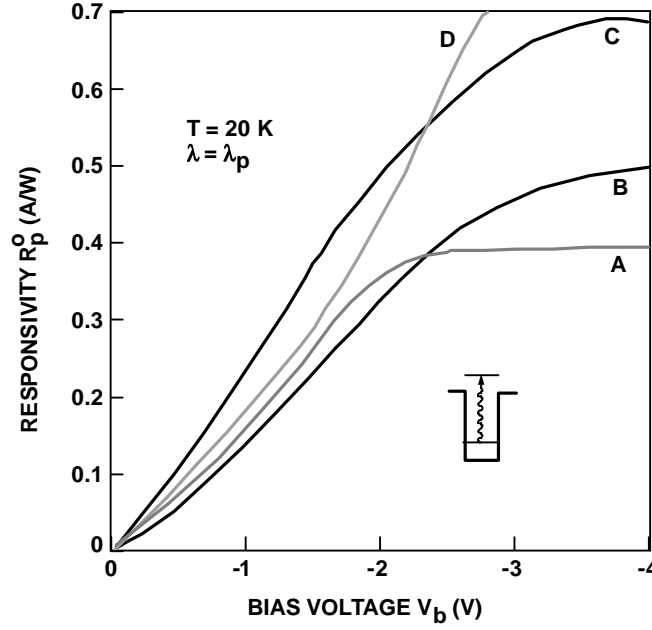


Fig. 14. Bias dependent peak ($\lambda = \lambda_p$) responsivity R_p^0 measured at $T=20$ K for samples A-F. The inserts show the conduction band diagrams. (Levine *et al.*, 1992a)

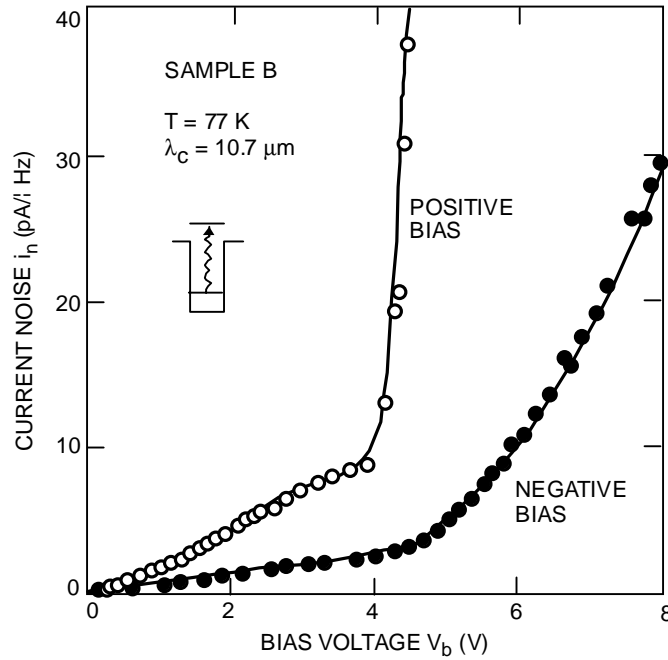


Fig. 15. Dark current noise i_n (at $T=77$ K) Vs bias voltage V_b for sample B. Both positive (open circles) and negative (solid circles) bias are shown. The smooth curves are drawn through the measured data. The insert shows the conduction band diagram. (Levine *et al.*, 1992a)

$$i_n = \sqrt{4eI_d g_n \Delta f}, \quad (11)$$

where Δf is the band width, (taken as $\Delta f = 1$ Hz).

3.5. Noise gain and Photoconductive gain

For a typical QWIP, where the dark current is dominated by thermionic emission, noise gain g_n and photoconductive gain g can be written in terms of well capture probability p_c (capture probability of electrons by the next period of the MQW) and the number of quantum wells N in the MQW region (Levine *et al.*, 1992a; Liu, 1992a, 1992b, Beck, 1993; Choi, 1994, 1996),

$$g_n = \frac{1 - p_c/2}{Np_c} \quad (12)$$

$$g = \frac{(1 - p_c)}{Np_c} \quad (13)$$

where p_c is capture probability of electrons by the next period of the MQW. Combining i_n from Fig. 15 and I_d from Fig. 12 allows the experimental determination of g as shown in Fig. 16. The solid circles are for negative bias while the open circles are for positive bias, and the smooth curves are drawn through the experimental points. As shown in Fig. 16, the photoconductive gain increases approximately linearly with the bias at low voltage and saturates near $V_b = 2$ V (due to velocity saturation) at $g \sim 0.3$. It is worth noting that, in spite of the large difference between the noise current i_n for positive and negative bias (as shown in Fig. 15), the photoconductive gains are quite similar. This demonstrates that, the asymmetry in i_n is due quantitatively to the asymmetry in I_d . It further shows that, although the number of carriers which escape from the well and enter the continuum [transmission factor, γ (Choi, 1996)] is strongly dependent on bias direction (due to the asymmetrical growth interfaces), the continuum transport (i.e., photoconductive gain), is less sensitive to the direction of carrier motion. The reason for this difference is that the transmission factor, γ (and hence I_d), depends exponentially on the bias, whereas photoconductive gain is only linearly dependent on bias V_b . The photoconductive gain of QWIPs can be written as (Kastalsky *et al.*, 1988; Hasnain, 1990)

$$g = L/l, \quad (14)$$

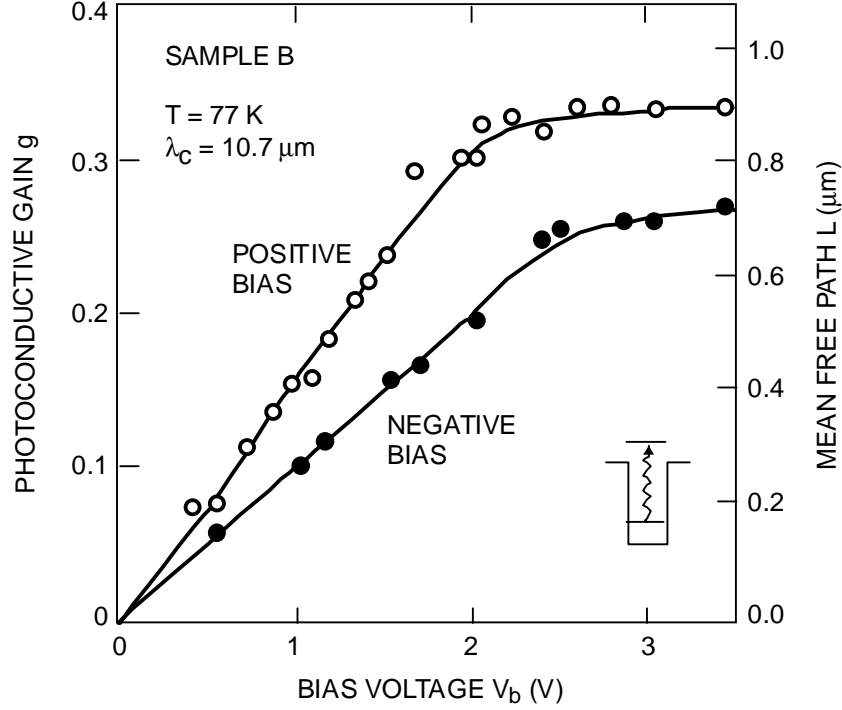


Fig. 16. Photoconductive gain g (left-hand scale) and hot electron mean free path L (right-hand scale) Vs bias voltage V_b for sample B at $T=77$ K. Both positive (open circles) and negative (solid circles) bias are shown. The smooth curves are drawn through the measured data. The insert shows the conduction band diagram. (Levine *et al.*, 1992a)

where L is the hot carrier mean free path and l is the superlattice length ($l = 2.7 \mu\text{m}$ for sample B). Therefore, we can evaluate L as shown on the right hand scale of Fig. 16. Thus, for this device L saturates at $\sim 1 \mu\text{m}$. As mentioned above, the dramatic increase in i_n near $V_b = 4$ V in Fig. 15 is due to additional noise mechanisms and, therefore, should not be attributed to a striking increase in g .

From the strong saturation of R_p for sample A (in Fig. 14) we would also expect the photoconductive gain to be completely saturated for $|V_b| > 2$ V, which is how we have drawn the smooth curve in Fig. 17. However, if one obtains g by simply substituting the measured i_n into equation 11, the result is the dotted line in Fig. 17. Interpreting the large excess noise i_n above 4 V in Fig. 15 as I_d shot noise would lead to an incorrectly large gain. Likewise, interpreting the low i_n above $V_b = -2$ V in Fig. 17 as due to a low gain would also be incorrect. Levine *et al.* (1992b) have explained this by attributing the excess noise at high bias to the ground state sequential tunneling, which is increasing the dark current I_d above that due to thermionic emission and thermionically assisted tunneling through the tip of the barriers. That is

$$I_{d,m} = I_{d,th} + I_{d,tu} \quad (15)$$

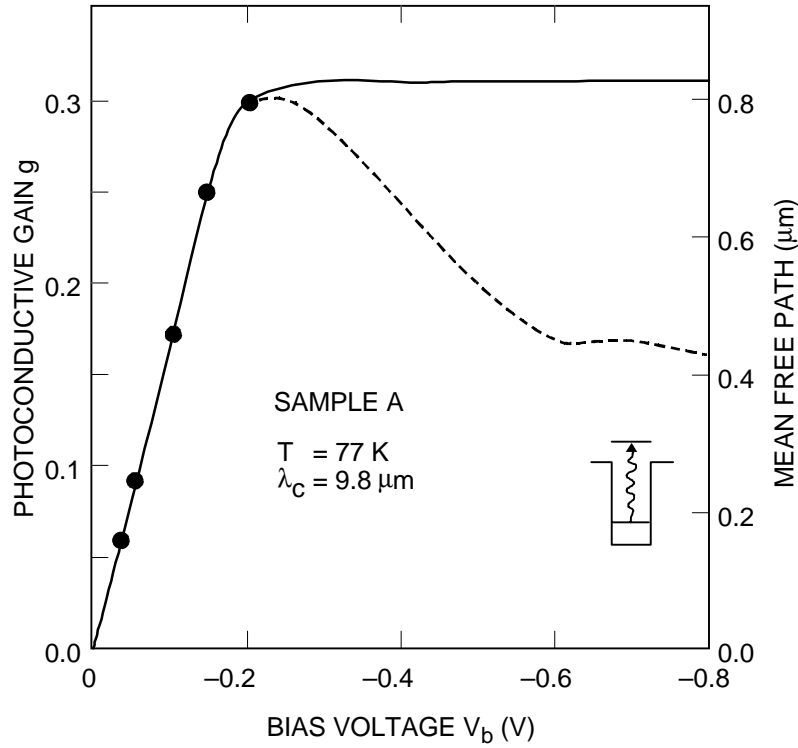


Fig. 17. Photoconductive gain g (left-hand scale) and hot electron mean free path L (right-hand scale) Vs bias voltage V_b for sample A at $T=77$ K. The solid curve drawn through the points is the correct interpretation; the dashed line is not. The insert shows the conduction band diagram. (Levine *et al.*, 1992a)

where $I_{d,m}$ is the total measured current, $I_{d,th}$ is the usual thermionic contribution, and $I_{d,tu}$ is the ground state tunneling current. It should be noted (Levine *et al.*, 1990a) that electrons near the top of the well, which contribute to the dark current $I_{d,tu}$, are the same as those which can transport in the continuum and thus contribute to the photocurrent I_p . In contrast, the electrons which contribute to the ground state tunneling current $I_{d,tu}$ do not enter the continuum, but sequentially tunnel from one well to the next (Choi *et al.*, 1987a). The gain associated with this process is $g_{tu} = L_p/l$ (where L_p is the superlattice period) and is very small compared with the usual continuum transport gain $g = L/l$. These two current processes lead to two contributions to the shot noise.

$$i_{dm}^2 = i_{dth}^2 + i_{dtu}^2 \quad (16)$$

By combining equations (11), (15) and (16) and using the fact that $g_{tu} \ll g$ we can write

$$g_m = (1-f)g \quad (17)$$

where g_m is the measured gain and $f \equiv I_{d,tu}/I_{d,m}$. Therefore, at high bias when the current contribution from sequential tunneling increases, the measured gain decreases, exactly as found in Fig. 17. A more general formula for noise gain was derived by Choi (1994,

1996) and Beck (1993) which incorporated tunneling and thermionic contributions of the dark current. Bandara *et al.* (1998b) have observed two different gain mechanisms associated with photocurrent electrons and dark current electrons, which transported in two different paths in a QWIP structure.

3.6 Quantum efficiency

By using equation (10), the bias dependent photoconductive gain (Figs. 16 and 17), and the responsivity (Fig. 14), we can now determine the total measured quantum efficiency η (Levine *et al.*, 1992a). The results of the continuum samples A-D are shown in Fig. 18.

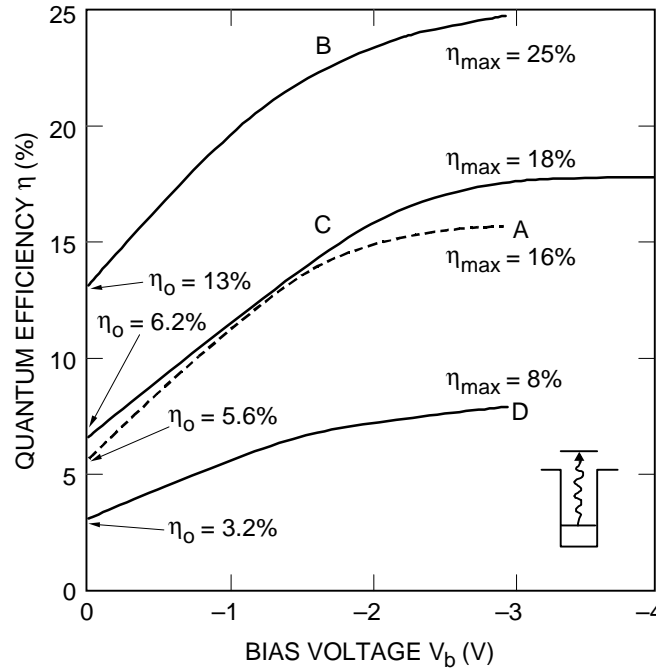


Fig. 18. Quantum efficiency η Vs bias voltage V_b (negative) for samples A-D. The zero bias quantum efficiencies η_0 and the maximum quantum efficiencies η_{\max} are shown. The insert shows the conduction band diagram. (Levine *et al.*, 1992a)

It is important to note that the total quantum efficiency does not vanish at zero bias but has a substantial value ranging from $\eta_0 = 3.2\%$ -13%, corresponding to a finite probability of escaping from the quantum well. As the bias is increased, quantum efficiency increases approximately linearly and then saturates at high bias reaching maximum values of $\eta_{\max} = 8\%$ -25%. The saturation values of the total quantum efficiencies are listed in Table II where they appear to be comparable with the values obtained from the zero bias absorption measurements η_a (77 K). The difference in these values [i.e., between η_{\max} and η_a (77 K)] can be attributed to lower measured gain as described in sub-section 3.5.

We now consider the bound and quasibound QWIPs (samples E and F). The photoconductive gains are plotted in Fig. 19, where they appear to be quite similar to the continuum QWIPs shown in Figs. 17, and the quantum efficiencies are shown in Fig. 20.

For these QWIPs (sample E and F), η is quite similar to that of continuum QWIPs (Fig. 18), having a saturation values at high bias voltages. However, the required bias voltage to reach the saturation value is higher for bound and quasibound QWIPs than that for the continuum QWIPs. Also, zero bias quantum efficiency of these QWIPs (sample E and F) have much lower values. These differences are due to the necessity of field assisted tunneling in order for the bound state excited photoelectrons to escape from the quantum well. This transmission factor (γ) can be included in the effective quantum efficiency (η) such that (Levine *et al.*, 1992b; Choi, 1996)

$$\eta = \gamma\eta_a \quad (18)$$

where η_a is the absorption quantum efficiency of the MQW structure. In this case, responsivity (R) and photoconductive gain (g) are related by $R = e\eta g/h\nu$, where $h\nu$ is the photoexcitation energy. Also, this transmission factor can be included in the optical gain (g_o) which is defined (Choi, 1996) as $g_o = \gamma g$, and as a result, $R_p = e\eta_a g_o/h\nu$.

Typically, γ of bound-to-continuum detectors is larger than γ of bound-to-bound detectors, and has a weaker bias voltage dependence. This is to be expected since the photoexcited carriers in bound-to-continuum QWIPs are above the top of the barriers and, thus, readily escape before being recaptured. However, the bound-to-bound QWIP is quite different due to the necessity of field assisted tunneling in order for excited photoelectrons to escape from the quantum well (Levine *et al.*, 1992b; Choi, 1996).

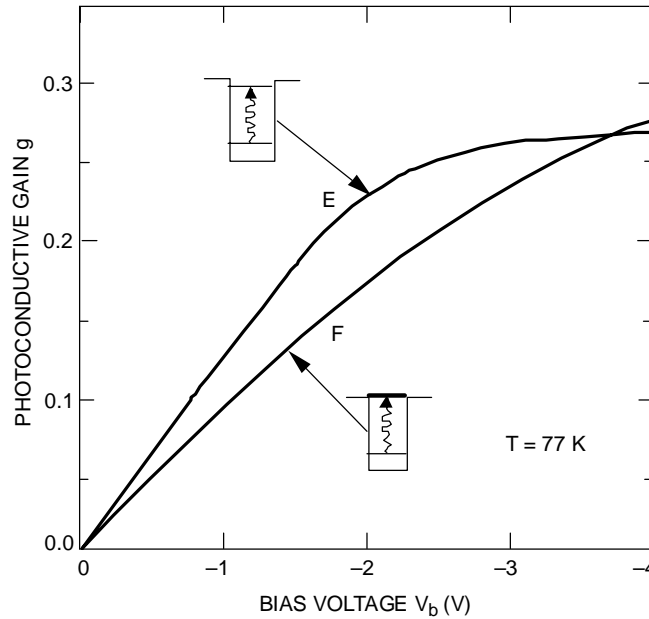


Fig. 19. Photoconductive gain g Vs bias voltage V_b (negative) for samples E and F at $T=77$ K. The inserts show the conduction band diagram. (Levine *et al.*, 1992a)

3.7 Detectivity

We can now determine the peak detectivity D_λ^* defined as (Levine *et al.*, 1990a; Zussman *et al.*, 1992)

$$D_\lambda^* = R_p^0 \frac{\sqrt{A\Delta f}}{i_n} \quad (19)$$

where A is the detector area and $\Delta f = 1$ Hz. This is done as a function of bias for a continuum (A), a bound (E), and a quasibound (F) QWIP in Fig. 21. (The dashed lines near the origin are extrapolations.) For all three samples D^* has a maximum value at a bias between $V_b = -2$ and -3 V. Since these QWIPs all have different cutoff wavelengths, these maximum D^* values cannot be simply compared. In order to facilitate this comparison, we note that the dark current has been demonstrated to follow an exponential law (Levine *et al.*, 1990a, 1992a; Zussman *et al.*, 1991) $I_d \propto e^{-(E_c - E_f)/kT}$ (where E_c is the cutoff energy $E_c = hc / \lambda_c$) over a wide range of both temperature and cutoff wavelength. Thus using $D^* \propto (R_p / i_n)$, we have

$$D^* = D_0^\lambda e^{E_c/2kT} \quad (20)$$

Fig. 20. Quantum efficiency η Vs bias voltage V_b (negative) for samples E and F. The zero bias quantum efficiencies η_0 and the maximum quantum efficiencies η_{\max} are shown. The inserts show the conduction band diagram. (Levine *et al.*, 1992a)

In order to compare the performance of these different QWIPs Levine *et al.* (1992b) have

plotted D^* against E_c on a log scale as shown in Fig. 22 (Levine *et al.*, 1990a, 1991b; Gunapala *et al.*, 1991a; Zussman *et al.*, 1991). The straight line fit the data very well which is satisfying considering the samples have different doping densities, N_d , different methods of crystal growth, different spectral widths $\cdot \lambda$, different excited states (bound, quasibound, and continuum) and even, in one case, a different materials system (InGaAs) (Gunapala *et al.*, 1991a). The best fit for $T = 77$ K detectivities of n-doped QWIPs is

$$D_e^* = 1.1 \times 10^6 e^{E_c/2kT} \text{ cm}\sqrt{\text{Hz}} / \text{W} \quad (21)$$

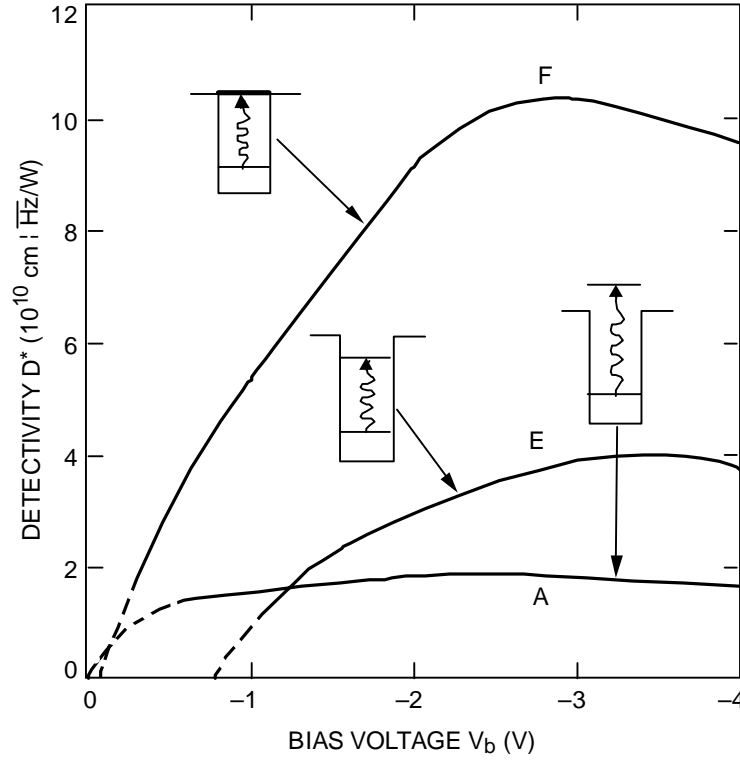


Fig. 21. Detectivity D^* (at $T=77$ K) Vs bias voltage V_b for samples A, E and F. The inserts show the conduction band diagram. (Levine *et al.*, 1992a)

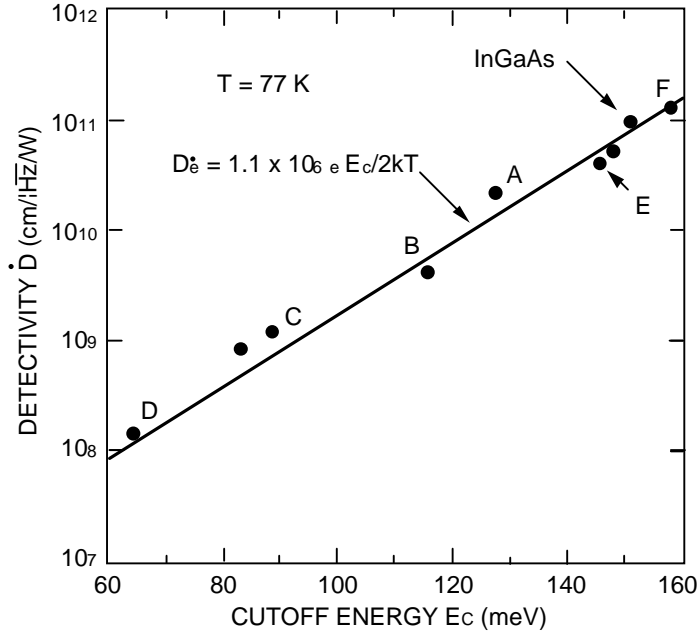


Fig. 22. Detectivity D^* (at $T=77$ K) Vs cutoff energy E_c for n-doped QWIPs. The straight line is the best fit to the measured data. (Levine *et al.*, 1992a)

Another useful figure of merit is blackbody responsivity and detectivity R_B and D_B^* and can be written as

$$D_B^* = R_B \frac{\sqrt{A\Delta f}}{i_n} \quad (22)$$

with

$$R_B = \frac{\int_{\lambda_1}^{\lambda_2} R(\lambda)W(\lambda)d\lambda}{\int_{\lambda_1}^{\lambda_2} W(\lambda)d\lambda} \quad (23)$$

It is worth noting that, for most applications, the blackbody responsivity R_B is reduced only a relatively small amount from the peak value R_p . Also note that, since QWIP dark current is mostly due to thermionic emission and thermionically assisted tunneling, unlike other detectors, QWIP detectivity increases nearly exponentially with the decreasing temperature as shown in Fig. 23.

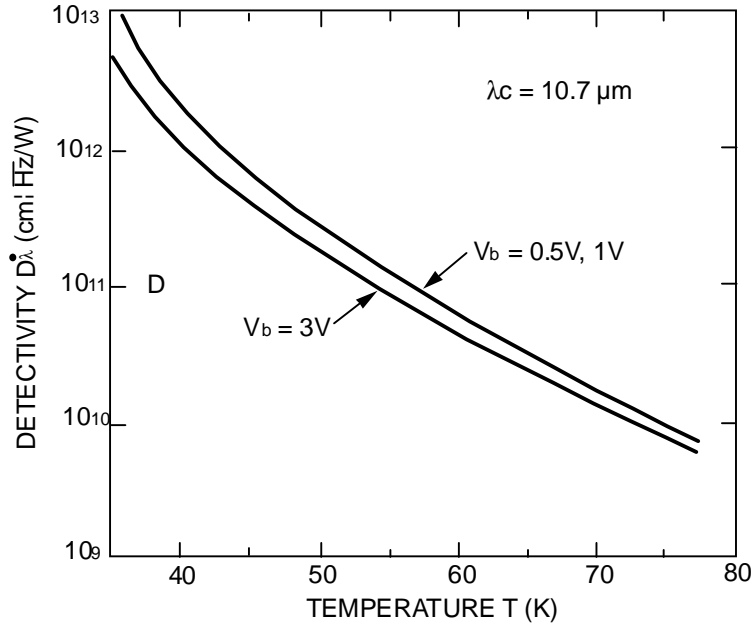


Fig. 23. Peak detectivity D_{λ}^* for a QWIP having cutoff wavelength of $\lambda_c=10.7 \mu\text{m}$ as a function of temperature T for several bias voltages V_b . (Gunapala *et al.*, 1990b)

4. LIGHT COUPLING

QWIPs do not absorb radiation incident normal to the surface since the light polarization must have an electric field component normal to the superlattice (i.e., growth direction) to be absorbed by the confined carriers (Levine, 1993, Gunapala and Bandara, 1995). When the incoming light contains no polarization component along the growth direction, the matrix element of the interaction vanishes [i.e., $\vec{\epsilon} \cdot \vec{p}_z = 0$ where $(\vec{\epsilon})$ is the polarization and (\vec{p}_z) is the momentum along growth direction (z)]. As a consequence, these detectors have to be illuminated through a 45° polished facet (Levine, 1993; Gunapala and Bandara, 1995). Clearly, this illumination scheme limits the configuration of detectors to linear arrays and single elements. For imaging, it is necessary to be able to couple light uniformly to two dimensional arrays of these detectors.

Several different monolithic grating structures, such as linear gratings (Goossen and Lyon, 1985; Hasnain *et al.*, 1989) two-dimensional (2-D) periodic gratings (Andersson *et al.*, 1991a, 1991b, 1991c; Sarusi *et al.*, 1994b; Bandara *et al.*, 1997), and random-reflectors (Sarusi *et al.*, 1991a, 1994a; Xing and Liu, 1996), have demonstrated efficient light coupling to QWIPs, and have made two dimensional QWIP imaging arrays feasible (see Fig. 24). These gratings deflect the incoming light away from the direction normal to the surface, enabling intersubband absorption. These gratings were made of metal on top of each detector or crystallographically etched through a cap layer on top of the MQW structure. Normal incident light-coupling efficiency comparable to the light coupling efficiency of a 45° polished facet illumination was demonstrated using linear gratings (Goossen and Lyon, 1985; Hasnain *et al.*, 1989).

4.1 Random Reflectors

Random reflectors have demonstrated excellent optical coupling for individual QWIPs as well as for large area FPAs (Sarusi *et al.*, 1994a; Xing and Liu, 1996, Gunapala *et al.*, 1997a, 1997b). It has been shown that many more passes of infrared light [Fig. 24(a)], and significantly higher absorption, can be achieved with a randomly roughened reflecting surface. By careful design of surface texture randomization (with a three level random reflector), an enhancement factor of 8 in responsivity compared to 45° illumination was demonstrated experimentally (Sarusi *et al.*, 1994a). The random structure on top of the detector prevents the light from being diffracted normally backward after the second bounce, as happens in the case of 2-D periodic grating [See Fig. 24(b)]. Naturally, thinning down the substrate enables more bounces of light and, therefore, higher responsivity (Sarusi *et al.*, 1994a, Gunapala *et al.*, 1997a).

All these gratings were fabricated on the detectors by using standard photolithography and selective dry etching. The advantage of the photolithographic process is its ability to accurately control the feature size and preserve the pixel-to-pixel uniformity, which is a prerequisite for high-sensitivity imaging FPAs. However, the resolution of photolithography and accuracy of etching processes become key issues in producing smaller grating feature sizes. These feature sizes are proportionally scaled with the peak response wavelength of the QWIP. The minimum feature size of random reflectors implemented in $15\ \mu\text{m}$ and $9\ \mu\text{m}$ cutoff FPAs were $1.25\ \mu\text{m}$ and $0.6\ \mu\text{m}$ respectively (Gunapala *et al.* 1997a, 1997b). Thus, random reflectors of the $9\ \mu\text{m}$ cutoff FPA were less sharp and had fewer scattering centers compared to random reflectors of the $15\ \mu\text{m}$ cutoff FPA. These less sharp features in random gratings lowered the light coupling efficiency than expected. Therefore, it could be advantageous to utilize a 2-D periodic grating for light coupling in shorter wavelength QWIPs. However, one can avoid this problem by designing a random reflector which has features similar to 2-D periodic gratings (Xing and Liu, 1996).

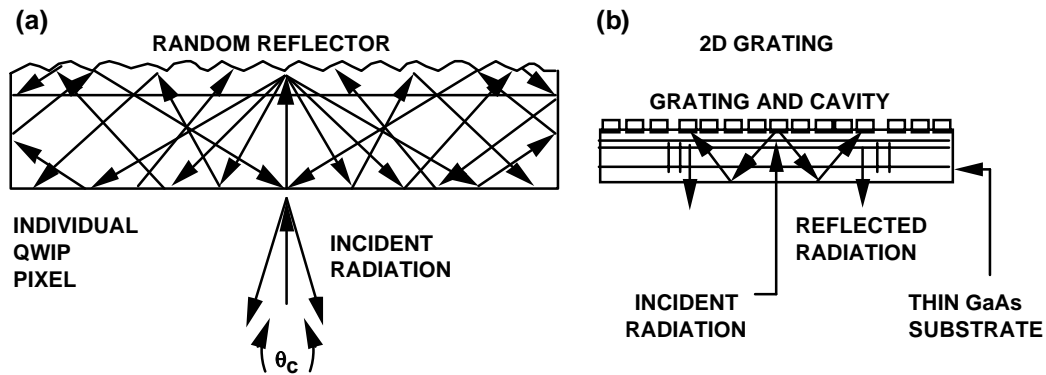


Fig. 24 (a). Schematic side view of a thin QWIP pixel with a random grating reflector. Ideally all the radiation is trapped except for a small fraction which escapes through the escape cone. (b) Schematic diagram of 2-D periodic grating specifications. The grating features are spaced periodically along the x and y directions.

4.2 Two-Dimensional Periodic Gratings

Detailed theoretical analysis has been carried out on both linear and 2-D periodic gratings on QWIPs. In 2-D gratings, the periodicity of the grating repeats in two perpendicular directions on the detector plane, leading to the absorption of both polarizations of incident infrared radiation. Also, experiments have been carried out for 2-D grating coupled QWIP detectors designed for wavelengths $\lambda \sim 9 \mu\text{m}$ (Andersson *et al.*, 1991a, 1991b, 1991c; Bandara *et al.*, 1997) and $\lambda \sim 16 - 17 \mu\text{m}$ (Sarusi *et al.*, 1994b). A factor of 2-3 responsivity enhancement relative to the standard 45° polished facet illumination was observed for large area mesas ($500 \mu\text{m} \times 500 \mu\text{m}$) with a total internal reflection optical cavity which can be created with an additional Al GaAs layer (Andersson *et al.*, 1991a, 1991b, 1991c) or with a thinned substrate (Sarusi *et al.*, 1994b). This optical cavity is responsible for an extra enhancement factor of about 2 due to the total internal reflection from the AlGaAs layer or from the thinned substrate as shown in Fig. 24. Due to the resonance nature, the light coupling efficiency of 2-D gratings depends strongly on the wavelength and, thus, exhibits narrow band width spectral responses. The normalized responsivity spectrum for 2-D periodic grating coupled QWIP samples (with six different grating periods, D and a fixed groove depth) and for the standard 45° sample are shown in Fig. 25. Note the normalized spectral peak shifts from $7.5 \mu\text{m}$ to $8.8 \mu\text{m}$ as the grating period increases from $D = 2.2 \mu\text{m}$ to $3.2 \mu\text{m}$. These measurements were repeated for three groove depths. The grating peak wavelength λ_{gp} (where the grating enhancement is maximized) and the peak enhancement (enhancement at λ_{gp}) associated with each grating period was obtained by normalizing the absolute spectral responsivity of the grating detectors relative to the 45° detector sample. As expected from the theory, measured λ_{gp}

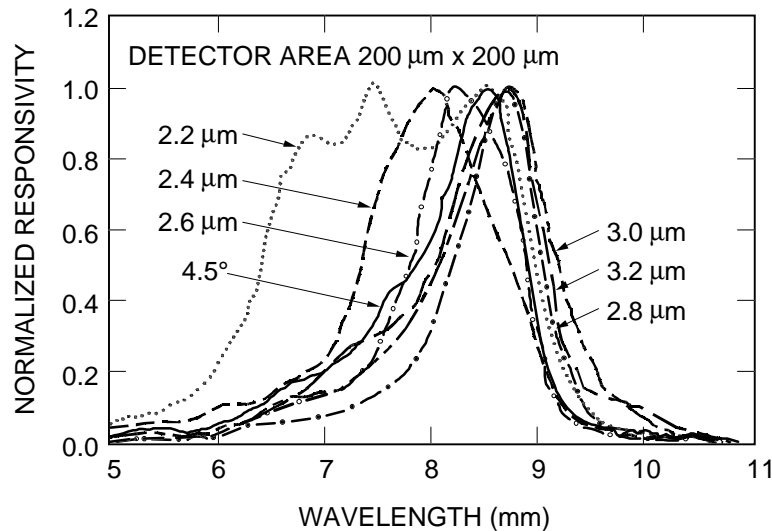


Fig. 25. Measured normalized responsivity spectra as a function of grating period D vary from 2.2 - 3.2 μm . The solid curve represent responsivity spectra same QWIP with 45° polished edge. (Bandara *et al.*, 1997)

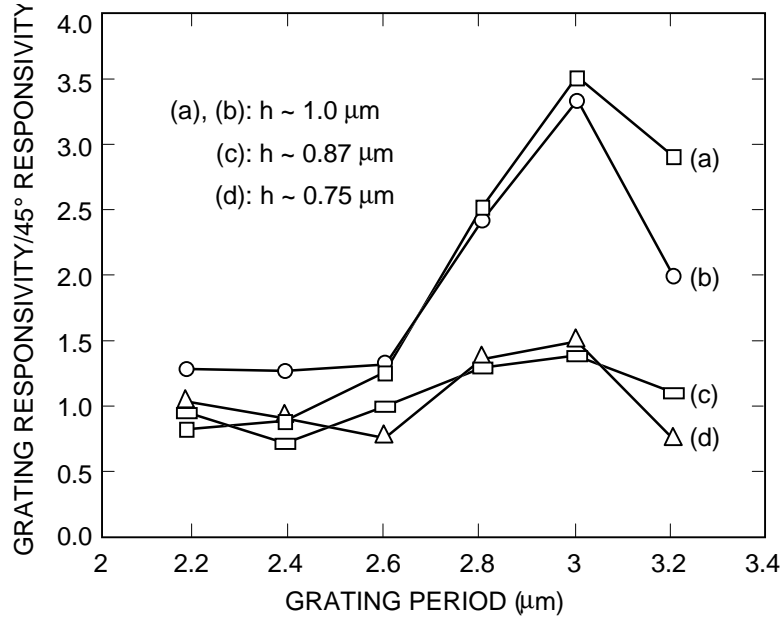


Fig. 26. The experimental responsivity enhancement at λ_{gp} for each grating period with different groove depths. Curves a and b represent gratings with same groove depth but different in detector area (a - $200 \times 200 \mu m^2$ and b - $400 \times 400 \mu m^2$). Curve c and d represent $200 \times 200 \mu m^2$ area detectors with different groove depths. (Bandara *et al.*, 1997)

linearly depends on grating period and it is independent of the groove depth of the grating (Bandara *et al.*, 1997). Figure 26 shows experimental responsivity enhancement due to 2-D grating at λ_{gp} for each grating period with different groove depths. One sample shows enhancement up to a factor of 3.5 (curves a and b in Fig. 26) depending on the grating period, while the other two samples show no enhancement and no dependence on the grating period. This high enhancement factor was measured in a similar (same gratings and groove depth) sample with different detector area. Scanning Electron Microscopic (SEM) pictures of two samples, associated with curve c and d of Fig. 26, show apparent distortion in the features of the gratings (Bandara *et al.*, 1997). This can be attributed to the partial contact between the grating mask and the wafer during the photolithography.

4.3 Corrugated Structure

Recently, Chen *et al.* (1997) has demonstrated a new light coupling geometry for QWIPs based on total internal reflection at the corrugated surface created within a detector pixel (Choi *et al.*, 1998a and 1998b). In these structures, linear V-grooves are chemically etched through the active detector region down to the bottom contact layer to create a collection of angled facets within a single detector pixels as shown in Fig. 27 (a). These facets deflect normally incident light into the remaining QWIP active area through total internal reflection. For certain chemical solutions, such as $1H_2SO_4 : 8H_2O_2 : 10H_2O$, the etching rate is different for different crystallographic planes. As a result, triangular wires are created with sidewalls inclined around 54° with (100) surface along (0, 1, 1) the plane. In practice, the angle was found to be at 50° (Choi *et al.*, 1998a, 1998b). See Fig. 27(b).

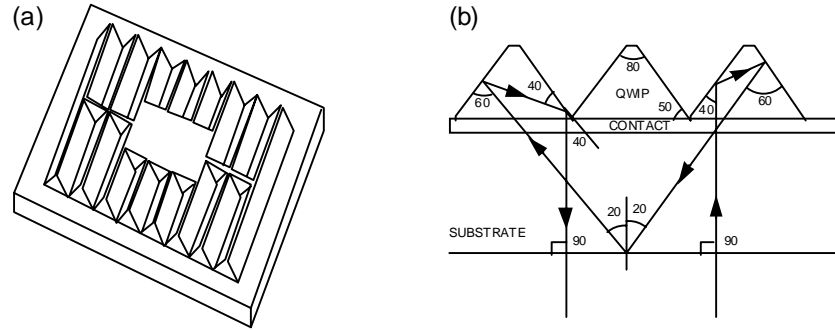


Fig. 27(a). The 3-dimensional perspective of a corrugated QWIP detector pixel and (b) the ray diagram at the side view. (Choi *et al.*, 1998b)

Since the corrugated QWIP structure exposes the active layers of the detector, top metal contact cannot be deposited directly on the detector pixel. Two different approaches have been considered addressing this problem; (i) to leave out an unetched area for the contact as illustrated in Fig.27 (a), and (ii) isolate the active layers with a dielectric such as polyimide. One of the main advantage of this light coupling technique is reduction in pixel dark current due the smaller QWIP active area. In addition, the coupling scheme does not show significant wavelength and size dependence, and is therefore suitable for multi-color or broad-band QWIPs. Figure 28 shows the spectral responsivity of the corrugated QWIP under normal incident illumination from the back of the wafer. For comparison, spectral responsivity of the same QWIP with 45° edge coupling is also illustrated in the Fig. 28. It clearly shows that the corrugated structure does not change the intrinsic absorption line shape which is represented by the 45° edge-coupling response, but increases the magnitude by a factor of 1.5. Also, this structure shows about 2.6 factor lower dark current due to the less active material, resulting in about 2.4 times improved D^* (Choi *et al.*, 1998a, 1998b).

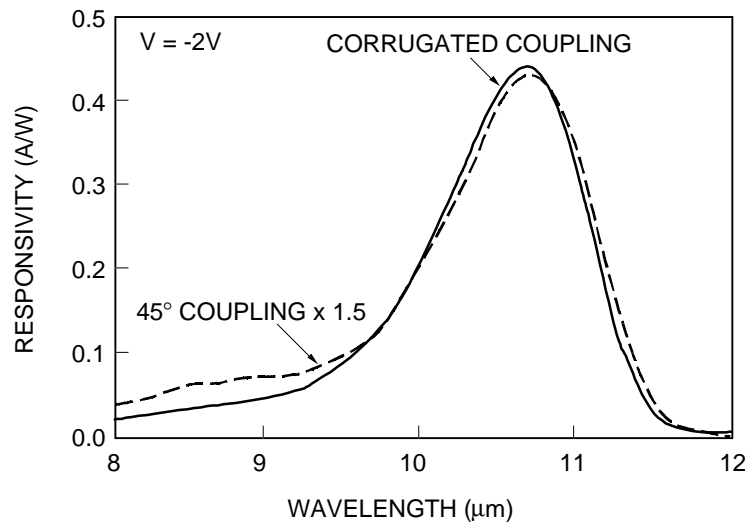


Fig. 28. Spectral responsivity of the corrugated QWIP and the same QWIP using 45° edge coupling. (Choi *et al.*, 1998b)

4.4 Microlenses

The general concept of utilizing microlenses with QWIPs is to increase the signal output or decrease the dark current or both per detecting pixel. Use of a microlens to concentrate the photon flux will lead to a much smaller detector area requirement. Since the dark current is linearly related to the detector area, the dark current is decreased. Thus, the goal of increasing the D^* is achieved. The reduction of dark current can be expressed as the ratio of the area gain, G_A (Pool *et al.*, 1998). If d is the diameter of the focal spot and D is the pixel diameter, then $G_A = (D/d)^2 = [Dn_r f/F]^2$, where n_r is the index of refraction, f is the f number of the optical system and F is the focal length of the microlens. For example, if we let $D = 2.44 \lambda f$, which is the diameter of an Airy disk, then at $15 \mu\text{m}$, $D \bullet 73 \mu\text{m}$. If we select $F=125 \mu\text{m}$, then $d \bullet 20 \mu\text{m}$. The dark current will improve by a factor of 13. If $F=75 \mu\text{m}$ then $d \bullet 12 \mu\text{m}$, the dark current will improve by a factor of 37.

Recently, monolithically integrated microlens and QWIP was demonstrated by Pool *et al.* (1998). Four-level binary optic microlenses were fabricated by standard contact lithography, using a two-mask photoresist pattern for plasma etching. The two-etch step process for fabrication of the four-level diffractive optics lenses created phase steps $d = \lambda/[2^2(n_r-1)]$, where n_r is the index of refraction of GaAs and λ is the wavelength of the incident light for which the lens is optimized. Since these lenses were designed for incident light of $15 \mu\text{m}$ the smallest feature size (outer zones) was approximately $4 \mu\text{m}$, making lithography relatively straightforward. Fabrication errors which resulted were level misalignment, etch depth errors, and limited resolution of outer zone features. The lenses were first fabricated and the QWIPs subsequently fabricated and aligned to the lenses through use of an infrared backside aligner to within $1 \mu\text{m}$ accuracy. The theoretical efficiency of a four-level diffractive optic lens in the scalar approximation is 81%. In this study microlenses were fabricated from $150 \times 150 \mu\text{m}^2$ to $350 \times 350 \mu\text{m}^2$ for infrared radiation to be focused on $75 \times 75 \mu\text{m}^2$ QWIP detectors, optimized for a peak wavelength of $15 \mu\text{m}$. In addition to the four-level lenses, continuous-relief lenses were fabricated by direct-write electron beam lithography followed by transfer etching technique (Pool *et al.*, 1998). The process for fabrication of the continuous relief lens is given by the schematic representation in Fig. 29. Figure 30 shows the surface of a $250 \mu\text{m}$ lens.

Although the effect of the microlens is evident through an increase in responsivity of approximately 2.7, the efficiency is far lower than a simple analysis would predict. The experiment was repeated with the continuous relief microlenses and the results were similar, even though the efficiency of the continuous lenses was likely higher than the 4-level lenses. The poor performance of the microlens-QWIP combination can be understood by analyzing the diffraction characteristics of the grating. The lens produces a cone of converging waves that are incident on the grating. Because the grating was optimized for normal incidence, the coupling of the angled waves into the desired polarization for QWIP absorption was severely degraded. There are two factors that influence the optical coupling: (i) the angles of the diffracted waves (grating orders), and (ii) the efficiencies of the diffracted orders. The angles of the diffracted orders θ_m can be

found directly from the grating equation,

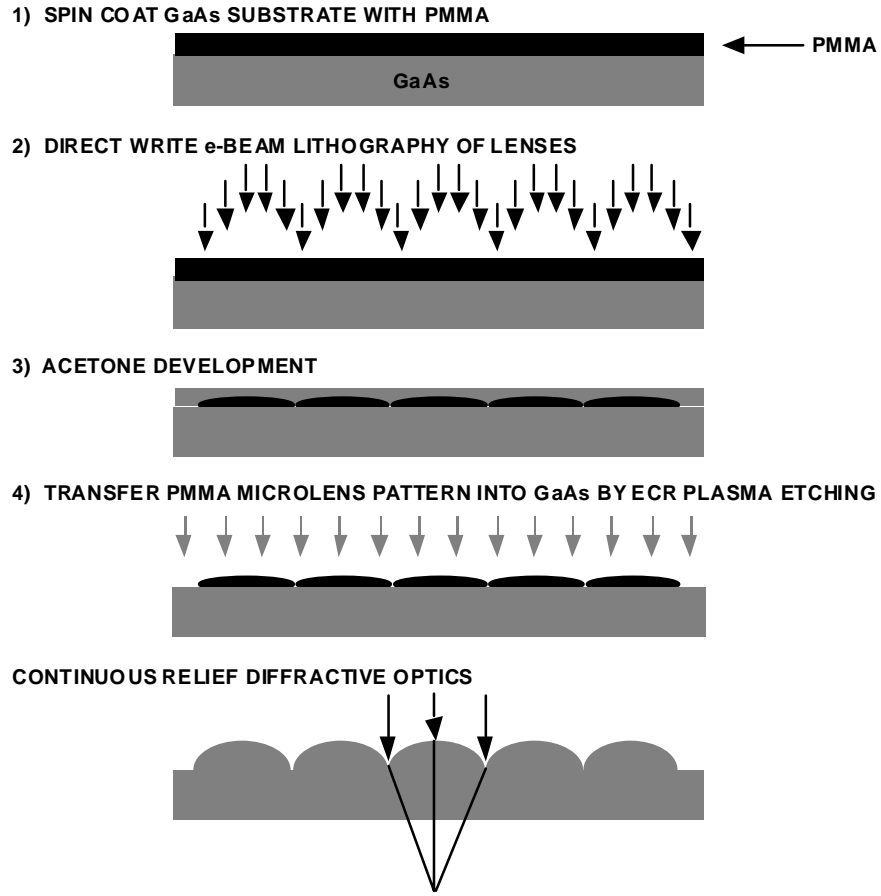


Fig. 29. Schematic representation of the fabrication process for continuous relief microlenses. (Pool *et al.*, 1998)

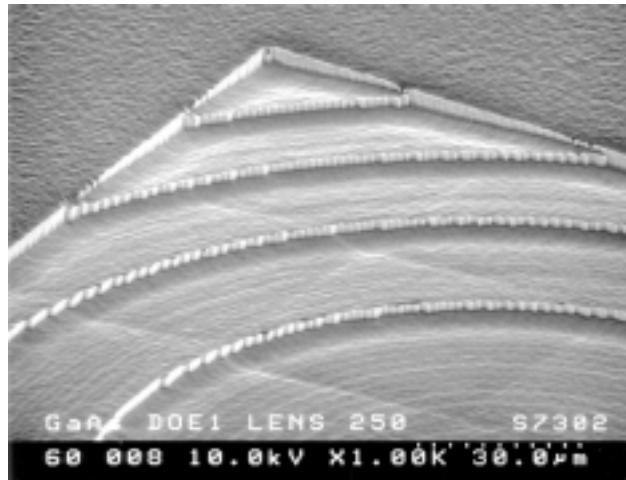


Fig. 30. AFM image of a 250 μm microlens in PMMA. (Pool *et al.*, 1998)

$$\sin(\theta_m) = m \frac{\lambda_{\text{GaAs}}}{\Lambda} - \sin(\theta_{\text{inc}}), \quad m = 0, \pm 1, \pm 2, \dots \quad (24)$$

where θ_{inc} is angle of incidence, λ_{GaAs} is the wavelength inside the GaAs ($\lambda/3.1$), and $\Lambda = 4.85 \mu\text{m}$ is the grating period.

The efficiencies of the diffracted orders must be found using a rigorous electromagnetic analysis technique. In this study, rigorous coupled-wave analysis was used to determine the efficiency of the grating as a function of incident angle and wavelength. After the angles and efficiencies of the diffracted orders were found, the fields inside the quantum well stack were calculated (Pool *et al.*, 1998). Because the QWIP can only absorb the component of the field perpendicular to the quantum well layers E_{\perp} , the integral of $|E_{\perp}|^2$ inside the quantum well region was taken as a measure of QWIP coupling efficiency. At $15 \mu\text{m}$, the coupling is strongly peaked around normal incidence even though the diffraction efficiencies are not well optimized. At a shorter wavelength of $14.5 \mu\text{m}$, the period to wavelength ratio is larger, allowing both the $+1$ and -1 orders to continue to propagate up to a few degrees off-normal. This broadens the angular response, but because the angles of the diffracted orders are smaller, they do not couple as effectively into the QWIP and the peak response is reduced.

The focused field from the lens is actually not a plane wave, but it can be Fourier decomposed into an angular spectrum of plane waves. For a given lens, there is certainly an optimum grating period that maximizes the integrated product of the focused-field angular spectrum and the grating angular response. However, it is unlikely that a lens-grating combination will achieve the same responsivity as a grating optimized for normally incident plane-wave illumination. Furthermore, for the lens-grating combination to effectively produce a higher signal-to-noise ratio, the area of the QWIP mesa must be reduced. In this situation, there may be too few grating periods for efficient diffraction. Although the microlens concept is not well suited for a QWIP detector, the concept described here can be soundly applied to normal incident absorbing infrared detectors (Pool *et al.*, 1998).

5. IMAGING FOCAL PLANE ARRAYS

There are many ground based and space borne applications that require long-wavelength, large, uniform, reproducible, low cost, low 1/f noise, low power dissipation, and radiation hard infrared FPAs. For example, the absorption lines of many gas molecules, such as ozone, water, carbon monoxide, carbon dioxide, and nitrous oxide occur in the wavelength region from 3 to $18 \mu\text{m}$. Thus, infrared imaging systems that operate in the LWIR and VLWIR region are required in many space applications such as monitoring the global atmospheric temperature profiles, relative humidity profiles, cloud characteristics, and the distribution of minor constituents in the atmosphere which are being planned for NASA's Earth Observing System (Chahine, 1990). In addition, $8\text{-}15 \mu\text{m}$ FPAs would be very useful in detecting cold objects such as ballistic missiles in midcourse [when hot rocket engine is not burning most of the emission peaks in the $8\text{-}15 \mu\text{m}$ infrared region (Duston, 1995)]. The GaAs/ $\text{Al}_x\text{Ga}_{1-x}\text{As}$ material system allows the quantum well shape to be tweaked over a range wide enough to enable light detection at wavelengths longer than

$\sim 6 \mu\text{m}$. Thus, GaAs based QWIP is a potential candidate for such space borne and ground based applications and many research groups (Bethea *et al.*, 1991, 1992, 1993; Kozlowski *et al.*, 1991a, Faska *et al.*, 1992; Beck *et al.*, 1994; Gunapala *et al.*, 1997a, 1997b, 1998a; Andersson *et al.*, 1997; Choi *et al.*, 1998a; Breiter *et al.*, 1998) have already demonstrated large uniform FPAs of QWIPs tuned to detect light at wavelengths from 6 to 25 μm in the GaAs/Al_xGa_{1-x}As material system.

5.1 Effect of nonuniformity

The general figure of merit that describes the performance of a large imaging array is the noise equivalent temperature difference NE \bullet T. NE \bullet T is the minimum temperature difference across the target that would produce a signal-to-noise ratio of unity and it is given by (Kingston, 1978; Zussman *et al.*, 1991)

$$\text{NE}\Delta T = \frac{\sqrt{A\Delta f}}{D_B^* (dP_B / dT)}, \quad (25)$$

where D_B^* is the blackbody detectivity (defined by Eq. 22) and (dP_B / dT) is the change in the incident integrated blackbody power in the spectral range of detector with temperature. The integrated blackbody power P_B , in the spectral range from λ_1 to λ_2 , can be written as

$$P_B = A \sin^2\left(\frac{\theta}{2}\right) \cos\phi \int_{\lambda_1}^{\lambda_2} W(\lambda) d\lambda, \quad (26)$$

where θ , ϕ , and $W(\lambda)$ are the optical field of view, angle of incidence, and blackbody spectral density respectively, and are defined by Eqs. 7 and 8 in sub-section 3.3. Before discussing the array results, it is also important to understand the limitations on the FPA imaging performance due to pixel nonuniformities (Levine, 1993). This point has been discussed in detail by Shepherd (1988) for the case of PtSi infrared FPAs (Mooney *et al.*, 1989) which have low response, but very high uniformity. The general figure of merit to describe the performance of a large imaging array is the noise equivalent temperature difference NE \bullet T, including the spatial noise which has been derived by Shepherd (1988), and given by

$$\text{NE}\Delta T = \frac{N_n}{dN_b / dT_b}, \quad (27)$$

where T_b is the background temperature, and N_n is the total number of noise electrons per pixel, given by

$$N_n^2 = N_t^2 + N_b^2 + u^2 N_b^2. \quad (28)$$

The photoresponse independent temporal noise electrons is N_t , the shot noise electrons from the background radiation is N_b , and residual nonuniformity after correction by the electronics is u . The temperature derivative of the background flux can be written to a good approximation as

$$\frac{dN_b}{dT_b} = \frac{hcN_b}{k\bar{\lambda}T_b^2}, \quad (29)$$

where $\bar{\lambda} = (\lambda_1 + \lambda_2)/2$ is the average wavelength of the spectral band between λ_1 and λ_2 . When temporal noise dominates, $NE \cdot T$ reduces to Eq. (25). In the case where residual nonuniformity dominates, Eqs. (27) and (29) reduces to

$$NE\Delta T = \frac{u\bar{\lambda}T_b^2}{1.44}. \quad (30)$$

The units of the constant is cm K, $\bar{\lambda}$ is in cm and T_b is in K. Thus, in this spatial noise limited operation $NE \cdot T \propto u$ and higher uniformity means higher imaging performance. Levine (1993) has shown as an example, taking $T_b = 300$ K, $\bar{\lambda} = 10 \mu\text{m}$, and $u = 0.1\%$ leads to $NE \cdot T = 63$ mK, while an order of magnitude uniformity improvement (i.e., $u = 0.01\%$) gives $NE \cdot T = 6.3$ mK. By using the full expression Eq. (28) Levine (1993) has calculated $NE \cdot T$ as a function of D^* as shown in Fig. 31. It is important to note that when $D^* \geq 10^{10}$ cm \cdot Hz/W, the performance is uniformity limited and thus essentially independent of the detectivity, i.e., D^* is not the relevant figure of merit (Grave and Yariv, 1992).

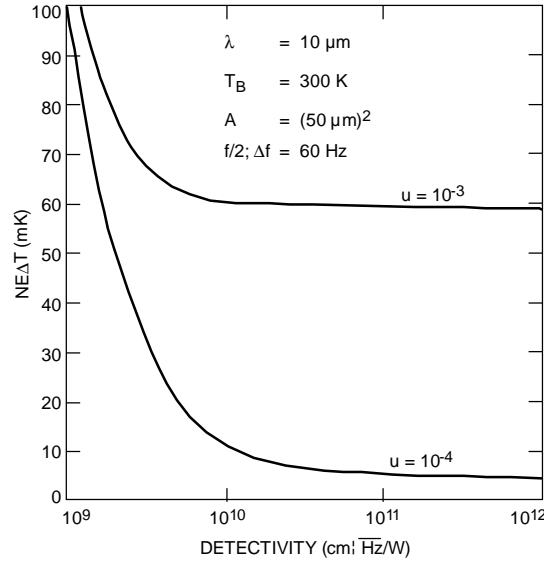


Fig. 31. Noise equivalent temperature difference $NE \cdot T$ as a function of detectivity D^* . The effects of nonuniformity are included for $u = 10^{-3}$ and 10^{-4} . Note that for $D^* > 10^{10}$ cm \cdot Hz/W detectivity is not the relevant figure of merit for FPAs. (Levine, 1993)

5.2 128x128 VLWIR Imaging Camera

By carefully designing the quantum well structure as well as the light coupling (as discussed in Section 4) to the detector, it is possible to optimize the material to an optical response in the desired spectral range, determine the spectral response shape, as well as reduce the parasitic dark current, and therefore increase the detector impedance.

Generally, in order to tailor the QWIP spectral response to the VLWIR spectral region the barrier height should be lowered and the well width increased relative to the shorter cutoff wavelength QWIPs. For a detailed analysis of design and performance optimization of VLWIR QWIPs see Sarusi; *et al.* (1994c).

The first VLWIR FPA camera was demonstrated by Gunapala *et al.* (1997a) which consisted of bound-to-quasibound QWIPs as shown in Fig. 32. Samples were grown using MBE and their well widths L_w vary from 65 to 75 Å, while barrier widths are approximately constant at $L_b = 600$ Å. These QWIPs consisted of 50 periods of doped ($N_D = 2 \times 10^{17} \text{ cm}^{-3}$) GaAs quantum wells, and undoped $\text{Al}_x\text{Ga}_{1-x}\text{As}$ barriers. Very low doping densities were used to minimize the parasitic dark current. The Al molar fraction in the $\text{Al}_x\text{Ga}_{1-x}\text{As}$ barriers varies from $X = 0.15$ to 0.17 (corresponding to cutoff wavelengths of 14.9 to 15.7 μm). These QWIPs had peak wavelengths from 14 to 15.2 μm as shown in Fig. 33. The peak quantum efficiency was 3% (lower quantum efficiency is due to the lower well doping density) for a 45° double pass.

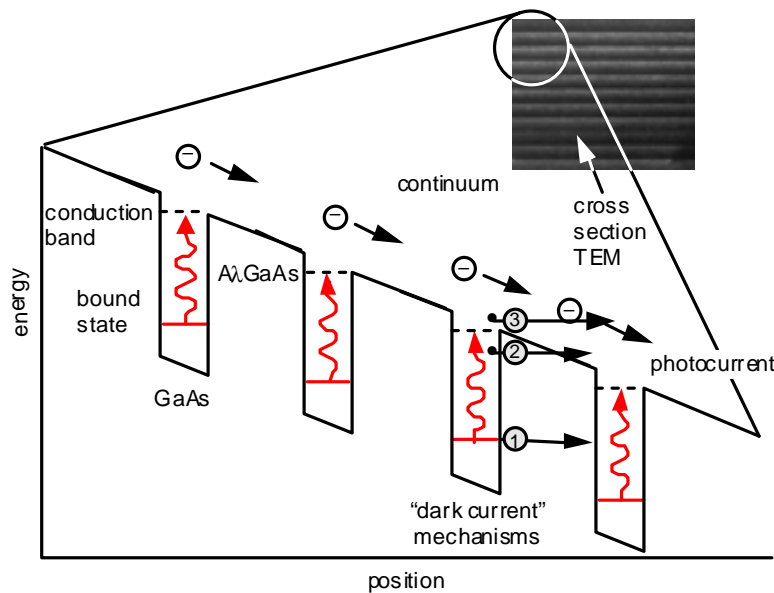


Fig. 32. Schematic diagram of the conduction band in a bound-to-quasibound QWIP in an externally applied electric field. Absorption of infrared photons can photoexcite electrons from the ground state of the quantum well into the continuum, causing a photocurrent. Three dark current mechanisms are also shown: ground state tunneling (1); thermally assisted tunneling (2); and thermionic emission (3). The inset shows a cross-section transmission electron micrograph of a QWIP sample. (Gunapala *et al.*, 1997b)

Four device structures were grown on 3 inch GaAs wafers and each wafer processed into 35 128x128 FPAs. An expanded corner of a FPA is shown in Fig. 34. The pixel pitch of the FPA is $50\text{ }\mu\text{m}$ and the actual pixel size is $38\times 38\text{ }\mu\text{m}^2$. Two level random reflectors

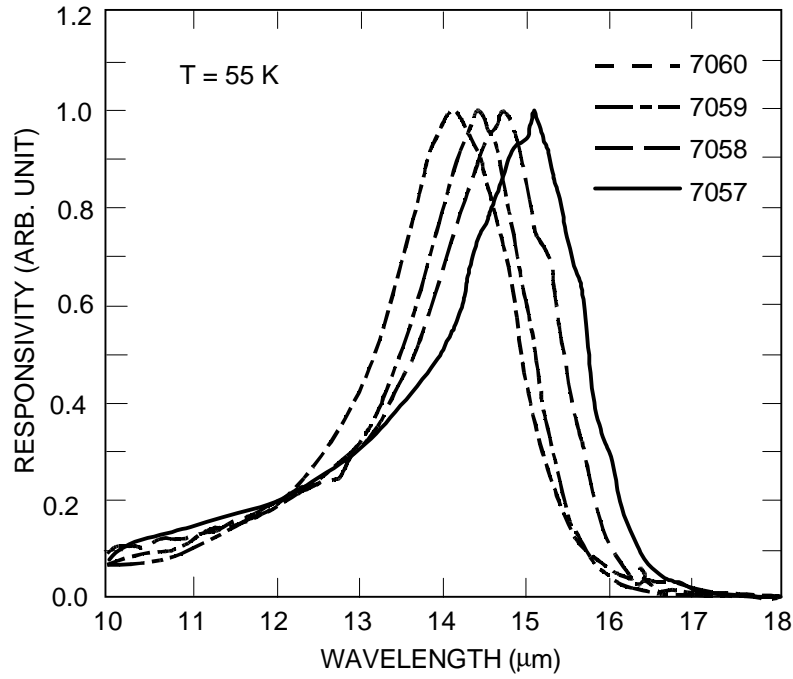


Fig. 33. Normalized responsivity spectra of four bound-to-quasibound VLWIR QWIP FPA samples at temperature $T = 55\text{ K}$. (Gunapala *et al.*, 1997a)

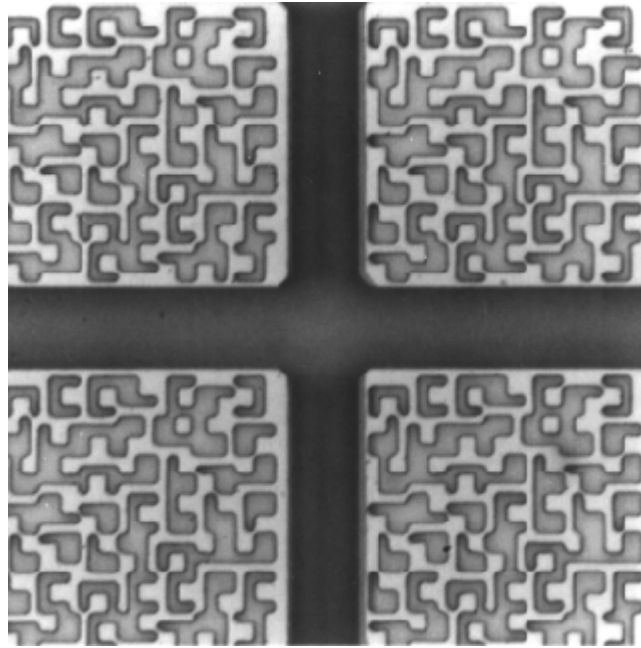


Fig. 34. An expanded corner of a 128x128 QWIP FPA showing two level random reflectors on pixels ($38\times 38\text{ }\mu\text{m}^2$). (Gunapala *et al.*, 1997a)

used to improve the light coupling, can be seen on top of each pixel. These random reflectors, which were etched to a depth of half a peak wavelength in GaAs using reactive-ion etching, had a square profile. These reflectors are covered with Au/Ge and Au (for Ohmic contact and reflection), and In bumps are evaporated on top for Silicon multiplexer hybridization. A single QWIP FPA was chosen from sample number 7060 (cutoff wavelength of this sample is $14.9\ \mu\text{m}$) and bonded to a silicon readout multiplexer. FPA was back-illuminated through the flat thinned substrate. This initial array gave excellent images with 99.9% of the pixels working, demonstrating the high yield of GaAs technology. As mentioned earlier this high yield is due to the excellent GaAs growth uniformity and the mature GaAs processing technology. The uniformity after two point correction was $u = 0.03\%$ (Gunapala *et al.*, 1997a).

Video images were taken at various frame rates varying from 20 to 200 Hz with f/2.6 KRS-5 optics at temperatures high as $T = 45\ \text{K}$, using a multiplexer having a charge capacity of 4×10^7 electrons. However, the total charge capacity was not available during the operation, since the charge storage capacitor was partly filled to provide the high operating bias voltage required by the detectors (i.e., $V_b = -3\ \text{V}$). Figure 35 shows an image of a man's face with NE• $T = 30\ \text{mK}$ (Gunapala *et al.*, 1997a). It should be noted that these initial unoptimized FPA results are far from optimum.

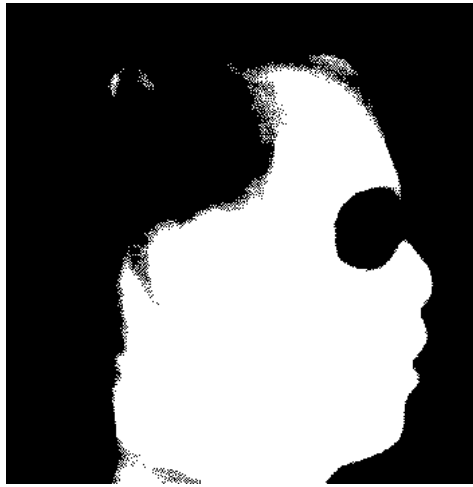


Fig. 35. One frame from a $15\text{-}\mu\text{m}$ QWIP video image of a man's face with NE• $T = 30\ \text{mK}$. (Gunapala *et al.*, 1997a)

5.3 256x256 LWIR Imaging Camera

Infrared imaging systems that work in the $8\text{-}12\ \mu\text{m}$ (LWIR) band have many applications, including night vision, navigation, flight control, early warning systems, etc. Several research groups have demonstrated (Betha *et al.*, 1991, 1992, 1993; Kozlowski *et al.*, 1991a, 1991b; Levine *et al.*, 1991d; Asom *et al.*, 1991; Swaminathan *et al.*, 1992) the excellent performance of QWIP arrays. For example, Faska *et al.* (1992) have obtained very good images using a 256×256 bound-to-miniband MQW FPA. The first 256×256 LWIR hand-held imaging camera was demonstrated by Gunapala *et al.* (1997b). The

device structure of this FPA consisted of a bound-to-quasibound QWIP containing 50 periods of a 45 Å well of GaAs (doped $n = 4 \times 10^{17} \text{ cm}^{-3}$) and a 500 Å barrier of $\text{Al}_{0.3}\text{Ga}_{0.7}\text{As}$. Ground state electrons are provided in the detector by doping the GaAs well layers with Si. This photosensitive MQW structure is sandwiched between 0.5 μm GaAs top and bottom contact layers doped $n = 5 \times 10^{17} \text{ cm}^{-3}$, grown on a semi-insulating GaAs substrate by MBE. Then a 0.7 μm thick GaAs cap layer on top of a 300 Å $\text{Al}_{0.3}\text{Ga}_{0.7}\text{As}$ stop-etch layer was grown in situ on top of the device structure to fabricate the light coupling optical cavity.

The detectors were back illuminated through a 45° polished facet as described earlier and a responsivity spectrum is shown in Fig. 36. The responsivity of the detector peaks at 8.5 μm and the peak responsivity (R_p) of the detector is 300 mA/W at bias $V_B = -3 \text{ V}$. The spectral width and the cutoff wavelength are $\lambda/\lambda_c = 10\%$ and $\lambda_c = 8.9 \text{ μm}$ respectively. The measured absolute peak responsivity of the detector is small, up to about $V_B = -0.5 \text{ V}$. Beyond that it increases nearly linearly with bias reaching $R_p = 380 \text{ mA/W}$ at $V_B = -5 \text{ V}$. This type of behavior of responsivity versus bias is typical for a bound-to-quasibound QWIP. The peak quantum efficiency was 6.9% at bias $V_B = -1 \text{ V}$ for a 45° double pass. The lower quantum efficiency is due to the lower well doping density ($5 \times 10^{17} \text{ cm}^{-3}$) as it is necessary to suppress the dark current at the highest possible operating temperature.

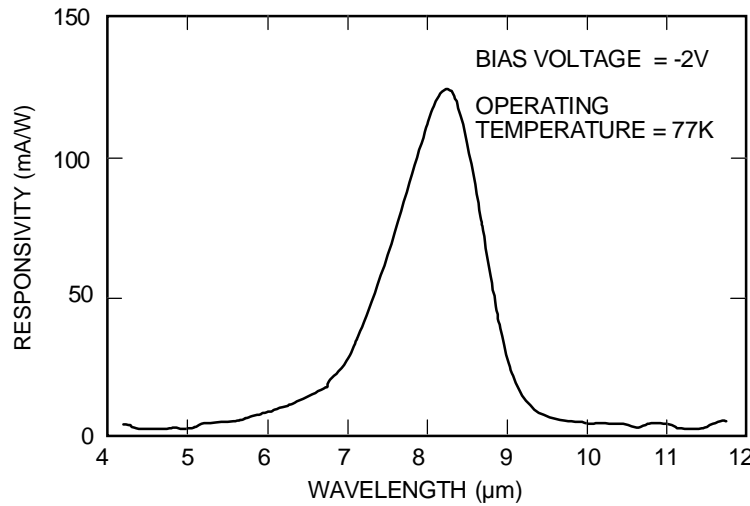


Fig. 36. Responsivity spectrum of a bound-to-quasibound LWIR QWIP test structure at temperature $T = 77 \text{ K}$. The spectral response peak is at 8.5 μm and the long wavelength cutoff is at 8.9 μm. (Gunapala *et al.*, 1997a)

After the random reflector array was defined by the lithography and dry etching, the photoconductive QWIPs of the 256x256 FPAs were fabricated by wet chemical etching through the photosensitive GaAs/ $\text{Al}_x\text{Ga}_{1-x}\text{As}$ MQW layers into the 0.5 μm thick doped GaAs bottom contact layer. The pitch of the FPA is 38 μm and the actual pixel size is $28 \times 28 \text{ μm}^2$. The random reflectors on top of the detectors were then covered with Au/Ge and Au for Ohmic contact and reflection. A single QWIP FPA was chosen and hybridized (via indium bump-bonding process) to a 256x256 CMOS readout multiplexer (Amber AE-

166) and biased at $V_B = -1.0$ V. The FPA was back-illuminated through the flat thinned substrate membrane (thickness ≈ 1300 Å). This array gave excellent images with 99.98% of the pixels working (number of dead pixels ≈ 10), demonstrating the high yield of GaAs technology (Gunapala *et al.*, 1997b). The measured $NE \cdot T$ (mean value) of the FPA at an operating temperature of $T = 70$ K, bias $V_B = -1$ V, and 300 K background is 15 mK. This agrees reasonably with our estimated value of 8 mK based on test structure data. The peak quantum efficiency of the FPA was 3.3% (lower FPA quantum efficiency is attributed to 54% fill factor and 90% charge injection efficiency) and this corresponds to an average of three passes of infrared radiation (equivalent to a single 45° pass) through the photosensitive MQW region.

A 256x256 QWIP FPA hybrid was mounted onto a 250 mW integral Sterling closed-cycle cooler assembly and installed into an Amber RADIANCE 1™ camera-body to demonstrate a hand-held LWIR camera (shown in Fig. 37). The camera is equipped with a 32-bit floating-point digital signal processor combined with multi-tasking software, providing the speed and power to execute complex image-processing and analysis functions inside the camera body itself. The other element of the camera is a 100 mm focal length germanium lens, with a 5.5 degree field of view. It is designed to be transparent in the 8-12 μm wavelength range to be compatible with the QWIP's 8.5 μm operation. The digital acquisition resolution of the camera is 12-bits, which determines the instantaneous dynamic range of the camera (i.e., 4096). However, the dynamic range of QWIP is 85 Decibels. Its nominal power consumption is less than 50 Watts.

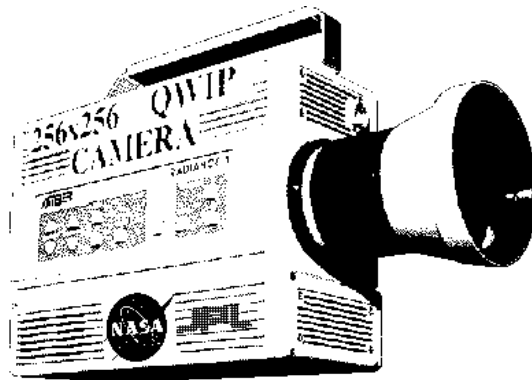


Fig. 37. Picture of the first 256x256 hand-held long wavelength QWIP camera (QWIP RADIANCE™). (Gunapala *et al.*, 1997a)

5.4 640X486 LWIR Imaging Camera

In this section, we will discuss the demonstration of the 640x486 LWIR imaging camera by Gunapala *et al.* (1998a). Although random reflectors have achieved relatively high quantum efficiencies with large area test device structures, it is not possible to achieve the similar high quantum efficiencies with random reflectors on small area FPA pixels due to the reduced width-to-height aspect ratios. In addition, due to fabrication difficulties of random reflector for shorter wavelength FPAs as described in subsection 4.1, a 2-D periodic grating reflector was fabricated for light coupling of this 640x486 QWIP FPA.

After the 2-D grating array was defined by the photolithography and dry etching, the photoconductive QWIPs of the 640x486 FPAs were fabricated by wet chemical etching through the photosensitive GaAs/Al_xGa_{1-x}As MQW layers into the 0.5 μm thick doped GaAs bottom contact layer. The pitch of the FPA is 25 μm and the actual pixel size is 18x18 μm². The 2-D gratings on top of the detectors were then covered with Au/Ge and Au for Ohmic contact and reflection. Figure 38 shows twelve processed QWIP FPAs on a 3-inch GaAs wafer (Gunapala *et al.*, 1998a). Indium bumps were then evaporated on top of the detectors for silicon readout circuit (ROC) hybridization. A single QWIP FPA was chosen and hybridized (via indium bump-bonding process) to a 640x486 direct injection silicon readout multiplexer (Amber AE-181) and biased at V_B = -2.0 V. Figure 39 shows a size comparison of this large area long-wavelength QWIP FPA to a quarter. At temperatures below 70 K, the signal-to-noise-ratio of the system is limited by multiplexer readout noise, and shot-noise of the photo current. At temperatures above 70 K, temporal noise due to the QWIP's higher dark current becomes the limitation. As mentioned earlier, this higher dark current is due to thermionic emission and thus causes the charge storage capacitors of the readout circuitry to saturate (Gunapala *et al.*, 1998a). Since the QWIP is a high impedance device, it should yield a very high charge injection coupling efficiency into the integration capacitor of the multiplexer. In fact Bethea *et al.* (1993) have demonstrated charge injection efficiencies approaching 90%. Charge injection efficiency can be obtained from (Bethea *et al.*, 1993)

$$\eta_{inj} = \frac{g_m R_{Det}}{1 + g_m R_{Det}} \left[\frac{1}{1 + \frac{j\omega C_{Det} R_{Det}}{1 + g_m R_{Det}}} \right] \quad (31)$$

where g_m is the transconductance of the MOSFET and is given by $g_m = eI_{Det}/kT$. The differential resistance R_{Det} of the pixels at -2 V bias is 5.4×10^{10} Ohms at $T=70$ K, and detector capacitance C_{Det} is 1.4×10^{-14} F. The detector dark current $I_{Det} = 24$ pA under the same operating conditions. According to equation (31) the charge injection efficiency $\eta_{inj} = 99.5\%$ at a frame rate of 30 Hz. The FPA was back-illuminated through the flat thinned substrate membrane (thickness ≈ 1300 Å). This thinned GaAs FPA membrane completely eliminated the thermal mismatch between the silicon CMOS readout multiplexer and the GaAs based QWIP FPA. Basically, the thinned GaAs based QWIP

FPA membrane adapts to the thermal expansion and contraction coefficients of the silicon readout multiplexer. Thus, thinning has played an extremely important role in the fabrication of large area FPA hybrids. In addition, this thinning has completely eliminated the pixel-to-pixel optical cross-talk of the FPA. This initial array gave very good images with 99.97% of the pixels working, demonstrating the high yield of GaAs technology. The operability was defined as the percentage of pixels having noise equivalent differential temperature less than 100 mK at 300 K background with $f/2$ optics and, in this case, operability happened to be equal to the pixel yield.

We have used the following equation to calculate $NE\Delta T$ of the FPA

$$NE\Delta T = \frac{\sqrt{AB}}{D_B^* (dP_B / dT) \sin^2(\theta / 2)} \quad (32)$$

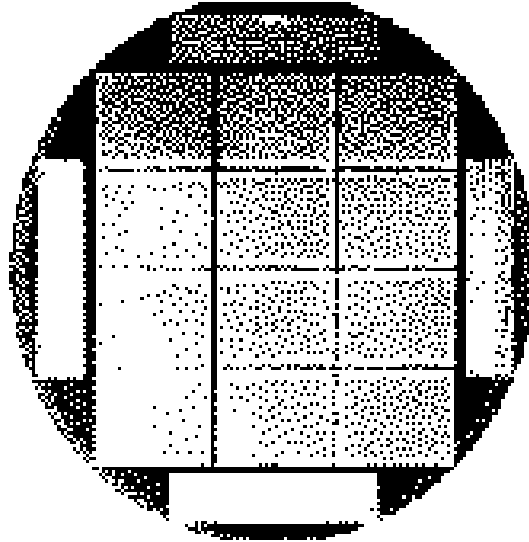


Fig. 38. Twelve 640 x 486 QWIP FPAs on a 3-inch GaAs wafer. (Gunapala *et al.*, 1997a)



Fig. 39. A size comparison of the 640 x 486 long-wavelength QWIP FPA to a quarter. (Gunapala *et al.*, 1997a)

where D_B^* is the blackbody detectivity, dP_B/dT is the derivative of the integrated blackbody power with respect to temperature, and θ is the field of view angle [i.e., $\sin^2(\theta/2) = (4f^2+1)^{-1}$, where f is the f-number of the optical system]. The background temperature $T_B = 300$ K, the area of the pixel $A = (18 \mu\text{m})^2$, the f-number of the optical system is 2, and the frame rate is 30 Hz. Figure 40 shows the experimentally measured $NE \cdot T$ histogram of the FPA at an operating temperature of $T = 70$ K, bias

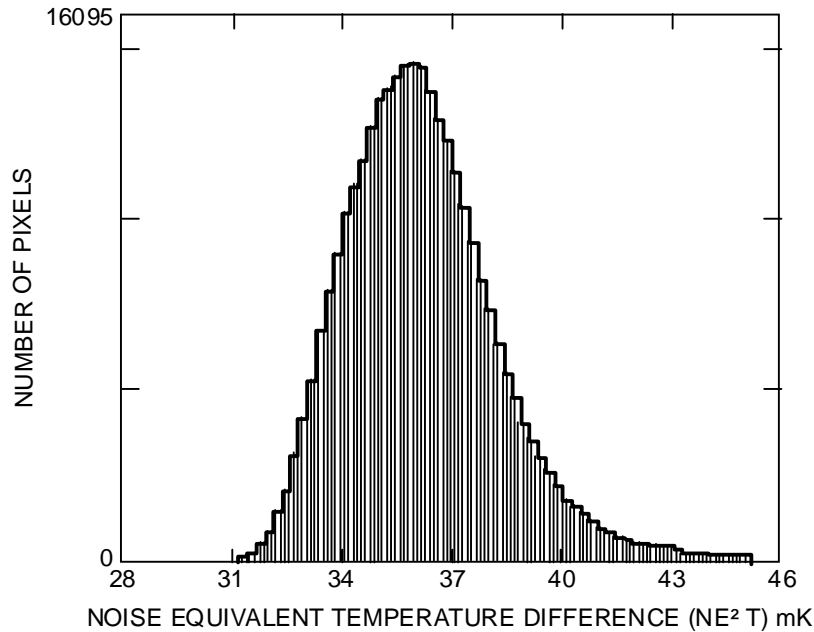


Fig. 40. Noise equivalent temperature difference ($NE \cdot T$) histogram of the 311,040 pixels of the 640 x 486 array showing a high uniformity of the FPA. The uncorrected non-uniformity (= standard deviation/mean) of this unoptimized FPA is only 5.6% including 1% non-uniformity of ROC and 1.4% non-uniformity due to the cold-stop not being able to give the same field of view to all the pixels in the FPA. (Gunapala *et al.*, 1998a)

$V_B = -2$ V, and 300 K background with $f/2$ optics. The mean value of the $NE \cdot T$ histogram is 36 mK (Gunapala *et al.*, 1998a). This agrees reasonably well with our estimated value of 25 mK based on test structure data. The read noise of the multiplexer is 500 electrons. The 44% shortfall of $NE \cdot T$ is mostly attributed to unoptimized detector bias (i.e., $V_B = -2$ V was used instead of optimum $V_B = -3$ V based on detectivity data as a function of bias voltage), decrease in bias voltage across the detectors during charge accumulation (common in many direct injection type readout multiplexers), and read noise of the readout multiplexer. The experimentally measured peak quantum efficiency of the FPA was 2.3% (lower FPA quantum efficiency is attributed to 51% fill factor and 30% reflection loss from the GaAs back surface). Therefore, the corrected quantum efficiency of the focal plane detectors is 6.5% and this corresponds to an average of two passes of infrared radiation through the photosensitive MQW region.

A 640X486 QWIP FPA hybrid was mounted onto a 84-pin lead-less chip carrier and installed into a laboratory dewar which was cooled by liquid nitrogen to demonstrate a LWIR imaging camera. The FPA was cooled to 70K by pumping on liquid nitrogen and the temperature was stabilized by regulating the pressure of gaseous nitrogen. The other element of the camera is a 100 mm focal length AR coated germanium lens, which gives a $9.2^\circ \times 6.9^\circ$ field of view. It is designed to be transparent in the 8-12 μm wavelength range for compatibility with the QWIP's 8-9 μm operation. An Amber ProViewTM image processing station was used to obtain clock signals for the readout multiplexer and to perform digital data acquisition and non-uniformity corrections. The digital data acquisition resolution of the camera is 12-bits, which determines the instantaneous dynamic range of the camera (i.e., 4096).

The measured mean $NE \cdot T$ of the QWIP camera is 36 mK at an operating temperature of $T = 70$ K, bias $V_B = -2$ V, and 300 K background with $f/2$ optics. This is in good agreement with expected FPA sensitivity due to the practical limitations on charge handling capacity of the multiplexer, read noise, bias voltage and operating temperature. The uncorrected $NE \cdot T$ non-uniformity (which includes a 1% non-uniformity of the ROC and a 1.4% non-uniformity due to the cold-stop in front of the FPA not yielding the same field of view to all the pixels) of the 311,040 pixels of the 640x486 FPA is about 5.6% ($= \text{sigma} / \text{mean}$). The non-uniformity of the FPA after two-point (17 $^\circ$ and 27 $^\circ$ Celsius) correction improves to an impressive 0.04%. As mentioned earlier, this high yield is due to the excellent GaAs growth uniformity and the mature GaAs processing technology. After two point correction, measurements of the residual nonuniformity were made at temperatures ranging from 10 $^\circ$ C (the cold temperature limit of the blackbody source) up to 40 $^\circ$ C. The non-uniformity at each temperature was found by averaging 16 frames, calculating the standard deviation of the pixel-to-pixel variation of the 16 frame average and then dividing by the mean output, producing non-uniformity that may be reported as a percentage. For camera systems that have $NE \cdot T$ of about 30 mK, the corrected image must have less than 0.1% non-uniformity in order to be standard television (TV) quality. Only at a temperature of 38 Celsius did the camera's non-uniformity exceed the 0.1% non-uniformity threshold. Figure 41 shows residual non-uniformity plotted versus scene temperature. The 33 Celsius window where the correction is below 0.1% is based on the

measured data and one extrapolated data point at 5 Celsius.

Video images were taken at a frame rate of 30 Hz at temperatures as high as $T = 70$ K using a ROC capacitor having a charge capacity of 9×10^6 electrons (the maximum number of photoelectrons and dark electrons that can be counted in the integration time of each detector pixel). Figure 42 show a frame of video image taken with this long-wavelength 640x486 QWIP camera. This image was taken in the night (around midnight) and it clearly shows where automobiles were parked during the day time. These high resolution images are comparable to standard TV, and demonstrate high operability (i.e., 99.9%) and stability (i.e., lower residual uniformity and $1/f$ noise) of the 640 x 486 long-wavelength QWIP staring array camera (Gunapala *et al.*, 1998a).

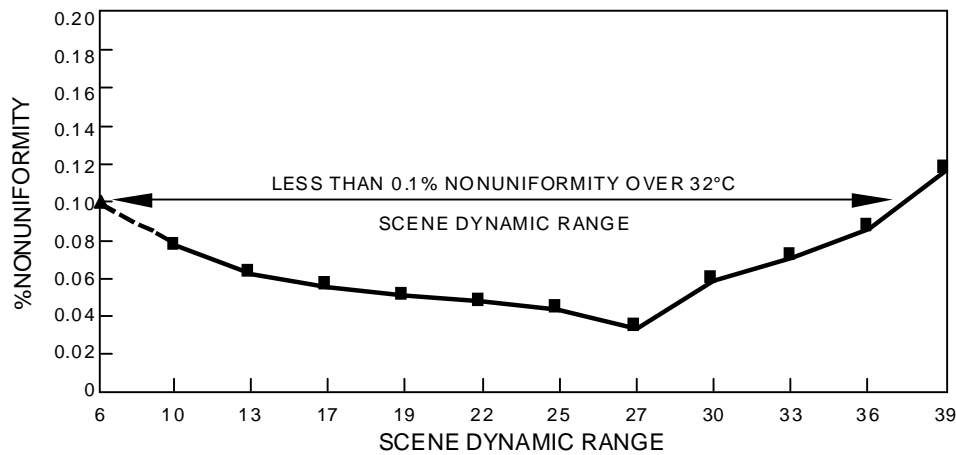


Fig. 41. Residual nonuniformity after two point correction as a function of scene temperature. This corrected uniformity range is comparable to 3-5 μ m IR cameras. (Gunapala *et al.*, 1998a)



Fig. 42. This picture was taken in the night (around midnight) and it clearly shows where automobiles were parked during the day time. This image demonstrates the high sensitivity of the 640 x 486 long-wavelength QWIP staring array camera. (Gunapala *et al.*, 1998a)

5.5 Dualband (MWIR & LWIR) Detectors

There are several applications such as target recognition and discrimination which require monolithic mid and long wavelength dualband large area, uniform, reproducible, low cost

and low $1/f$ noise infrared FPAs. For example, a dualband FPA camera would provide the absolute temperature of the target which is extremely important to the process of identifying temperature difference between targets, war heads and decoys. The GaAs based QWIP is a potential candidate for development of such a two-color FPAs. Until recently, the most developed and discussed two-color QWIP detector was the voltage tunable two stack QWIP. This device structure consists of two QWIP structures, one tuned for mid-wavelength detection and the other stack tuned for long-wavelength detection. This device structure utilizes the advantage of formation of electric field domains to select the response of one or the other detector (Grave *et al.*, 1993; Mei *et al.*, 1997). The difficulties associated with this type of two-color QWIP FPA are that these detectors need two different voltages to operate and long-wavelength sensitive segment of the device needs very high bias voltage (> 8 V) to switch on the LWIR detection. A voltage tunable simplified QWIP structure consisting of three quantum wells has been demonstrated by Tidrow and Bacher (1996). Due to a lower number of wells, the peak response wavelength of this detector can be tuned from 7.3 to 10 μm with smaller changes in the bias voltage. Chiang *et al.* (1996) also reported a multicolor voltage tunable triple-coupled QWIP using InGaAs/AlGaAs/GaAs for 8-12 μm detection. Another disadvantage of the voltage tunable scheme is that it does not provide simultaneous data from both wavelength bands.

Gunapala *et al.* (1998b) have developed a two-color, two stack, QWIP device structure based on $\text{In}_x\text{Ga}_{1-x}\text{As}/\text{Al}_y\text{Ga}_{1-y}\text{As}/\text{GaAs}$ material system for MWIR/LWIR detection (Foire *et al.*, 1994; Tidrow *et al.*, 1997). This structure can be processed in to dualband QWIP FPAs with dual or triple contacts to access the CMOS readout multiplexer. The device structure consists of a stack of 30 periods of LWIR MQW structure and another stack of 10 periods of MWIR MQW structure separated by a heavily doped 0.5 μm thick intermediate GaAs contact layer. The first stack (LWIR) consist of 10 periods of 500 Å $\text{Al}_x\text{Ga}_{1-x}\text{As}$ barrier and a GaAs well. This LWIR QWIP structure has been designed to have a bound-to-quasibound intersubband absorption peak at 8.5 μm , since the dark current of the device structure is expected to be dominated by the longer wavelength portion of the device structure. The second stack (MWIR) consist of 10 periods of, 300 Å $\text{Al}_x\text{Ga}_{1-x}\text{As}$ barrier and narrow $\text{In}_y\text{Ga}_{1-y}\text{As}$ well sandwiched between two thin layers of GaAs. This MWIR QWIP structure has been designed to have a bound-to-continuum intersubband absorption peak at 4.2 μm , since photo current and dark current of the MWIR device structure is relatively small compared to the LWIR portion of the device structure. This two-color QWIP structure is then sandwiched between 0.5 μm GaAs top and bottom contact layers doped $n = 5 \times 10^{17} \text{ cm}^{-3}$. The whole device structure was grown on a semi-insulating GaAs substrate by MBE. Then a 1.0 μm thick GaAs cap layer on top of a 300 Å $\text{Al}_{0.3}\text{Ga}_{0.7}\text{As}$ stop-etch layer is grown in situ on top of the device structure to fabricate the light coupling optical cavity.

The detectors were back illuminated through a 45° polished facet as described earlier and a simultaneously measured responsivity spectrum of vertically integrated dualband QWIP is shown in Fig. 43. The responsivity of the MWIR detector peaks at 4.4 μm and the peak responsivity (R_p) of the detector is 140 mA/W at bias $V_B = -3$ V. The spectral width and

the cutoff wavelength of the MWIR detector are $\bullet \lambda/\lambda = 20\%$ and $\lambda_c = 5 \mu\text{m}$ respectively. The responsivity of the LWIR detector peaks at $8.8 \mu\text{m}$ and the peak responsivity R_p of the detector is 150 mA/W at bias $V_B = -1.2 \text{ V}$. The spectral width and the cutoff wavelength of the LWIR detector are $\bullet \lambda/\lambda = 14\%$ and $\lambda_c = 9.4 \mu\text{m}$ respectively. The measured absolute peak responsivity of both MWIR and LWIR detectors are small, up to about $V_B = -0.5 \text{ V}$. Beyond that it increase nearly linearly with bias in both MWIR and LWIR detectors reaching $R_p = 210$ and 440 mA/W respectively at $V_B = -4 \text{ V}$. This type of responsivity behavior versus bias is typical for a bound-to-continuum and bound-to-quasibound QWIPs in MWIR and LWIR bands respectively. The peak quantum efficiency (45° double pass) of MWIR and LWIR detectors were 2.6% and 16.4% respectively at operating biases indicated in Fig. 43. The lower quantum efficiency of MWIR detector is due to the lower well doping density ($5 \times 10^{17} \text{ cm}^{-3}$) and lower number of quantum wells in the MQW region. The peak detectivities of both MWIR and LWIR detectors were estimated at different operating temperature and bias

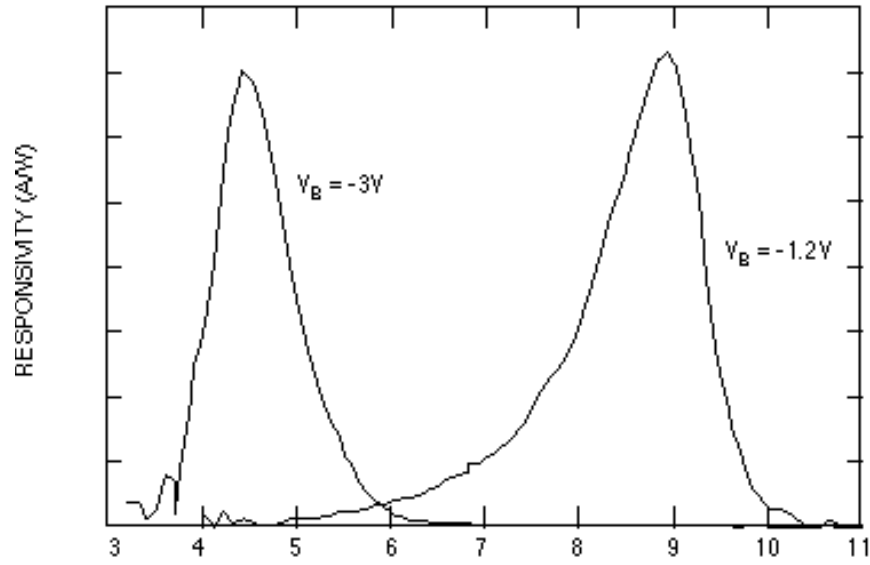


Fig. 43. Simultaneously measured responsivity spectrum of vertically integrated MWIR and LWIR dualband QWIP detector. (Gunapala *et al.*, 1998a)

voltages using experimentally measured noise currents (Gunapala *et al.*, 1998b). The MWIR peak detectivity $D_\lambda^* = 3.8 \times 10^{11} \text{ cm} \bullet \text{ Hz/W}$ has been achieved at $V_B = -1.8 \text{ V}$ and $T = 90 \text{ K}$. Similarly, LWIR peak detectivity $D^* = 8 \times 10^{11} \text{ cm} \bullet \text{ Hz/W}$ has achieved at $V_B = -1.1 \text{ V}$ and $T = 60 \text{ K}$.

5.6 Dualband (LWIR & VLWIR) Detectors

As we discussed in the previous section of this chapter, there are many target recognition and discrimination applications which require monolithic LWIR and VLWIR dualband large area FPAs as well. The general notion is that dualband target recognition and discrimination capability significantly improves with increasing wavelength separation between the two wavelength bands in consideration. Therefore, authors of this chapter are currently developing a 640x486 LWIR and VLWIR dualband QWIP FPA camera. Thus, we have developed the following QWIP device structure which can be processed into dualband QWIP FPAs with dual or triple contacts to access a CMOS readout multiplexer (Bois et al., 1995; Tidrow et al., 1997). Single indium bump per pixel is usable only in the case of an interlace readout scheme (i.e., odd rows for one color and the even rows for the other color) which uses an existing single color CMOS readout multiplexer. The advantages of this scheme are that it provides simultaneous data readout and allows it to use currently available single color CMOS readout multiplexers. However, the disadvantage is that it does not provide a full fill factor for both wavelength bands. This problem can be eliminated by fabricating $(n+1)$ terminals (e.g., three terminals for dualband) per pixel and hybridizing with a multicolor readout having n readout cells per detector pitch, where n is the number of wavelength bands.

The device structure (Gunapala *et al.*, 1998b) consists of a stack of 25 periods of LWIR QWIP structure and another stack of 25 periods of VLWIR QWIP structure separated by a heavily doped $0.5\ \mu\text{m}$ thick intermediate GaAs contact layer. The first stack (VLWIR) consist of 25 periods of, $500\ \text{\AA}$ $\text{Al}_x\text{Ga}_{1-x}\text{As}$ barrier and a GaAs well. This VLWIR QWIP structure has been designed to have a bound-to-quasibound intersubband absorption peak at $15\ \mu\text{m}$, since the dark current of the device structure is expected to dominated by the longer wavelength portion of the device structure. The second stack (LWIR) consist of 25 periods of $500\ \text{\AA}$ $\text{Al}_x\text{Ga}_{1-x}\text{As}$ barrier and a narrow GaAs well. This LWIR QWIP structure has been designed to have a bound-to-continuum intersubband absorption peak at $8.5\ \mu\text{m}$, since photo current and dark current of the LWIR device structure are relatively small compared to the VLWIR portion of the device structure. This whole dualband QWIP structure is then sandwiched between $0.5\ \mu\text{m}$ GaAs top and bottom contact layers doped $n = 5 \times 10^{17}\ \text{cm}^{-3}$, and has grown on a semi-insulating GaAs substrate by MBE. Then a $1.0\ \mu\text{m}$ thick GaAs cap layer on top of a $300\ \text{\AA}$ $\text{Al}_{0.3}\text{Ga}_{0.7}\text{As}$ stop-etch layer has to be grown in situ on top of the device structure for the fabrication of a light coupling optical cavity.

The detectors were back illuminated through a 45° polished facet as described earlier and a simultaneously measured responsivity spectrum of vertically integrated dualband QWIP is shown in Fig. 44. The responsivity of the LWIR detector peaks at $8.3\ \mu\text{m}$ and the peak responsivity R_p of the detector is $260\ \text{mA/W}$ at bias $V_B = -2.5\ \text{V}$. The spectral width and the cutoff wavelength of the LWIR detector are $\bullet\ \lambda/\lambda_c = 19\%$ and $\lambda_c = 9.3\ \mu\text{m}$

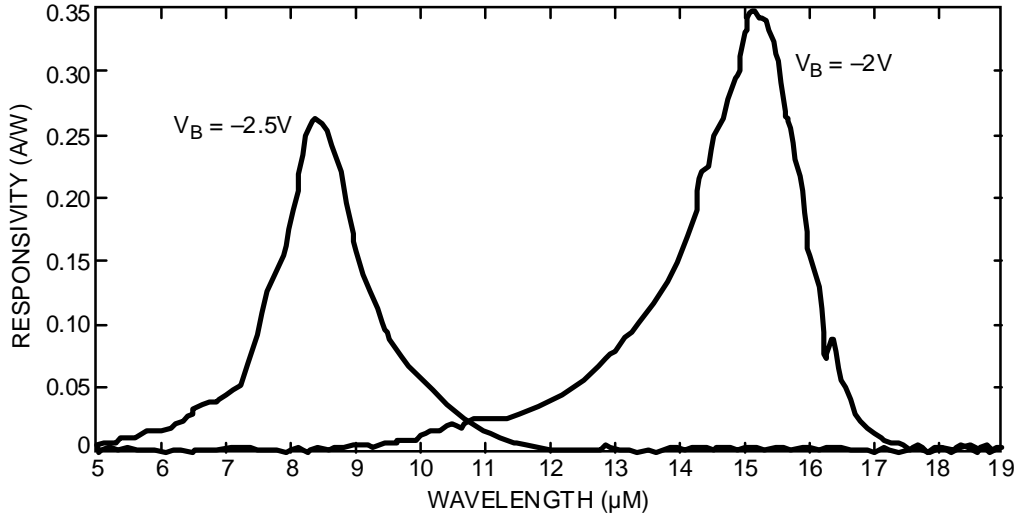


Fig. 44. Simultaneously measured responsivity spectrum of vertically integrated LWIR and VLWIR dualband QWIP detector. (Gunapala *et al.*, 1998a)

respectively. The responsivity of the VLWIR detector peaks at 15.2 μm and the peak responsivity (R_p) of the detector is 340 mA/W at bias $V_B = -2.0$ V. The spectral width and the cutoff wavelength of the LWIR detector are $\Delta\lambda/\lambda = 12\%$ and $\lambda_c = 15.9$ μm respectively. The peak quantum efficiency (45% double pass) of LWIR and VLWIR detectors were 12.6% and 9.8% respectively at operating biases indicated in Fig. 44. The peak detectivities of both LWIR and VLWIR detectors were estimated at different operating temperatures and bias voltages using experimentally measured noise currents (Gunapala *et al.*, 1998b). The peak detectivities D_λ^* of LWIR and VLWIR detectors were 1.8×10^{12} $\text{cm}^2 \cdot \text{Hz/W}$ (at $T = 55\text{K}$ and $V_B = -1.0$) and 1.5×10^{12} $\text{cm}^2 \cdot \text{Hz/W}$ (at $T = 35\text{K}$ and $V_B = -1.0$) respectively.

5.7 High Performance QWIPs for Low Background Applications

In this section, we discuss the demonstration of high performance QWIPs for low background applications by Gunapala *et al.* (1998b). Improving QWIP performance depends largely on minimizing the Shott noise of the dark current and improving the quantum efficiency. Equations (4) and (5) in section 3.2 were used to analyze the dark current of a QWIP which has a intersubband absorption peak in long-wavelength region. Figure 45 shows the estimated total dark currents (thermionic + thermionic assisted tunneling + tunneling), and experimental dark current of a QWIP sample which has a cutoff wavelength $\lambda_c = 10$ μm . According to the calculations, tunneling through the barriers dominates the dark current at temperatures below 30K, and at temperatures above 30 K, thermionic emission into the continuum transport state dominates the dark current.

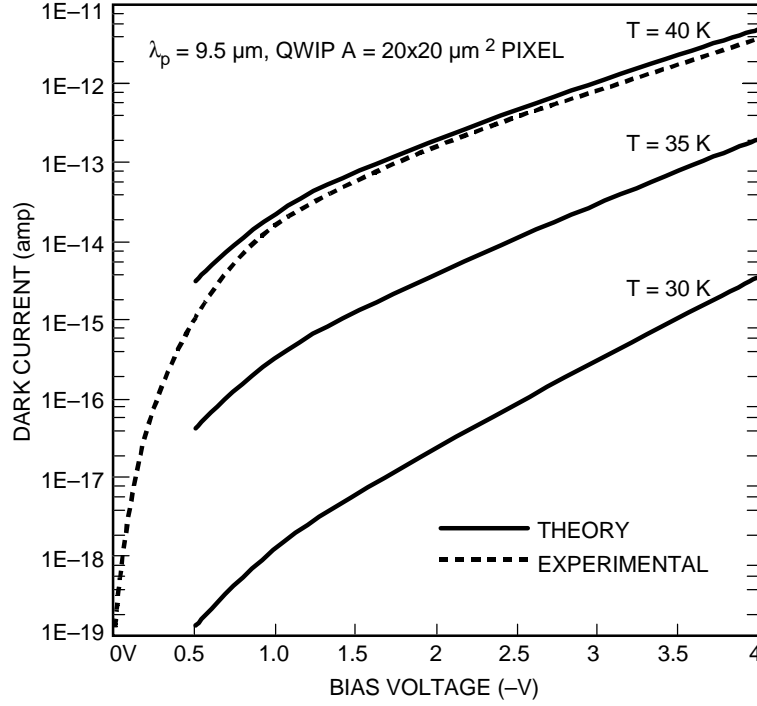


Fig. 45. Comparison of experimental (solid curves) and theoretical (dashed) dark current versus bias voltage curves at various temperatures for a 10 μm cutoff QWIP. (Gunapala *et al.*, 1998a)

For this experiment, eight n-type doped QWIP device structures were grown using MBE. The quantum well widths L_w range from 35 to 50 \AA , while the barrier widths are approximately constant at $L_b = 500 \text{ \AA}$. The Al molar fraction in the $\text{Al}_x\text{Ga}_{1-x}\text{As}$ barriers varied from $x = 0.24$ to 0.30 (corresponding to cutoff wavelengths of $\lambda_c = 8.3 - 10.3 \text{ }\mu\text{m}$). The photosensitive doped MQW region (containing 25 to 50 periods) is sandwiched between similarly doped top (0.5 μm) and bottom (0.5 μm) ohmic contact layers. These structural parameters have been chosen to give a very wide variation in QWIP absorption and transport properties. All eight QWIP samples are n-doped with intersubband infrared transition occurring between a single localized bound state in the well and a delocalized state in the continuum. Thus, in the presence of an electric field, the photoexcited carrier can be effectively swept out of the quantum well region.

All eight QWIP samples were processed into 200 μm diameter mesas (area = $3.14 \times 10^{-4} \text{ cm}^2$) using wet chemical etching and Au/Ge ohmic contacts were evaporated onto the top and bottom contact layers. The dark current versus voltage curves for all samples were measured as a function of temperature from $T = 40\text{--}70 \text{ K}$ and Fig. 45 shows the current-voltage curve of one sample. As expected, Fig. 45 clearly shows that the $T = 40 \text{ K}$ dark current of these QWIP devices are many orders of magnitude smaller than the dark current at $T = 70 \text{ K}$. This clearly indicates that the dark current of these devices are thermionically dominant down to 40 K and the tunneling induced dark current is insignificant.

The detectors were back illuminated through a 45 \times polished facet and their normalized responsivity spectrums are shown in Fig. 46. The responsivities of all device structures

peaked in the range from 7.7 μm and 9.7 μm . The peak responsivities (R_p), spectral widths ($\bullet \lambda$), cutoff wavelengths (λ_c) and quantum efficiency photoconductive gain products ($\eta \times g$) are listed in Table IV. It is worth noting that ηg product of sample four has increased to 17%. This is approximately a factor of 24 increase in ηg product compared to ηg product of QWIP devices designed for high background and high temperature operation. This large enhancement was achieved by (i) improving quantum efficiency per well as a result of higher well doping density, (ii) operating at a higher electric field, i.e. higher gain. Number of periods in the structure was reduced to 30 (typically 50) in order to increase the applied electric field while keeping operating bias voltage at the same. The current noise i_n was estimated using measured optical gain and dark current. The peak detectivity D^* can now be calculated from $D^* = R \sqrt{A \Delta f} / i_n$, where A is the area of the detector and $A = 27 \times 27 \mu\text{m}^2$. Table V shows the D^* values of both device structures at various bias voltages at $T = 40 \text{ K}$. These data clearly show that detectivities of 10 μm cutoff QWIPs reach mid $10^{13} \text{ cm} \cdot \text{Hz/W}$ at $T = 40 \text{ K}$. As shown in Table V, these detectors are not showing background limited performance (BLIP) for moderately low background of $2 \times 10^9 \text{ photons/cm}^2/\text{sec}$ at $T = 40 \text{ K}$ operation. Since the dark current of these detectors is thermionically limited down to $T = 30 \text{ K}$, these detectors should demonstrated a BLIP at $T = 35 \text{ K}$ for $2 \times 10^9 \text{ photons/cm}^2/\text{sec}$ background.

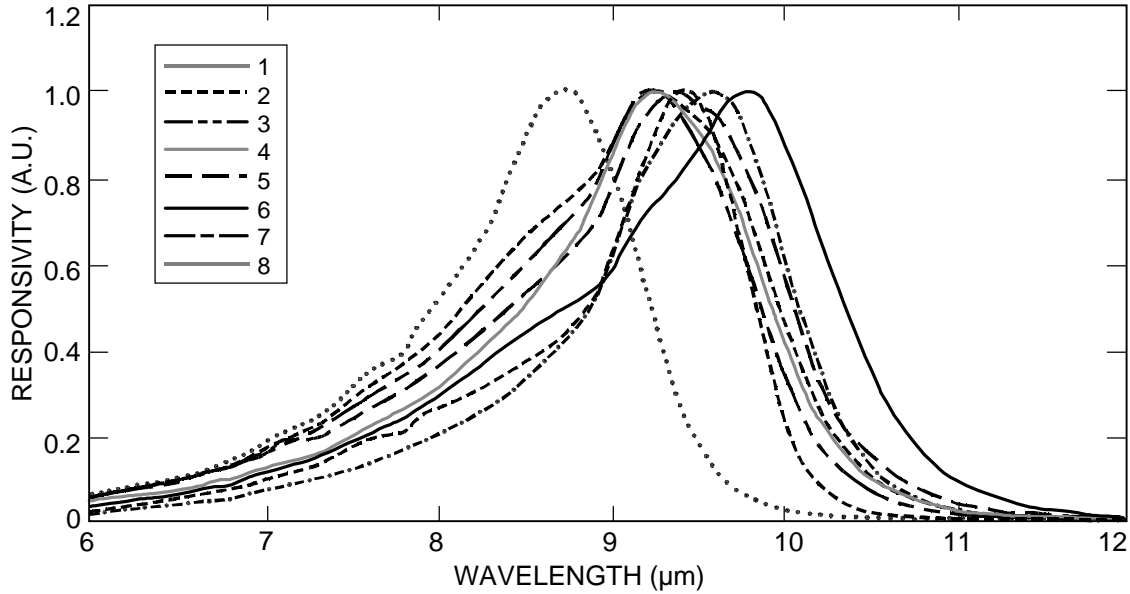


Fig. 46. Normalized responsivity spectra versus wavelength at $T=40 \text{ K}$ for all samples. (Gunapala *et al.*, 1998a)

Table IV. Responsivity spectral parameters of all eight samples. (Gunapala *et al.*, 1998b)

Sample	Spectral Response (μm)			Device Performance (Detector Area $3.1 \times 10^{-4} \text{ cm}^2$)		
	λ_p	50% λ_c	$\Delta\lambda$	Peak Rp A/W @ 2V	Q.E. x Gain %	Dark Current @ 50K
1	9.6	10.1	1.1	0.65	8.4	1.1 E-11
2	9.4	10.1	1.6	0.61	8.0	8.0 E-11
3	9.3	9.8	1.6	0.38	5.2	2.0 E-11
4	9.3	9.8	1.2	1.26	17.0	9.0 E-11
5	9.4	10.0	1.8	0.46	6.1	1.0 E-10
6	9.7	10.3	1.5	0.54	5.3	3.0 E-10
7	8.5	8.9	1.0	0.15	2.2	1.0 E-12
8	7.7	8.3	1.3	0.34	5.5	2.5 E-12

Table V. Responsivity, quantum efficiency, photoconductive gain, and detectivity of the first and the fourth sample at $T = 40 \text{ K}$. (Pixel Area: $27 \mu\text{m} \times 27 \mu\text{m}$, Background Flux: $2 \times 10^9 \text{ photons/cm}^2/\text{sec}$) (Gunapala *et al.*, 1998b)

Sample	Peak W.L. (μm)	Bias (V)	Responsivity (A/W)	Q.E. x Gain %	ABS. Q.E. @ 300K	ABS. Q.E. @ 40K	Optical Gain	Dark Current @ 40K (A)	Photo- Current (A)	Detectivity $\text{cm Hz}^{1/2}/\text{W}$
1	9.6	1.0	0.24	3.1	14.1	18.3	0.17	1.2 E-15	7.2 E-17	5.7 E+13
		2.0	0.65	8.4	14.1	18.3	0.46	2.3 E-15	1.9 E-16	6.8 E+13
		3.0	0.66	8.5	14.1	18.3	0.47	9.3 E-15	2.0 E-16	3.4 E+13
		4.0	0.68	8.8	14.1	18.3	0.48	1.4 E-14	2.1 E-16	2.8 E+13
4	9.3	1.0	0.43	5.7	17.0	22.1	0.26	7.0 E-15	1.3 E-16	3.4 E+13
		2.0	1.26	16.8	17.0	22.1	0.76	9.3 E-15	3.9 E-16	5.1 E+13
		3.0	1.35	18.0	17.0	22.1	0.81	3.5 E-14	4.2 E-16	2.7 E+13
		4.0	1.36	18.1	17.0	22.1	0.82	2.3 E-13	4.2 E-16	1.1 E+13

5.8 Broad-band QWIPs for Thermal Infrared Imaging Spectrometers

Until recently, QWIP detectors have been available only over narrow bands (typically 1.0 - 2.0 μm wide) in the 6 - 20 μm spectral range. Bandara *et al.* (1998b) have developed a broadband test detector that will cover the 10 - 16 μm band and FPAs of these detectors can be mated to a 640x480 multiplexer (see Fig. 47). This detector has been developed specifically for thermal infrared imaging spectrometers—anticipating a possible need for

Mars exploration. This program required a thermal infrared imaging spectrometer with minimum power, mass, and volume. One attractive instrument concept involved a Spatially Modulated Infrared Spectrometer (SMIS) to cover the LWIR and VLWIR spectral ranges. This instrument does not contain any moving mirrors because it uses the spatially modulated Fourier Transform spectroscopy technique. Another advantage of this concept is that it has a substantially higher signal flux because all of the photons entering the pupil are used. The high spectral resolution version of this instrument requires larger format FPAs (at least 640x486) with high pixel to pixel uniformity. The lack of large format, uniform LWIR and VLWIR FPA technology has prevented the development of such highly sensitive and robust thermal infrared spectrometers. That has changed recently due to demonstration of highly uniform, large format QWIP FPAs with lower 1/f noise, at a lower cost than any other LWIR detector. In addition, the use of external filters can be avoided because QWIP can be designed to have sharp spectral cut-offs at required wavelengths. Francis Reininger, at JPL, has demonstrated this concept by building a prototype laboratory instrument working with a 8-9 μm QWIP 640x486 FPA. The unique characteristic of this instrument (besides being small and efficient) is that it has one instrument line shape for all spectral colors and spatial field positions. By using broad-band QWIP arrays with wavelengths out to 16 μm , the next version of this

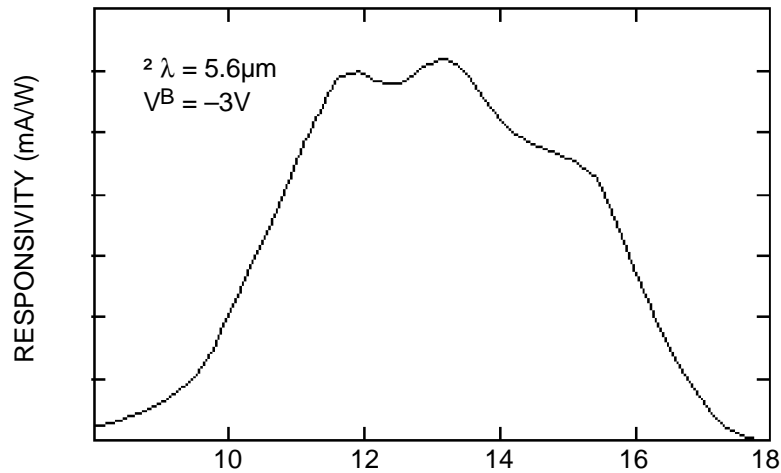


Fig. 47. Experimental measurements of the normalized responsivity spectrum of 10-16 μm broad-band QWIP at bias voltage $V_B = -4$ V. (Gunapala *et al.*, 1998a)

instrument could become the first compact, high resolution thermal infrared, hyper-spectral imager with a single spectral line shape and zero spectral smile. Such an instrument is in strong demand by scientists studying Earth and planetary science.

6. APPLICATIONS

6.1 Fire Fighting

Recently, 256 x 256 hand-held QWIP cameras have been used to demonstrate various possible applications in science, medicine, industry, defense, etc. A 256 x 256 portable LWIR QWIP camera helped a Los Angeles TV news crew get a unique perspective on fires that raced through the Southern California seaside community of Malibu in October, 1996. The camera was used on the station's news helicopter. This portable camera features infrared detectors which cover longer wavelengths than previous portable cameras could. This allows the camera to see through smoke and pinpoint lingering hotspots which are not normally visible. This enabled the TV station to transmit live images of hotspots in areas which appeared innocuous to the naked eye. These hotspots were a source of concern for firefighters, because they could flare up even after the fire appeared to have subsided. Figure 48 shows the comparison of visible and infrared images of a just burned area as seen by the news crew in nighttime. It works effectively in both daylight and nighttime conditions. The event marked the QWIP camera's debut as a fire observing device (Gunapala *et al.*, 1998c).

6.2 Volcanology

A similar 256 x 256 LWIR QWIP camera has been used to observe volcanoes, mineral formations, weather and atmospheric conditions at the Kilauea Volcano in, Hawaii. The objectives of this trip were to map geothermal features. The wide dynamic range enabled volcanologists to image volcanic features at temperatures much higher (300 - 1000 C) than can be imaged with conventional thermal imaging systems in the 3 - 5 μm range or in visible (Realmuto *et al.*, 1997). Figure 49 shows the comparison of visible and infrared images of the Kilauea Volcano in Hawaii. The infrared image of the volcano clearly shows a hot lava tube running underground which is not visible to the naked eye.

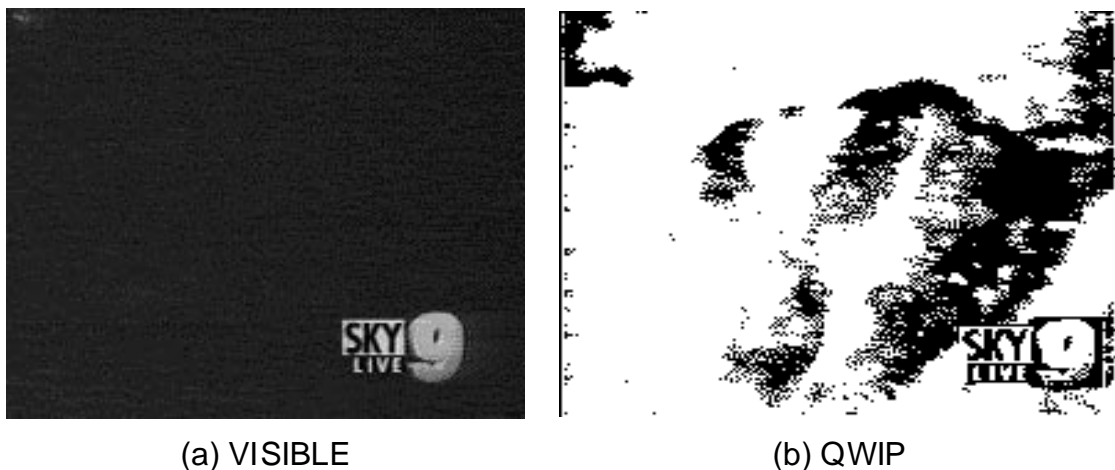


Fig. 48. Comparison of visible and infrared images of a just burned area as seen by a highly sensitive visible CCD camera and the long wavelength infrared camera in nighttime. (a) Visible image from a CCD camera. (b) Image from the 256x256 portable QWIP camera. Infrared imagery clearly enables firefighters

to locate the hotspots in areas which appeared innocuous to the naked eye. These hotspots are a source of concern for firefighters, because fire can flare up even after it appears to have subsided. (Gunapala *et al.*, 1998a)

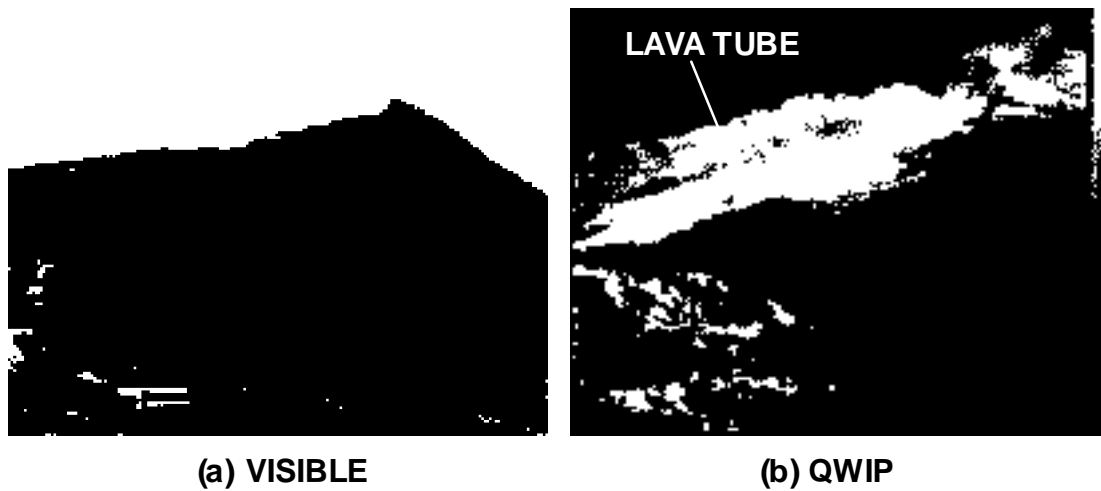


Fig. 49. Comparison of visible and infrared images of the Mount Kilauea Volcano in, Hawaii. (a) Visible image from a highly sensitive CCD camera. (b) Image from the 256x256 portable QWIP camera. The wide dynamic range enabled us to image volcanic features at temperatures much higher (300 - 1000 C) than can be imaged with conventional thermal imaging systems in the 3 - 5 μm range or in visible. The infrared image of the volcano clearly show a hot lava tube running underground which is not visible to the naked eye. This demonstrates the advantages of long wavelength infrared in geothermal mapping. (Gunapala *et al.*, 1998a)

6.3 Medicine

A group of researchers from the State University of New York in Buffalo and Walter Reed Army Institute of Research in Washington DC has used a 256x256 LWIR QWIP camera in the Dynamic Area Telethermometry (DAT). DAT has been used to study the physiology and patho-physiology of cutaneous perfusion, which has many clinical applications. DAT involves accumulation of hundreds of consecutive infrared images and fast Fourier transform (FFT) analysis of the biomodulation of skin temperature, and of the microhomogeneity of skin temperature. The FFT analysis yields the thermoregulatory frequencies and amplitudes of temperature and HST modulation (HST, which measures the perfusion of the skin's capillaries). To obtain reliable DAT data, one needs an infrared camera in the $>8 \mu\text{m}$ range (to avoid artifacts of reflections of modulated emitters in the environment), a repetition rate of 30 Hz (allowing accumulation of a maximal number of images during the observation period to maximize the resolution of the FFT), frame to frame instrumental stability (to avoid artifact stemming from instrument modulation), and sensitivity of less than 50 mK. According to these researchers, the longer wavelength operation, higher spatial resolution, higher sensitivity, and greater stability of the QWIP RADIANCETM made it the best choice of all infrared cameras.

This camera has also been used by a group of researchers at the Texas Heart Institute in a heart surgery experiment performed on a rabbit heart. This experiment clearly revealed that it is possible to detect arterial plaque built inside a heart by thermography. Figure 50

clearly shows arterial plaque accumulated in a rabbit heart.

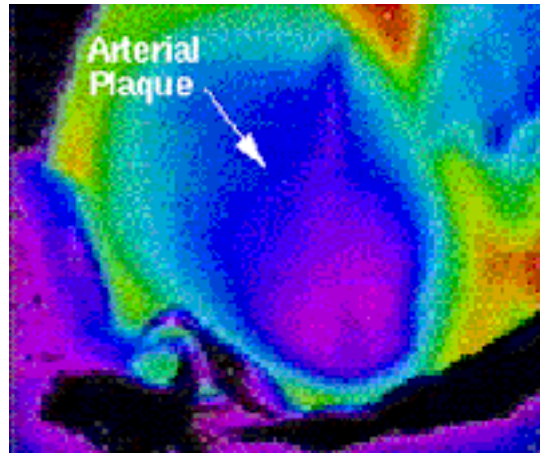


Fig. 50. This image shows arterial plaque deposited in a rabbit heart. (Gunapala *et al.*, 1998a)

6.4 Defense

It is not necessary to explain how real time infrared imaging is important in surveillance, reconnaissance and military operations. The QWIP RADIANCE™ was used by the researchers at the Ballistic Missile Defense Organization's innovative science and technology experimental facility in a unique experiment to discriminate and clearly identify the cold launch vehicle from its hot plume emanating from rocket engines.

Usually, the temperature of cold launch vehicles is about 250• C, whereas the temperatures of the hot plume emanating from launch vehicle can reach 950• C. According to the Plank's blackbody emission theory, the photon flux ratio of 250• C and 950• C blackbodies at 4 μm is about 25,000, whereas the same photon flux ratio at 8.5 μm is about 115 (see Figure 51). Thus, it is very clear that one must explore longer wavelengths for better cold-body versus hot plume discrimination (Gunapala *et al.*, 1998c), because the highest instantaneous dynamic range of infrared cameras is usually 12-bits (i.e., 4096) or less. Figure 52 shows a image of Delta-II launch taken with QWIP RADIANCE™ camera. This clearly indicates the advantage of long-wavelength QWIP cameras in the discrimination and identification of cold launch vehicles in the presence of hot plume during early stages of launch.

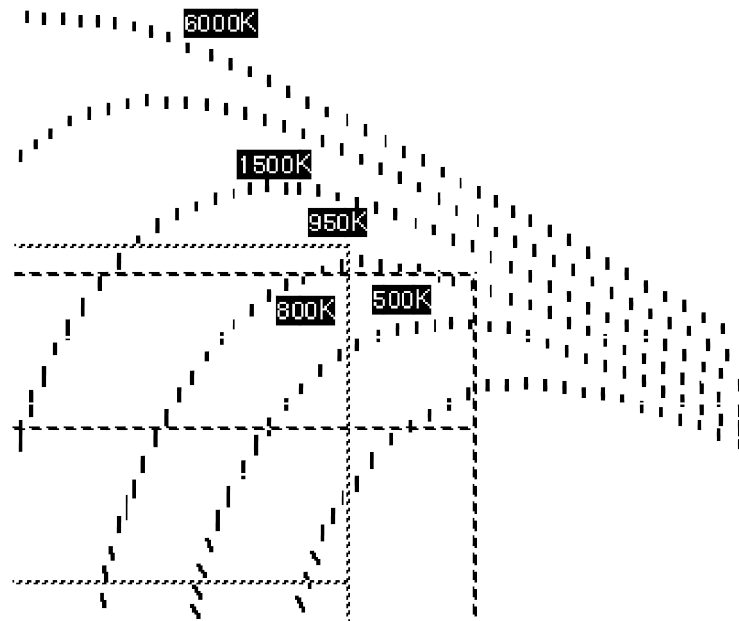


Fig. 51. Blackbody spectral radiant photon emittance at various temperatures. (Gunapala *et al.*, 1998a)

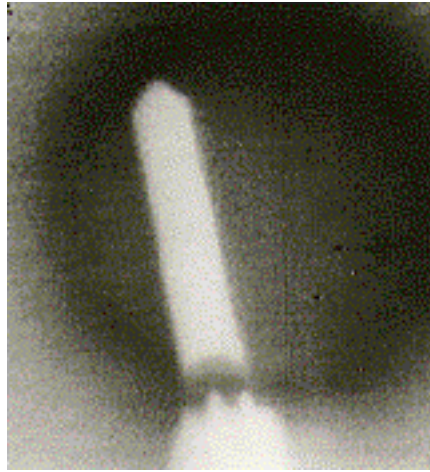


Fig. 52. Image of a Delta-II launch vehicle taken with the long-wavelength QWIP RADIANCE during the launch. This clearly indicates the advantage of long-wavelength QWIP cameras in the discrimination and identification of cold launch vehicles in the presence of hot plume during early stages of launch. (Gunapala *et al.*, 1998a)

6.5 Astronomy

In this section, we discuss the first astronomical observations with a QWIP FPA. In order to perform this astronomical observation, we designed a QWIP wide-field imaging multi-color prime-focus infrared camera (QWICPIC). Observations were conducted at the five meter Hale telescope at Mt. Palomar with QWICPIC based on a 8-9 μm 256x256 QWIP FPA operating at $T=35\text{ K}$. The ability of QWIPs to operate under high photon backgrounds without excess noise enables the instrument to observe from the prime focus with a wide 2'x2' field of view, making this camera unique among the suite of infrared instruments available for astronomy. The excellent 1/f noise performance (see Fig. 53) of QWIP FPAs allows QWICPIC to observe in a slow scan strategy often required in infrared observations from space (Gunapala *et al.*, 1998c).

Figure 54 compares an image of the Orion nebula obtained in a brief 30 minute observation with an engineering grade QWIP FPA to a visible image of the Orion nebula taken with the wide field planetary camera in Hubble Space Telescope (HST). In addition to the well-known infrared bright BN-KL object in the upper right-hand corner, careful comparison of the infrared images with optical and near-infrared images obtained by HST reveal a multitude of infrared sources which are dim or undetectable in visible. These images demonstrate the advantage of large format, stable (low 1/f noise) LWIR QWIP FPAs for surveying obscured regions in search for embedded or reddened objects such as young forming stars.

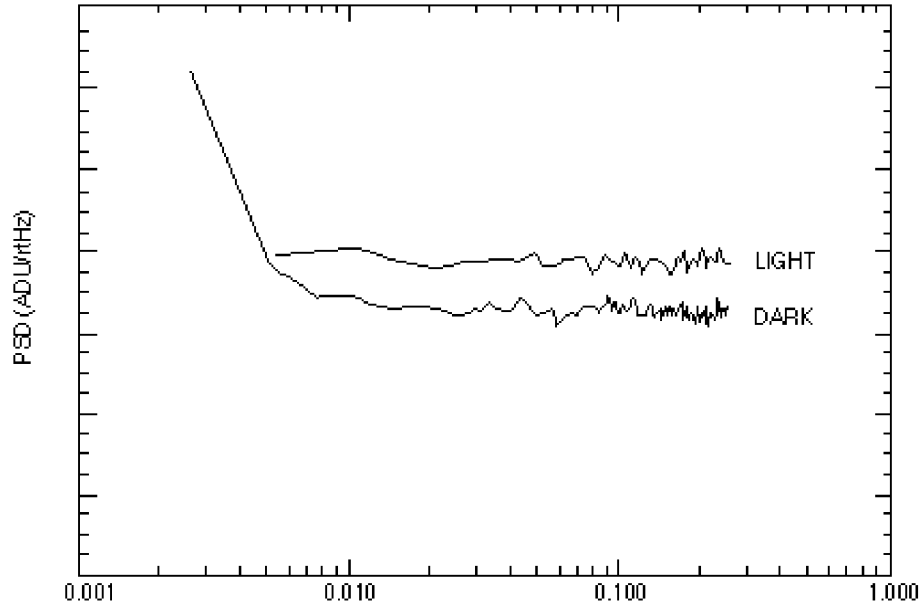


Fig. 53. $1/f$ noise spectrum of $8\text{-}9\text{ }\mu\text{m}$ 256×256 QWIP FPA. (1 ADU = 430 electrons). This clearly shows that QWIPs have no $1/f$ down to 30 mHz. This allows QWIP based instruments to use longer integration times and frame adding capability. (Gunapala *et al.*, 1998a)

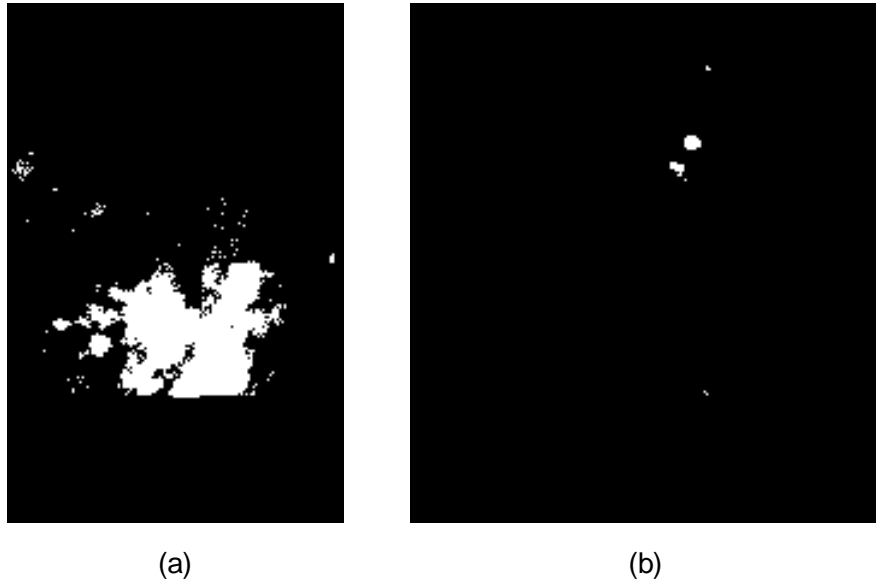


Fig. 54 (a). Visible image of the Orion nebula taken with the wide field planetary camera in Hubble Space Telescope. (b) $8\text{-}9\text{ }\mu\text{m}$ infrared image of the Orion nebula taken with an engineering grade 256×256 QWIP FPA at five meter Hale telescope at Mt. Palomar. (Gunapala *et al.*, 1998a)

7. SUMMARY

Various types of GaAs/AlGaAs based QWIPs, QWIPs with other materials systems, figures of merit, light coupling methods, QWIP imaging arrays, and some applications of QWIP FPAs were reviewed. Our discussion of QWIPs has been necessarily brief and the

literature references cited are not all inclusive, but represent a selection of key articles from a historic and technical point of view. Exceptionally rapid progress has been made in the understanding of intersubband absorption and carrier transport in the QWIP device structure and practical demonstration of large, sensitive, two-dimensional QWIP imaging FPAs since they were first demonstrated only several years ago. This remarkable progress was due to the highly mature III-V growth and processing technologies. As discussed in sub-section 5.7, an important advantage of QWIPs over the HgCdTe is that, as the temperature is reduced, D^* increases dramatically reaching $D_\lambda^* = 10^{14} \text{ cm}^2 \cdot \text{Hz/W}$ at $T = 30 \text{ K}$ and even larger values at lower temperatures. Even though a detailed discussion of cooling methods are outside of the scope of this chapter, it should be noted that advances in cooling technologies have kept pace with the detector developments. Efficient, light-weight mechanical and sorption coolers have been developed that can achieve temperatures down to 10 K. Thus, when QWIP technology utilizes the advanced cooling technologies, it can easily meet the stringent spectroscopic and imaging requirements of ground based and space borne applications in the LWIR and VLWIR spectral bands. As discussed in sections 5 and 6, rapid progress has been made in the performance ($NE \cdot T$) of long-wavelength QWIP FPAs, starting with bound-to-bound QWIPs which had relatively poor sensitivity, and culminating in high performance bound-to-quasibound QWIP FPAs with various light coupling schemes. In conclusion, very sensitive, low cost, large (2048x2048) LWIR and VLWIR QWIP FPAs can be expected in the near future.

ACKNOWLEDGMENTS

We are grateful to C. P. Bankston, M. Bothwell, J. Buckley, G. M. Burdick, M. T. Chahine, T. Cole, D. Duston, W. Dyer, T. C. Frascchetti, S. K. Khanna, K. M. Koliwad, T. N. Krabach, C. A. Kukkonen, P. D. LeVan, R. H. Liang, T. R. Livermore, F. G. O'Callaghan, M. J. Sander, V. Sarohia, R. R. Stephenson, R. Wall, and B. A. Wilson for encouragement and support during the development and optimization of QWIP FPAs at Jet Propulsion Laboratory for various applications. Also, authors would like to give their special thanks to J. K. Liu and J. M. Mumolo of Jet Propulsion Laboratory for critical reading of the manuscript. In addition authors would like to express their thanks to H. H. Auman, E. R. Blazejewski, C. G. Bethea, J. J. Bock, R. Carralejo, N. Chand, K. K. Choi, M. L. Eastwood, J. Frank, J. Gill, D. E. Hagan, T. R. Hamilton, R. Hamm, G. Hasnain, W. S. Hobson, T. Hoelter, M. Hong, W. Hong, J. James, D. W. Juergens, A. B. Kahle, J. T. Kenny, R. F. Kopf, J. M. Kuo, S. Laband, A. L. Lane, T. L. Lin, J. Llorens, R. A. Logan, S. S. Li, H. C. Liu, J. K. Liu, E. M. Luong, P. D. Maker, M. J. McKelvey, R. E. Muller, J. M. Mumolo, D. A. Nichols, B. Pain, M. B. Panish, J. S. Park, S. S. Pei, L. Pfeiffer, H. R. Pollock, F. S. Pool, V. J. Realmuto, F. M. Reininger, M. E. Ressler, D. Ritter, G. Sarusi, C. A. Shott, J. J. Simmonds, A. Singh, R. B. Somoano, N. Stetson, R. C. Stirbl, M. Sundaram, M. Z. Tidrow, G. Udomkesmalee, D. Vincent, M. W. Werner, and A. Zussman who worked closely with us, for stimulating technical discussions, device processing, and crystal growth. The authors would like to give their special thanks to B. F. Levine of AT&T Bell Laboratories for his support and guidance received over the early years of QWIP development. Also, the authors are grateful to Dr. E. C. Stone, director of the Jet Propulsion Laboratory for his continuing support in this endeavor. The QWIP

FPA research and applications described in this chapter was performed partly by the Center for Space Microelectronics Technology, Jet Propulsion Laboratory, California Institute of Technology, and were jointly sponsored by the JPL Director's Research and Development Fund, the Ballistic Missile Defense Organization / Innovative Science & Technology Office and Exo-atmospheric Interceptor Technology Office, the National Aeronautics and Space Administration, Office of Space Science, and Air Force Research Laboratory.

REFERENCES

- Andersson, J. Y., Lundqvist, L., and Paska, Z. F. (1991a). Appl. Phys. Lett. **58**, 2264.
- Andersson, J. Y., and Lundqvist, L. (1991b). Appl. Phys. Lett. **59**, 857.
- Andersson, J. Y., Lundqvist, L., and Paska, Z. F. (1991c). J. Appl. Phys. **71**, 3600
- Andersson, J. Y., Alverbro, J., Borglind, J., Helander, P., Martijn, H., and Ostlund, M. (1997). SPIE Proceeding **3061**, 740.
- Andersson, T. G., Chen, Z. G., Kulakovskii, V. D., Uddin, A., and Vallin, J. T. (1988). Phys. Rev. B **37**, 4032.
- Andrews, S. R., and Miller, B. A. (1991). J. Appl. Phys. **70**, 993.
- Asom, M. T., Bethea, C. G., Focht, M. W., Fullowan, T. R., Gault, W. A., Glogovsky, K. G., Guth, G., Leibenguth, R. E., Levine, B. F., Lievscu, G., Luther, L. C., Stayt, Jr., J. W., Swaminathan, V., Wong, Y. M., and Zussman, A. (1991), in Proceedings of the IRIS Specialty Group on Infrared Detectors, Vol. I, p. 13.
- Bandara, K. M. S. V., Coon, D. D., O, B., Lin, Y. F., and Francombe, M. H. (1988). Appl. Phys. Lett. **53**, 1931.
- Bandara, K. M. S. V., Choe, J.-W., Francombe, M. H., Perera, A. G. U., and Lin, Y. F. (1992). Appl. Phys. Lett. **60**, 3022.
- Bandara, K. M. S. V., Levine, B. F., and Asom, M. T. (1993a). J. Appl. Phys. **74**, 346.
- Bandara, K. M. S. V., Levine, B. F., Leibenguth, R. E., and Asom, M. T. (1993b). J. Appl. Phys. **74**, 1826.
- Bandara, K. M. S. V., Levine, B. F., and Kuo, J. M. (1993c). Phys. Rev. **B 48**, 7999.
- Bandara, S., Gunapala, S., Liu, J., Hong, W., and Park, J. (1997). SPIE **2999**, 103.
- Bandara, S. V., Gunapala, S. D., Liu, J. K., Luong, E. M., Mumolo, J. M., Hong, W., Sengupta, D. K., and McKelvey, M. J. (1998a). SPIE **3379**, 396.
- Bandara, S. V., Gunapala, S. D., Liu, J. K., Luong, E. M., Mumolo, J. M., Hong, W., Sengupta, D. K., and McKelvey, M. J., (1998b), Appl. Phys. Lett., **72**, 2427.
- Beck, W. A. (1993). Appl. Phys. Lett. **63**, 3589.
- Beck, W. A., Faska, T. S., Little, J. W., Albritton, J., and Sensiper, M. (1994). Second International Symposium on 2-20 μm Wavelength Infrared Detectors and Arrays: Physics and Applications, Miami Beach, Florida.
- Bethea, C. G., Levine, B. F., Shen, V. O., Abbott, R. R., and Hseih, S. J. (1991). IEEE Trans. Electron Devices **38**, 1118
- Bethea, C. G., and Levine, B. F. (1992). In Proceedings of SPIE International Symposium on Optical Applied Science and Engineering, San Diego, CA.

- Bethea, C. G., Levine, B. F., Asom, M. T., Leibenguth, R. E., Stayt, J. W., Glogovsky, K. G., Morgan, R. A., Blackwell, J., and Parish, W. (1993). *IEEE Trans. Electron Devices* **40**, 1957.
- Bois, Ph., Costard, E., Duboz, J. Y., Nagle, J., Rosencher, E., and Vinter, B. (1995). *SPIE Proceeding*, Vol. 2552, pp. 755-766.
- Breiter, R., Cabanski, W., Koch, R., Rode, W., and Ziegler, J. (1998). *SPIE* **3379**, 423.
- Capasso, F., Mohammed, K., and Cho, A. Y. (1986). *IEEE J. Quantum Electron.* **22**, 1853.
- Chahine, M. T., (1990), "Sensor requirements for Earth and Planetary observations", *Proceedings of Innovative Long Wavelength Infrared Detector Workshop*, Pasadena, California, April 3.
- Chang, Y.-C., and James, R. B. (1989). *Phys. Rev. B* **39**, 12672.
- Chiang, J. C., Li, S. S., Tidrow, M.Z., Ho, P., Tsai, C.M., and Lee, C. P., (1996), *Appl. Phys. Lett.*, **69**, 2412.
- Chiu, L. C., Smith, J. S., Margalit, S., Yariv, A., and Cho, A. Y. (1983). *Infrared Physics*, **23**, 93.
- Choe, J. W., O, B., Bandara, K. M. S. V., and Coon, D. D. (1990). *Appl. Phys. Lett.*, **56**, 1679.
- Choi, K. K., Levine, B. F., Malik, R. J., Walker, J., and Bethea, C. G. (1987a). *Phys. Rev. B*, **35**, 4172.
- Choi, K. K., Levine, B. F., Bethea, C. G., Walker, J., and Malik, R. J. (1987b). *Phys. Rev. Lett.*, **59**, 2459.
- Choi, K. K., Levine, B. F., Jarosik, N., Walker, J., and Malik, R. J. (1987c). *Appl. Phys. Lett.*, **50**, 1814.
- Choi, K. K., (1998), *Appl. Phys. Lett.*, **65**, 1266.
- Choi, K. K., (1996), *J. Appl. Phys. Lett.*, **80**, 1257.
- Choi, K. K., Goldberg, A. C., Das, N. C., Jhabvala, M. D., Bailey, R. B., and Vural, K. (1998a). *SPIE* **3287**, 118.
- Choi, K. K., Chen, C. J., Goldberg, A. C., Chang, W. H., and Tsui, D. C. (1998b). *SPIE* **3379**, 441.
- Coon, D. D., and Karunasiri, R. P. G. (1984). *Appl. Phys. Lett.* **45**, 649.
- Duston, D., (1995), "BMDO's IS&T faces new hi-tech priorities", *BMDO Monitor*, 180.
- Elman, B., Koteles, E. S., Melman, P., Jagannath, C., Lee, J., and Dugger, D. (1989). *Appl. Phys. Lett.* **55**, 1659
- Esaki, L., and Sakaki, H. (1977). *IBM Tech. Disc. Bull.* **20**, 2456.
- Faska, T. S., Little, J. W., Beck, W. A., Ritter, K. J., Goldberg, A. C., and LeBlanc, R. (1992). *In Innovative Long Wavelength Infrared Detector Workshop*, Pasadena, CA.

- Foire, A., Rosencher, E., Bois, P., Nagle, J., and Laurent, N., (1994), Appl. Phys. Lett., **64**, 478.
- Goosen, K. W., and Lyon, S. A. (1985). Appl. Phys. Lett. **47**, 1257.
- Grave, I., and Yariv, A. (Sept. 9-14). *Intersubband Transitions in Quantum Wells*, edited by E. Rosencher, B. Vinter, and B. Levine, (1992). Cargese, France (Plenum, New York), p. 15.
- Grave, I., Shakouri, A., Kuze, N., and Yariv, A. (1993). "Control of electric field domain formation in multiquantum well structures", Appl. Phys. Lett. **63**, 1101.
- Gunapala, S. D., Levine, B. F., Logan, R. A., Tanbun-Ek, T., and Humphrey, D. A. (1990a). Appl. Phys. Lett. **57**, 1802
- Gunapala, S. D., Levine, B. F., Pfeiffer, L., and West, K. (1990b). J. Appl. Phys. **69**, 6517.
- Gunapala, S. D., Levine, B. F., Ritter, D., Hamm, R. A., and Panish, M. B. (1991a). Appl. Phys. Lett. **58**, 2024.
- Gunapala, S. D., Levine, B. F., and Chand, N. (1991b). J. Appl. Phys. **70**, 305.
- Gunapala, S. D., Levine, B. F., Ritter, D., Hamm, R. A., and Panish, M. B. (1991c). SPIE **1541**, 11.
- Gunapala, S. D., Levine, B. F., Ritter, D., Hamm, R. A., Panish, M. B. (1992a). Appl. Phys. Lett. **60**, 636.
- Gunapala, S. D., Levine, B. F., Ritter, D., Hamm, R., and Panish, M. B. (1992b). J. Appl. Phys. **71**, 2458
- Gunapala, S. D., Bandara, K. S. M. V., Levine, B. F., Sarusi, G., Sivco, D. L., and Cho, A. Y. (1994a). Appl. Phys. Lett. **64**, 2288.
- Gunapala, S. D., Bandara, K. S. M. V., Levine, B. F., Sarusi, G., Park, J. S., Lin, T. L., Pike, W. T., and Liu, J. K. (1994b). Appl. Phys. Lett. **64**, 3431.
- Gunapala, S. D., and Bandara, K. M. S. V. (1995). Physics of Thin Films, Academic Press **21**, 113.
- Gunapala, S. D., Liu, J. K., Sundaram, M., Park, J. S., Shott, C. A., Hoelter, T., Lin, T. L., Massie, S. T., Maker, P. D., Muller, R. E., and Sarusi, G. (1995a). Elec. Chem. Soc. **95-28**, 55.
- Gunapala, S. D., Park, J. S., Sarusi, G., Lin, T. L., Liu, J. K., Maker, P. D., Muller, R. E., Shott, C. A., Hoelter, T., and Levine B. F. (1997a). IEEE Trans. Electron Devices **44**, 45.
- Gunapala, S. D., Liu, J. K., Park, J. S., Sundaram, M., Shott, C. A., C. A. Hoelter, C. A., Lin, T-L., Massie, S. T., Maker, P. D., Muller, R. E., and Sarusi, G. (1997b). IEEE Trans. Electron Devices **44**, 51.

- Gunapala, S. D., Bandara, S. V., Liu, J. K., Hong, W., Sundaram, M., Maker, P. D., Muller, R. E., Shott, C. A., and Carralejo R. (1998a). *IEEE Trans. Electron Devices* **45**, 1890.
- Gunapala, S. D., Bandara, S. V., Singh, A., Liu, J. K., Luong, E. M., Mumolo, J. M., and McKelvey, M. J. (1998b). *SPIE* **3379**, 225.
- Gunapala, S. D., Bandara, S. V., Liu, J. K., Hong, W., Luong, E. M., Mumolo, J. M., McKelvey, M. J., Sengupta, D. K., Singh, A., Shott, C. A., Carralejo, R., Maker, P. D., Bock, J. J., Ressler, M. E., Werner, M. W., and Krabach, T. N. (1998c). *SPIE* **3379**, 382.
- Harwit, A., and Harris, Jr., J. S. (1987). *Appl. Phys. Lett.* **50**, 685.
- Hasnain, G., Levine, B. F., Bethea, C. G., Logan, R. A., Walker, J., and Malik, R. J. (1989). *Appl. Phys. Lett.* **54**, 2515.
- Hasnain, G., Levine, B. F., Sivco, D. L., and Cho, A. Y. (1990a). *Appl. Phys. Lett.* **56**, 770.
- Hasnain, G., Levine, B. F., Gunapala, S., and Chand, N. (1990b). *Appl. Phys. Lett.* **57**, 608.
- Hoff, J., Kim, S., Erdtmann, M., Williams, R., Piotrowski, J., Bigan, E., and Razeghi, M. (1995a). *Appl. Phys. Lett.* , **67**, 22.
- Hoff, J., Jelen, C., Slivken, S., Bigan, E., Brown, G., and Razeghi, M. (1995b). *SPIE* **2397**, 445.
- Janousek, B. K., Daugherty, M. J., Bloss, W. L., Rosenbluth, M. L., O'Loughlin, M. J., Kanter, H., De Luccia, F. J., and Perry, L. E. (1990). *J. Appl. Phys.* **67**, 7608.
- Jelen, C., Slivken, S., Brown, G., and Razeghi, M. (1997). *Mat. Res. Soc. Symp.* **450**, 195
- Jelen, C., Slivken, S., David, T., Razeghi, M., and Brown, G. (1998a). *IEEE J. Quantum Elec.* **34**, 1124.
- Jelen, C., Slivken, S., David, T., Brown, G., and Razeghi, M. (1998b). *SPIE* **3287**, 96.
- Kane, M. J., Emeny, M. T., Apsley, N., and Whitehouse, C. R. (1989). *Electron. Lett.* **25**, 230.
- Karunasiri, R. P. G., Park, J. S., Mii, Y. J., and Wang, K. L. (1990). *Appl. Phys. Lett.* **57**, 2585.
- Kastalsky, A., Duffield, T., Allen, S. J., and Harbison, J. (1988). *Appl. Phys. Lett.* **52**, 1320.
- Kiledjian, M. S., Schulman, J. N., and Wang, K. L. (1991). *Phys. Rev. B* **44**, 5616.
- Kinch, M. A., and Yariv, A. (1989). *Appl. Phys. Lett.* **55**, 2093.
- Kingston, R. H. (1978). *Detection of Optical and Infrared Radiation* (Springer, Berlin).

Kozlowski, L. J., Williams, G. M., Sullivan, G. J., Farley, C. W., Andersson, R. J., Chen, J., Cheung, D. T., Tennant, W. E., and DeWames, R. E. (1991a). *IEEE Trans. Electron. Devices* **ED-38**, 1124.

Kozlowski, L. J., DeWames, R. E., Williams, G. M., Cabelli, S. A., Vural, K., Cheung, D. T., Tennant, W. E., Bethea, C. G., Gault, W. A., Glogovsky, K. G., Levine, B. F., and Stayt, Jr., J. W. (Aug. 13-16, 1991b). In *Proceedings of the IRIS Specialty Group on Infrared Detectors*, **NIST**, Boulder, CO, Vol. **I**, p. 29.

Lacoe, R. C., O'Loughlin, M. J., Gutierrez, D. A., Bloss, W. L., Cole, R. C., Dafesh, P. A., and Isaac, M. (1992). *Proc. SPIE*.

Levine, B. F., Malik, R. J., Walker, J., Choi, K. K., Bethea, C. G., Kleinman, D. A., and Vandenberg, J. M. (1987a). *Appl. Phys. Lett.*, **50**, 273.

Levine, B. F., Choi, K. K., Bethea, C. G., Walker, J., and Malik, R. J. (1987b). *Appl. Phys. Lett.*, **50**, 1092.

Levine, B. F., Choi, K. K., Bethea, C. G., Walker, J., and Malik, R. J. (1987c). *Appl. Phys. Lett.*, **51**, 934.

Levine, B. F., Bethea, C. G., Choi, K. K., Walker, J., and Malik, R. J. (1987d). *J. Appl. Phys.* **64**, 1591.

Levine, B. F., Cho, A. Y., Walker, J., Malik, R. J., Kleinman, D. A., and Sivco, D. L. (1988a). *Appl. Phys. Lett.* **52**, 1481.

Levine, B. F., Bethea, C. G., Choi, K. K., Walker, J., and Malik, R. J. (1988b). *Appl. Phys. Lett.* **53**, 231.

Levine, B. F., Bethea, C. G., Hasnain, G., Walker, J., and Malik, R. J. (1988c). *Appl. Phys. Lett.*, **53**, 296.

Levine, B. F., Hasnain, G., Bethea, C. G., and Chand, N. (1989). *Appl. Phys. Lett.* **54**, 2704.

Levine, B. F., Bethea, C. G., Hasnain, G., Shen, V. O., Pelve, E., Abbott, R. R., and Hsieh, S. J. (1990a). *Appl. Phys. Lett.*, **56**, 851.

Levine, B. F., Bethea, C. G., Shen, V. O., and Malik, R. J. (1990c). *Appl. Phys. Lett.* **57**, 383.

Levine, B. F., Gunapala, S. D., and Kopf, R. F. (1991a). *Appl. Phys. Lett.* **58**, 1551.

Levine, B. F., Gunapala, S. D., Kuo, J. M., Pei, S. S., and Hui, S. (1991b). *Appl. Phys. Lett.* **59**, 1864.

Levine, B. F., Gunapala, S. D., and Hong, M. (1991c). *Appl. Phys. Lett.* **59**, 1969.

Levine, B. F., Bethea, C. G., Glogovsky, K. G., Stayt, J. W., and Leibenguth, R. E. (1991d). *Semicond. Sci. Technol.* **6**, C114.

Levine, B. F. (Sept. 9-14, 1991e). *Proceedings of the NATO Advanced Research Workshop on Intersubband Transitions in Quantum Wells*, Cargese, France, edited by E. Rosencher, B. Vinter, and B. F. Levine. (Plenum, London).

- Levine, B. F., Zussman, A., Kuo, J. M., and de Jong, J. (1992a). J. Appl. Phys. **71**, 5130.
- Levine, B. F., Zussman, A., Gunapala, S. D., Asom, M. T., Kuo, J. M., and Hobson, W. S. (1992b). J. Appl. Phys. **72**, 4429.
- Levine, B. F. (1993). J. Appl. Phys. **74**, R1.
- Li, S. S., Chuang, M. Y., and Yu, L. S., (1993), Semicond. Sci. Technol., **8**, 406.
- Liu, H. C., Aers, G. C., Buchanan, M., Wasilewski, Z. R., and Landheer, D. (1991a). Appl. Phys. Lett. **70**, 935
- Liu, H. C., Buchanan, M., Aers, G. C., and Wasilewski, Z. R. (1991b). Semicond. Sci. Technol. **6**, C124.
- Liu, H. C. (1992a). Appl. Phys. Lett. **60**, 1507.
- Liu, H. C. (1992b), Appl. Phys. Lett., **61**, 2703.
- Liu, H. C., Wasilewski, Z. R., Buchanan, M., (1993), Appl. Phys. Lett. **63**, 761.
- Manasreh, M. O., Szmulowicz, F., Fischer, D. W., Evans, K. R., and Stutz, C. E. (1991). Phys. Rev. B **43**, 9996.
- Martinet, E., Luc, F., Rosencher, E., Bois, Ph., Costard, E., Delaitre, S., and Bockenhoff, E. (Sept. 9-14 1991). In *Intersubband transitions in Quantum wells*, edited by E. Rosencher, B. Vinter, and B. Levine, (1992). France (plenum, New York.), p. 299.
- Mei, T., Karunasiri, G., and Chua, S. J. (1997). Appl. Phys. Lett. **71**, 2017.
- Mii, Y. J., Karunasiri, R. P. G., Wang, K. L., Chen, M., and Yuh, P. F. (1989). Appl. Phys. Lett. **55**, 2417.
- Mooney, J. M., Shepherd, F. D., Ewing, W. S., Murgia, J. E., and Silverman, J. (1989). Opt. Eng. **28**, 1151.
- O. B., Choe, J.-W., Francombe, M. H., Bandara, K. M. S. V., Coon, D. D., Lin, Y. F., and Takei, W. J. (1990). Appl. Phys. Lett. **57**, 503.
- Pelve, E., Beltram, F., Bethea, C. G., Levine, B. F., Shen, V. O., Hsieh, S. J., Abbott, R. R. (1989). J. Appl. Phys. **66**, 5656.
- Pinczuk, A., Heiman, D., Sooryakumar, R., Gossard, A. C., and Wiegmann, W. (1986). Surf. Sci. **170**, 573.
- Pool, F. S., Wilson, D. W., Maker, P. D., Muller, R. E., Gill, J. J., Sengupta, D. K., Liu, J. K., Bandara, S. V., and Gunapala, S. D. (1998). SPIE **3379**, 402.
- Realmuto, V. J., Sutton, A. J., and Elias, T. (1997). J. Geo. Phys. Res. **102**, 15057.
- Ritter, D., Hamm, R. A., Panish, M. B., Vandenberg, J. M., Gershoni, D., Gunapala, S. D., and Levine, B. F. (1991). Appl. Phys. Lett. **59**, 552
- Rosencher, E., Luc, F., Bois, Ph., and Delaitre, S. (1992). Appl. Phys. Lett. **61**, 468.
- Sarusi, G., Levine, B. F., Pearton, S. J., Bandara, K. M. S. V., and Leibenguth, R. E. (1994a). Phys. Lett. **64**, 960.

- Sarusi, G., Levine, B. F., Pearton, S. J., Bandara, K. M. S. V., and Leibenguth, R. E. (1994b). *J. Appl. Phys.* **76**, 4989.
- Sarusi, G., Gunapala, S. D., Park, J. S., and Levine, B. F. (1994c). *J. Appl. Phys.* **76**, 6001.
- Sengupta, D. K., Jackson, S. L., Ahmari, D., Kuo, H. C., Malin, J. I., Thomas, S., Feng, M., Stillman, G. E., Chang, Y. C., Li, L., and Liu, H. C. (1996). *Appl. Phys. Lett.* **69**, 3209.
- Shepherd, F. D. (1988). *In Infrared Detector and Arrays*, SPIE Vol. 930 (SPIE Orlando, FL), p.2.
- Smith, J. S., Chiu, L. C., Margalit, S., Yariv, A., and Cho, A. Y. (1983). *J. Vac. Sci. Technol.* **B 1**, 376.
- Steele, A. G., Liu, H. C., Buchanan, M., and Wasilewski, Z. R. (1991). *Appl. Phys. Lett.* **59**, 3625.
- Swaminathan, V., Stayt, Jr., J. W., Zilko, J. L., Trapp, K. D. C., Smith, L. E., Nakahara, S., Luther, L. C., Livescu, G., Levine, B. F., Leibenguth, R. E., Glogovsky, K. G., Gault, W. A., Focht, M. W., Buiocchi, C., and Asom, M. T. (Aug. 1992). In *Proceedings of the IRIS Specialty Group on Infrared Detectors*, Moffet Field, CA.
- Tidrow, M. Z., and Bacher, K. (1996). *Appl. Phys. Lett.*, **69**, 3396.
- Tidrow, M. Z., Chiang, J. C., Li, S. S., and Bacher, K. (1997). *Appl. Phys. Lett.* **70**, 859.
- Vodjdani, N., Vinter, B., Berger, V., Bockenhoff, E., and Costard, E. (1991). *Appl. Phys. Lett.* **59**, 555.
- Watanabe, M. O., and Ohba, Y. (1987). *Appl. Phys. Lett.* **50**, 906.
- Weisbuch, C. (1987). *Semiconductor and Semimetals* **24**, 1.
- West, L. C., and Eglash, S. J. (1985). *Appl. Phys. Lett.* **46**, 1156.
- Wheeler, R. G., and Goldberg, H. S. (1975). *IEEE Trans. Electron Devices* **ED-22**, 1001.
- Wieck, A. D., Batke, E., Heitman, D., and Kotthaus, J. P. (1984). *Phys. Rev. B* **30**, 4653.
- Wu, C. S., Wen, C. P., Sato, R. N., Hu, M., Tu, C. W., Zhang, J., Flesner, L. D., Pham, L., and Nayer, P. S. (1992). *IEEE Trans. Electron Devices* **39**, 234.
- Xing, B., and Liu, H. C. (1996). *J. Appl. Phys.*, vol. 80, 1214.
- Yao, J. Y., Andersson, T. G., and Dunlop, G. L. (1991). *Appl. Phys.* **69**, 2224.
- Yu, L. S., and Li, S. S. (1991a). *Appl. Phys. Lett.* **59**, 1332.
- Yu, L. S., Li, S. S., and Ho, P. (1991b). *Appl. Phys. Lett.* **59**, 2712.
- Yu, L. S., Wang, Y. H., Li, S. S., and Ho, P. (1992). *Appl. Phys. Lett.* **60**, 992.
- Zhou, X., Bhattacharya, P. K., Hugo, G., Hong, S. C., and Gulari, E. (1989). *Appl. Phys. Lett.* **54**, 855.

Zussman, A., Levine, B. F., Kuo, J. M., and de Jong, J. (1991). J. Appl. Phys. **70**, 5101.